Systems & Control

Dynamic Error Budgeting

a design approach

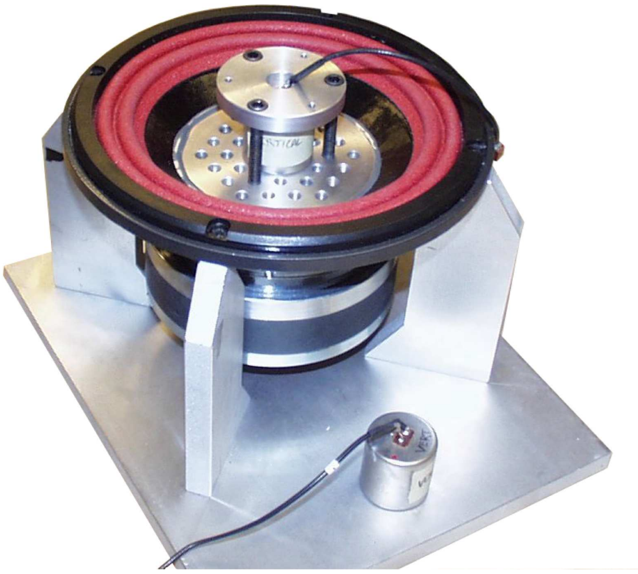

Wouter Monkhorst

Supervisors ir. L. Jabben
prof. dr. ir. D.L. Trumper
dr. ir. R. Tousain
Professor prof. dr. ir. O.H. Bosgra

Delft, March 31, 2004

TU Delft
Faculty of Design, Engineering and Production

Preface

This thesis is the result of a very exciting and adventurous year of doing research at different locations. It has always been a dream for me to do research at the Massachusetts Institute of Technology (MIT) in Boston, U.S.A. and thanks to professor Jan van Eijk (Advanced Mechatronics, Delft University of Technology (DUT)), this dream has become a reality. The resulting research project was done in co-operation with Philips Center for Industrial Technology (Philips CFT) and MIT.

After I finished a feasibility study of a design approach applicable to high end mechatronic systems, I have done a five months research project at MIT, Boston. Back in the Netherlands, I finished the research at Philips CFT, Eindhoven. In this research I was able to bring together the theory I have learned at the Systems and Control group DUT, with the practical knowledge of mechatronic system design at MIT, a very challenging job!

First of all, I would like to acknowledge my supervisor ir. Leon Jabben for all his time and support supervising my graduation project and help with the theoretical background and interpretation of results. I'm very thankful to Professor Trumper for the guidance he gave me during my research and for making it possible for me to do this at MIT. I would also like to thank dr. ir. Rob Tousain for his guidance and support during my research at Philips CFT.
Last, but not least, I would like to thank other colleague researchers who helped me with various difficulties and for making this year a pleasant time. A lot of thanks to Katie Lilienkamp, Rick Montesani and David Otten for their help with the design of the experimental setup at MIT, thanks to Michiel Vervoordeldonk, Toon Blom, Dick Goossens and Ger Jansen for helping me out with the noise modelling at Philips CFT.

Contents

Summary

In today's industry the performance demands on high end mechatronic systems are increased continuously, systems are to be faster, more accurate and less expensive. System designers face the challenge to design mechatronic solutions that are to fulfill these demands. The high design costs make it that one cannot afford to make a design failure, resulting in an important design demand: the system must be 'first time right'. High end mechatronic systems have become more and more complex. The system is often designed per sub-system by different designers, sometimes even at different locations, making the design challenge even bigger. In this environment the designer needs a structural approach which enables him to face this challenge. This thesis is about the development of such a design approach, which leads to the problem statement of this thesis:

problem statement: develop a tool that enables a system designer to predict the final performance of a system subject to disturbances and gives insight in what system property limits the performance. Show the feasibility of this approach.

Using this approach the designer must be able to predict the final performance a priori, accounting for all the disturbances that act on the system, enabling him to design a system such that it will be first time right.

In this thesis such an approach is developed using theory of spectral analysis and is referred to as the *Dynamic Error Budgeting* (DEB) design approach. The theory $\mathcal{H}_2$ -control is then added, reaching the designer a tool to improve his design strategy even further. The approach is then put to the test in two case studies, both concerning the *vibration isolation* problem. A vibration isolation system is to isolate a *payload*, e.g., very sensitive equipment, from ground vibrations. The vibration isolation problem can be solved passively (e.g., airmount) or actively. In this thesis the focus is on the active systems, which use a control loop to achieve the isolating performance. The performance of an active vibration isolation system is determined by the disturbances that act on the system, e.g., the ground vibrations themselves, but also the noise generated by its electrical components.

In the first case study the final performance of an active vibration isolation system is analyzed by modelling all the disturbances and calculating the performance level at the output. The system is then redesigned to improve the final performance. Using the DEB approach it is shown that pre-amplifying the sensor signal gives a huge performance improvement.

Next, an $\mathcal{H}_2$ - controller is synthesized improving the performance even more. Finally, the performance when using two different preamplifiers is compared using $\mathcal{H}_2$ controllers in the loop, enabling the designer to make an objective performance comparison of the two different preamplifiers. A number of experiments is done to validate the theory.

The second case study is about an active vibration isolation module that can be used parallel to an existing passive isolator. The drawback of introducing an additional active isolator, is that its active components also introduce additional disturbances, like electronic noise. The improvement in isolating performance must therefore at least counter balance introduction of the additional disturbances due to its active components, which is analyzed using the DEB approach. The approach shows that the sensor used in this active isolator is *the* main performance limiter of the system and that the total performance is indeed improved.
The two case studies show that the DEB design approach is a powerful tool for the designer in today's challenging industrial environment. The approach predicts the final performance of the system during the design process, and gives valuable insight in the limiting components and/or system properties. It also helps the designer to keep track of the total system in a modular design approach. Using $\mathcal{H}_2$ -control as an add-on to the DEB approach, the designer can objectively compare different system concepts using $\mathcal{H}_2$ control, helping him to justify important design decisions. Further research can be done to the choice of the performance variable, the use of higher order disturbance models, to the applicability of the information given by the $\mathcal{H}_2$ controller in practice and to the development a strategy that can be followed to improve the system performance.

Nomenclature

Symbols

$u(t)$	controller output signal $[V]$
$w(t)$	disturbance signal [SI]
$z(t)$	performance signal [SI]
$E_g(t)$	geophone output voltage $[V]$
$E_{in}(t)$	power amplifier input voltage $[V]$
$E_{out}(t)$	preamplifier output voltage $[V]$
$E_{sp}(t)$	voice coil input voltage $[V]$
$X_b(t)$	base plate position $[m]$
$X_l(t)$	cone plate or pay*load* position $[m]$
$C(s)$	controller
$C_{\mathcal{H}_2}(s)$	$\mathcal{H}_2$ controller
$C_z(f)$	cumulative power spectrum of signal $z(t)$ [SI²]
f	frequency $[Hz]$
$G(s)$	open loop weighted transfer function
$\bar{G}(s)$	open loop transfer function
G_g	geophone generator constant $[V/(m/s)]$
$H(s)$	closed loop transfer function
$H_g(s)$	sensor dynamics
$L(s)$	loop transfer function
N_f	speaker force constant $[N/A]$
$P(s)$	general open loop plant
$P_{geo}(s)$	geophone velocity sensitivity $E_g/\dot{X}_l$
$P_{speaker}(s)$	speaker transfer function $\dot{X}_l/E_{in}$
$P_{sp\_geo}(s)$	least square fit on E_g/E_{in}
$P_{sp\_vib}(s)$	open loop speaker model $\dot{X}_l/\dot{X}_b$
R_c	geophone coil impedance $[\Omega]$
R_s	speaker voice coil impedance $[\Omega]$
$S(s)$	loop sensitivity function $(1 + L(s))^{-1}$
$S_z(f)/S_z(\omega)$	power spectral density function of signal $z(t)$ [SI²/Hz]
$V_w(f)$	input weighting filter to model disturbances [SI]

$W_z(f)$	output weighting filter for relative output scaling $[-]$

Greek Symbols

σ_x	standard deviation of the signal $x(t)$ [SI]
σ_x^2	variance of the signal $x(t)$ [SI^2]
μ_x	mean of the signal $x(t)$ [SI]

Abbreviations and Acronyms

ade	ADC electrical (noise)
ade	ADC quantization (noise)
dae	DAC electrical (noise)
dae	DAC quantization (noise)
emf	electro motive force
pa	Preamplifier (noise)
sus	Suspension (noise)
coil	Geophone coil (noise)
lsb	Least significant bit
opamp	Operational Amplifier

AC	Alternating Current
ADC	Analogue to Digital Converter
AIMS	Advanced Isolation ModuleS
ASD	Amplitude Spectral Density [SI/$\sqrt{Hz}$]
AVI	Advanced Vibration Isolation
CPS	Cumulative Power Spectrum [SI^2]
CAS	Cumulative Amplitude Spectrum [SI]
DAC	Digital to Analogue Converter
DC	Direct Current
DEB	Dynamic Error Budgeting
DOF	Degree Of Freedom
DSA	Dynamic Signal Analyzer
FFT	Fast Fourier Transform
MIMO	Multi Input Multi Output
NHNM	New High Noise Model
NLNM	New Low Noise Model
P(I)D	Proportional, (Integral,) Derivative
PSD	Power Spectral Density [SI^2/Hz]
SISO	Single Input, Single Output
SNR	Signal to Noise Ratio [dB]

Chapter 1

Introduction

1.1 Context of this thesis

In modern society the use of high performance mechatronic systems is rapidly increasing. Systems like DVD players and computers are now part of every day life, and the desire for even better performing systems is clearly present. Manufacturers are forced to push the performance of their existing system concepts to the limit and develop new system concepts that can achieve even higher performance levels. The design of these high end mechatronic systems forms the context of this thesis.
High performance mechatronic systems have become more and more complex. The system is often designed per sub-system by different designers, sometimes even at different locations. The design is often time consuming and very expensive. The modular character and the high costs of the design process result in an important demand on the design of the system; the designed system must be *first time right*. This means that, when the system is finally build, its performance level must satisfy the specifications. No significant changes are allowed in the post-design phase! Because of this, the designer wants to be able to predict the performance of the system a-priori and gain insight in the performance limiting factors of the system. A design approach that enables designer to do so is the subject of this research.

1.2 Dynamic error budgeting

Mechatronic systems often comprise a certain number of sub-systems and a controller C, together forming a control loop which enforces a certain desired closed loop system behavior. The performance of such a system is generally defined by the error made, which is caused by the disturbances d that act on the system. This idea is illustrated in Figure 1.1 (left hand side). The error e can be seen as a measure of performance of the system.

In the design of precision machines an approach called *error budgeting* is often used to attribute an allowable amount of error to the machine's different components, see e.g., Slocum [21, p.61]. Every disturbance acting on the closed loop system is then allowed to contribute a certain part of the total error budget. The design is satisfying if the total

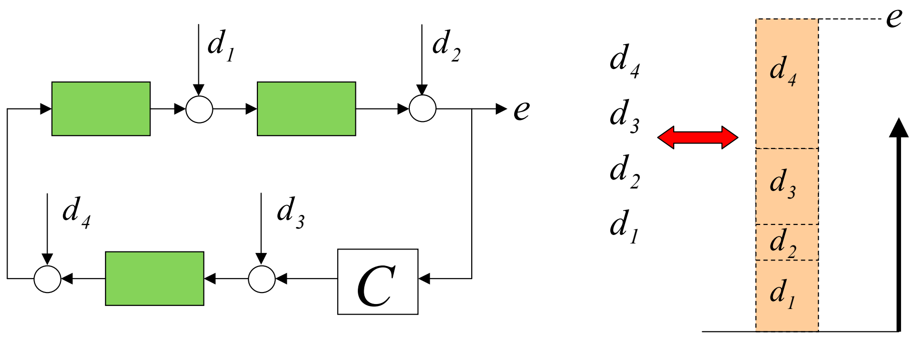

Figure 1.1 left*: The error e made by a mechatronic system determines its performance and results from the disturbances d that act on the closed loop system.* right*: The error is a measure of performance of the closed loop system and can be seen as the result of the separate contributions caused by the different input disturbances.*

budget does not exceed the performance specification, if not, the system has to be redesigned. The basic idea behind this approach is that the error can be seen as the result of the separate contributions caused by the different input disturbances, as is illustrated on the right hand side of Figure 1.1. For the designer to be able to predict the performance (indicated by the right-arrow) and to attribute a part of the error to the system disturbances (indicated by the left-arrow), he needs to know how each disturbance propagates to the error. In the error budgeting approach this relation is approximated using rules of thumb, which are (very often) based on simulations with sinusoidal signals. In practise most disturbances are of a stochastic nature, to which the rules of thumb do not apply.
However, the propagation of stochastic disturbances to the output can be described exactly (in theory) when one uses a frequency dependent relation to describe the propagation. This relation is described in the theory of *spectral analysis* and uses frequency dependent models of the disturbances and sub-systems. Because (almost all) the disturbances in high performance mechatronic system are stochastic of nature, they can be modelled with their *power spectral densities* (PSDs). This results in a new design approach which will be referred to as *Dynamic Error Budgeting* (DEB), where 'dynamic' refers to the use of the frequency dependent models. This approach enables the designer to accurately budget the error, to predict the final output error and to point out critical sub-systems and/or disturbances.

1.3 Vibration isolation

To put the DEB design approach to the test, it will be applied to two design cases, both concerning the *vibration isolation* problem. Vibration isolation is much used in modern high precision machines, where the obtained precision would not be possible without the use of vibration isolation, e.g., diamond turning machines, optical measurement equipment and gravity wave detection antennas. Another good example where extreme high precision is needed is in the production of Integrated Circuits (IC). So-called wafer stages move wafers of silicon with a repeated accuracy of ± 50 nm in order to project the image of the circuit onto a photoresist layer on the wafer (from [20]). Production of ICs would not be possible without the use of vibration isolation. As such, vibration isolation receives a lot of research attention.

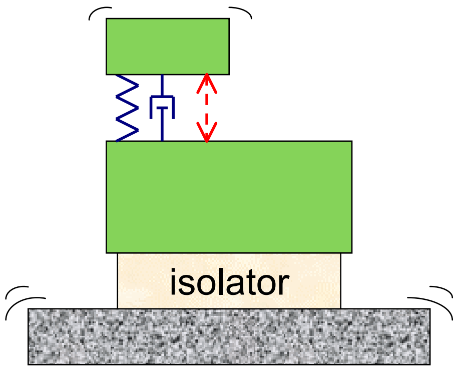

Figure 1.2 *Vibrations of the ground, will cause systems mounted on that ground to vibrate as well. Internal flexibilities of the system will result in internal deformations (indicated with the arrow), which, in general, have a negative effect on the accuracy (performance) of the system. In order to improve the performance of the system a* vibration isolator *can be used to isolate the system (now called the payload) from vibrations.*

The goal of vibration isolation is to isolate a payload system from ground vibrations, see Figure 1.2. Isolation from ground vibrations requires a soft (low stiffness) mounting of the payload to that ground. However, this results in a high sensitivity to disturbance forces originating from the payload itself; suppression of payload disturbances forces requires a high stiffness mounting to the ground, see Harris [9] and Subrahmanyan [22].

When using a passive isolation device this results in a fundamental trade-off between the rejection of ground vibrations and payload disturbances. Adding active control to the mounting, gives means to improve the performance by dampening of the suspension resonances in the system. However, when a relative sensor between ground and payload is used in the control system, the fundamental trade-off between payload and ground disturbance rejection still exists, limiting the performance. This fundamental limitation in performance can be circumvented by the use of an absolute measurement of the payload movement. This can be done by using an accelerometer measuring absolute accelerations, or a geophone measuring absolute velocity.

With an active control system using an absolute sensor, the fundamental trade-off no longer exists. The performance is now constrained because of the limited performance of the components used in the control loop, e.g., acceleration and velocity can only be measured over a limited frequency range and the active components in the control loop introduce additional disturbances like e.g., sensor noise and amplifier noise. These disturbances are stochastic of nature and can be modelled by their PSDs. This gives the designer the opportunity to use the DEB design approach for the design of the system!

1.4 Challenge definition

In the previous paragraphs it was explained that there is a need for a more accurate and structured design approach that enables the designer to account for stochastic disturbances *during* the design of the system. The active vibration isolation problem is introduced as a possible field of application for this approach. This leads to the challenge definition of this thesis:

Develop a tool which enables the designer to account for stochastic disturbances during the design of a mechatronic system.

From this challenge definition the following research goals can be formulated:

Develop tools that enable the designer to:

- Predict the final performance level of a system which is subject to stochastic disturbances.
- Gain insight in performance limiting factors of the system. This insight should enable the designer to point out critical system components/properties and to improve the performance of the system.
- Objectively compare the performance of different system designs. When a system designer starts off with several different system concepts, he needs to find out which concept is the most promising.

Show the feasibility of these tools by applying them in the design of two (one DOF) active vibration isolation systems. Steps to be taken in this research are:

- Investigate if there is a gap between the theoretically predicted results and the experimentally measured results. If there is a gap, try to explain the difference.
- Show that is possible to point out critical components and to improve the system performance, using the obtained insight in performance limiting factors.
- Show that it is possible to objectively compare the performance of two different systems.
- Apply the approach to a system which is in the design phase and show the feasibility of the approach in practice.

1.5 Outline of thesis

In Chapter 2 the DEB approach is covered in more detail. First, motivations are given that support the development of this new approach and the design process itself is described. After that the limitations of the DEB approach are given. What assumptions should be met and what things should be considered to make sure the theory is applicable? Next, the theoretical background is given which forms the basis of the approach. The theoretical definition of performance and power spectral densities is given, and it is described how the performance can be calculated and analyzed using the theory of propagation. In the last part of this chapter the theory of $\mathcal{H}_2$ control is given, which can be can be seen as an add-on to the DEB design approach. The theory of $\mathcal{H}_2$ control describes how to control the system in order to maximize its performance given the system and its disturbance models.

To put the approach to the test, the approach is applied in two case studies, both concerning a design of an active vibration isolator. The first case study covers both chapters 3 and 4. The second case study is described in Chapter 5.

The focus of the first study is to validate the approach in practice. Is the theory applicable in practice and does the approach give the designer more design insight? In Chapter 3 an active vibration isolator is described, modelled and its disturbances identified and modelled as well. The performance of the system is calculated in theory and compared with experimental results. In Chapter 4 the $\mathcal{H}_2$ control strategy is applied to the same system and the theoretically predicted performance it achieves is validated using experimental results.
The second case study is about an active vibration isolator with a more advanced working principle. This principle is explained and the system and disturbances are modelled. This system is still in the design phase and the main goal of this case study is to apply the design approach in practice as it is developed for.

Finally, in Chapter 6 conclusions and suggestions for further work are given regarding the DEB design approach and the use of $\mathcal{H}_2$ control in this approach.

Chapter 2

Dynamic Error Budgeting

In this chapter the DEB design approach is covered in more detail. First, the motivations behind the DEB approach are explained in more detail. Next, the DEB process itself is described and the limitations of the approach are discussed. In the remainder of the chapter the theoretical background of the approach is given.

2.1 Motivations of the DEB design approach

The main motivation for the development of the DEB approach is the need for the designer to account for disturbances while designing a high performance mechatronic system, as is already mentioned in the introduction of this thesis. The following advantages of this approach can be mentioned.

Cutting costs in the design phase. If the error is not simulated during the design phase, the final performance level can only be found when a costly prototype is build and the performance can be measured physically. If the performance level is not met, the designer has to find out what component or disturbance causes the output to exceed the error budget and then redesign the system, a rather time consuming and costly job. If the error could be simulated beforehand however, changes can be made when the system is still in the design phase, cutting down the costs of the system.

Speeding up the design process. Since the simulations can be done on a computer, it can give a quick indication if a concept is feasible or not. Several concepts can be analyzed in a short period of time and the most promising concept can be chosen, speeding up the design process.

Enhancing design insight. If the performance specification is not met, the designer wants to know which component or what system property is limiting the performance most. The designer also wants to know how much each disturbance contributes to the output error. For example, a very expensive low-noise sensor can possibly be replaced with a cheaper sensor if the simulations show that the cheaper sensor performs well within the specifications. The analysis of the simulated error shows all the information needed for the designers to make these kind of trade-offs, helping the designer to make design decisions.

2.2 DEB design process

The DEB design process can be summarized as follows: choose a system concept and simulate the output error. If the total error is meets the performance specification, the design is satisfying. If the error exceeds the specified budget, the designer has to change the system such that the specification is met. Step by step, the process is as follows:

- Design a concept system.
- Model the concept system, such that the closed loop transfer functions can be determined.
- Identify all significant disturbances. Model them with their *Power Spectral Density*(PSD).
- Define the performance (error) outputs of the system and simulate the output error. Using the theory of *propagation*, the contribution of each disturbance to the output error can be analyzed and the critical disturbance(s) can be pointed out.
- Make changes to the system that are expected to improve the performance level, and simulate the output error again. Iterate until the error budget is met.

The theoretical background of this approach (e.g., the use of PSDs and theory of propagation) is covered in § 2.4.

2.3 Assumptions and research boundaries

The DEB approach can only be applied when the system and its disturbances satisfy the following assumptions:

- It is assumed that the (sub-)system can be accurately described with a linear time invariant model. This assumption is not expected to cause much problems, for the following reasons: First of all, in today's mechatronic system design a lot of effort is put in to make systems have a linear behavior. Second, high precision mechatronic machines often comprise a feedback loop, which has a 'linearizing' effect on the closed loop behavior. Many high precision machines have a small working range, which makes it more likely for the system to behave linearly.

  Anyhow, if a system does shows non-linear behavior, the deviation from the linear behavior could be modelled as a disturbance and added to the analysis. This approach might not be so straightforward as it sounds and is considered outside the scope of this research.

- The disturbances acting on the system must be stationary; their statistical properties are not allowed to change over time. In practise this can dealt with by applying some sort of averaging of the measured PSDs over longer periods of time. For example, when ground vibrations are modelled, it is customary to measure the worst case PSD over a few hours, sometimes even a whole day.

- The third assumption also applies to the disturbances and says that the disturbances are assumed to be uncorrelated with each other. This condition is more difficult to satisfy under certain circumstances, especially for a MIMO (Multi Input, Multi Output) systems. For example, it is unlikely that ground vibrations in one direction are uncorrelated with another direction. The designer must therefore make sure that the separate disturbances all originate from separate independent sources. The theory in this chapter can be easily extended to be also valid for correlated signals, however this is outside the scope of this research.

- The disturbance signals will modelled by their PSD. This implies another assumption on the disturbances: they must have a defined PSD, so *only stochastic disturbances are allowed*. Deterministic components, like sinusoidal and DC signals, in a disturbance signal give infinite peaks in their PSD, making it meaningless in the DEB approach. In practise however, there will be periodic disturbance sources like e.g., pickup noise in electrical circuitry due to electromagnetic waves in the air caused by the periodically (60 Hz) alternating current of the electricity grid and disturbances originating from rotating machines, like ground vibrations and acoustic noise. The DEB analysis can then still be used, but should then only be applied to the stochastic part of the disturbances. For the deterministic part other (straightforward) techniques can be used to determine their influence to the error. In this research it will be assumed that all disturbances are stochastic of nature.

- It should be noted that the calculation method makes no assumption on the distribution of the distribution functions of the disturbances. In practise, many (stochastic) disturbances will have a normal (or Gaussian) like distribution. Although not all disturbances have a normal distribution, the performance output channel is most likely characterized accurately with a normal distribution; the performance channel is the sum of contributions by many disturbances, the *Central Limit Theorem*, see e.g., Priestley [16, p95] and Papoulis [14, p266] then states that the output will approach a normal distribution for an increasing number of disturbances.

2.4 Theoretical background

The theory covered in this section is discussed in more detail in Monkhorst [12]. Here, a short summary of the results is given.

2.4.1 Variance as a performance measure

The term 'performance of systems' is a very general term and needs interpretation. In this thesis the performance of a system is measured by the *variance* of the error signal. The variance gives an interpretation of how much power is spread around the *mean* of the signal, cancelling out the power of the DC component. A (deterministic) DC component has an infinite power density (at 0 Hz), making it impossible to represent it with a PSD. Therefore it can not be accounted for in the DEB approach. In the remainder of this thesis, all signals are assumed to have a zero mean. The variance σ_x^2 of a signal $x(t)$ is defined as the signal power or *mean square* $\bar{x^2}$ minus the squared *mean* μ_x^2:

$$\text{variance} \quad \sigma_x^2 = \bar{x^2} - \mu_x^2 \tag{2.1}$$

$$\text{power} \quad \bar{x^2} = \lim_{T\to\infty} \frac{1}{2T} \int_{-T}^{T} x(t)^2 dt \tag{2.2}$$

$$\text{mean} \quad \mu_x = \lim_{T\to\infty} \frac{1}{2T} \int_{-T}^{T} x(t) dt \tag{2.3}$$

In this thesis the term *power* refers to this mathematical definition (2.2) of signal power [SI^2] and not to physical power, which is expressed as energy per unit of time $[J/s]$.

2.4.2 Parseval's Theorem: linking the frequency to the time domain

In this thesis all disturbances and noise sources will be modelled using a *Power Spectral Density* function (PSD). Before the definition of a PSD is given in § 2.4.3, the relation between energy in the time domain and energy in the frequency domain will be described.

For non-periodic finite duration signals the energy in the time domain is described by:

$$\text{Energy:} \quad = \int_{-\infty}^{\infty} x(t)^2 dt \tag{2.4}$$

Parseval's Theorem now states that energy in the time domain equals the energy in the frequency domain as follows:

$$\text{Energy:} \quad = \int_{-\infty}^{\infty} x(t)^2 dt = \int_{-\infty}^{\infty} |X(f)|^2 df \tag{2.5}$$

where $X(f)$ is the Fourier Transform of the time signal $x(t)$ and is given by:

$$X(f) = \int_{-\infty}^{\infty} x(t) e^{-2\pi j f t} dt \tag{2.6}$$

2.4.3 Power spectral density function

Every disturbance signal that enters the system has a certain variance (or power) level, defined by (2.1). However, since the propagation transfer functions of a system are likely

to be frequency dependent, one needs the power distribution over frequency to describe the propagation (see § 2.4.4). The power distribution over frequency of a time signal $x(t)$ is described by the PSD denoted with $S_x(f)$. A PSD is a power density function with units $[SI^2/Hz]$, meaning that the area underneath the PSD curve equals the power (units $[SI^2]$) of the signal (SI is the unit of the signal, e.g., m/s). When the signal has a zero mean, the area of the PSD equals the variance of the signal. A DC component, or other deterministic signal content, would cause the PSD to have infinite peaks, so a PSD can only reliably represent the power density of a stochastic signal.
One can also use a *Power Spectrum* (PS) to represent the signal power distribution. A PS has units $[SI^2]$ and can only be defined on a discrete number of frequency points, since it would otherwise define an infinite power contents of the signal. A PS can only reliably represent deterministic signals like a sinusoid or a DC component, because the magnitude of a PS representing a stochastic signal would be dependent of the resolution of the frequency grid. In this research only stochastic signals are considered, so the PS is not used in this thesis.

Using the definition of signal power ($\bar{x^2}$) and Parseval's theorem we can link power in the time domain with power in the frequency domain:

$$\begin{aligned} \text{power} = \lim_{T\to\infty} \frac{1}{2T} \int_{-T}^{T} x_T(t)^2 dt &= \lim_{T\to\infty} \frac{1}{2T} \int_{-\infty}^{\infty} |X_T(f)|^2 df \\ &= \int_{-\infty}^{\infty} \left(\lim_{T\to\infty} \frac{|X_T(f)|^2}{2T} \right) df \end{aligned} \tag{2.7}$$

where $X_T(f)$ denotes the Fourier transform of $x_T(t)$, which equals $x(t)$ on the interval $T \leq t \leq T$, and is zero outside this interval. We will refer to the term within the integral as the two-sided power spectral density $S_x(f)$, since its integral over frequency equals the signal power.

$$S_{x\_two}(f) = \lim_{T\to\infty} \frac{|X_T(f)|^2}{2T} \ , \quad -\infty \leq f \leq \infty \tag{2.8}$$

In practice the one-sided PSD is used, which is only defined on the positive frequency axis, $0 \leq f \leq \infty$, but also contains all the power. The one-sided PSD is therefore simply defined as the double of the two-sided PSD:

$$S_{x\_one}(f) = \lim_{T\to\infty} \frac{|X_T(f)|^2}{T} \ , \quad 0 \leq f \leq \infty \tag{2.9}$$

In the remainder of this report, $S_x(f)$ refers to a one-sided PSD.

Discrete formulation

For discrete time signals the one-sided PSD estimate is defined as:

$$\hat{S}(f_k) = \frac{|X_L(f_k)|^2}{LT_s} \tag{2.10}$$

where L equals the number of time samples and T_s the sample time, $X_L(f_k)$ is the N-point discrete Fourier Transform of the discrete time signal $x_L[n]$ containing L samples:

$$X_L(f_k) = \sum_{n=0}^{N-1} x_L[n] e^{-j\,2\pi kn/N} \tag{2.11}$$

It is wise to choose the number of frequency points N larger than the time vector length L such that N is the next power of two larger than L. To evaluate $X_L[f_k]$, we simply pad $x_L[n]$ with zeros to length N.
The mean power of the signal can be estimated with the following sum:

$$\text{power} \approx \sum_{k=0}^{N-1} \frac{|X_L(f_k)|^2}{L^2} \tag{2.12}$$

The term after the summation symbol is called the two-sided discrete *Power Spectrum* and can be easily computed using the MATLAB® command `fft`, which computes the two-sided Fast Fourier Transform. Appendix A.1 shows the code to compute the two sided PSD from a sampled time signal.

2.4.4 Propagation of disturbances

Key to the DEB design approach is to realize that the final performance of the system is determined by all the disturbances that act on the closed loop system. These disturbances apply at different locations in the closed loop system, as illustrated in Figure 2.1. The disturbances $w(t)$ are assumed to be stochastic, and can therefore be easily modelled with their PSD (In this thesis, the PSD of a signal is denoted by a dashed box, this is not a dynamic filter!). Examples of disturbances are amplifier noise, ground vibrations, sensor noise, etc.. This section gives the mathematical description of how each disturbance propagates through the closed loop system and contributes to the output error.

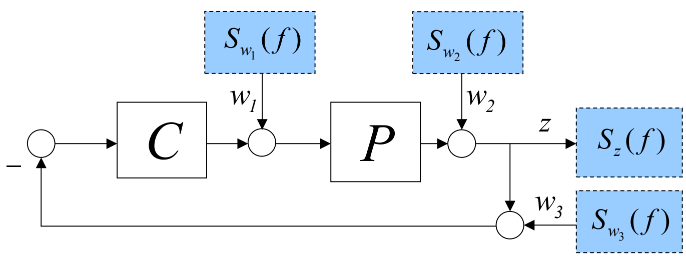

Figure 2.1 *Schematic of a closed loop system with various disturbances. The disturbances $w(t)$ can be modelled with their power spectral density function $S_w(f)$, denoted with a dashed box.*

The theory presented here is described in Papoulis [14], Balmer [1], Priestley [16] and Harris [9]. As said, the disturbance signals z_i can be modelled using PSDs, which will be denoted by $S_{w_i}(f)$. To calculate the performance of the system, we consider the closed loop system as a black box system, with transfer function $H(j\omega) = H(j\,2\pi f)$:

$$\begin{bmatrix} z_1 \\ \vdots \\ z_k \end{bmatrix} = \begin{bmatrix} H_{11} & \cdots & H_{1n} \\ \vdots & \ddots & \vdots \\ H_{k1} & \cdots & H_{kn} \end{bmatrix} \begin{bmatrix} w_1 \\ \vdots \\ w_n \end{bmatrix} = \tag{2.13}$$

where the input w stacks n disturbances, and output z stacks k performance outputs. For multi-variable systems, see Ljung [11], the PSD of the output is then given by:

$$S_z(f) = H(j\,2\pi f)\ S_w(f)\ H^{\mathrm{T}}(-j\,2\pi f) \tag{2.14}$$

where S_z is a matrix with the PSDs of the performance signals $z_1, \ldots, z_k$ on the diagonal. When that the disturbance inputs $w(t)$ are *uncorrelated*, the input PSD S_w will be diagonal, which simplifies the calculations. Since we are only interested in the PSDs of the performance signals, we only look at the diagonal terms of S_z, which follow from (2.14). The PSD of the jth performance output $S_{z_j}(f)$ due to all the noise PSDs $S_{w_i}(f)$, is calculated by propagating all the corresponding input PSDs to that output. Since $H_{ji}(j\,2\pi f)\ S_{w_i}(f)\ H_{ji}^{\mathrm{T}}(-j\,2\pi f)$ equals $|H_{ji}(j\,2\pi f)|^2\ S_{w_i}(f)$, the PSD of the jth output can be written as:

$$S_{z_j}(f) = \sum_{i=1}^{k} |H_{ji}(j\,2\pi f)|^2\ S_{w_i}(f) \tag{2.15}$$

In words; the PSD of a performance channel is the linear sum of each disturbance PSD multiplied with the squared magnitude of the corresponding SISO transfer function. Equation 2.15 offers the designer an important opportunity to analyze the error and to point out critical components or system properties, since it describes the PSD of the performance signal in terms of input disturbance PSDs and closed loop system transfer functions. This calculation method was implemented in the MATLAB® environment.

Now it follows from (2.1), (2.7) and 2.9 that

$$\bar{z^2} = \int_0^{\infty} S_z(f)df \tag{2.16}$$

In words: since a PSD describes the power density over frequency [SI^2/Hz], the integral of the output PSD $S_z(f)$ over frequency equals the power $\bar{z^2}$ of the performance signal $z(t)$. Because all signals are assumed to have zero mean, this integral equals the variance (2.1) of the performance signal:

$$\sigma_z^2 = \int_0^{\infty} S_z(f)df \tag{2.17}$$

where $S_z(\omega)$ is the one-sided PSD of the signal. Another very useful function in performance analysis is the *Cumulative Power Spectrum* (CPS), which is defined as:

$$C_z(f_o) = \int_0^{f_o} S_z(f)df \tag{2.18}$$

where $S_z(f)$ is the corresponding one-sided output PSD. The CPS is defined from $f_o = 0$ to $f_o = \infty$ and is a monotone increasing function with its magnitude increasing from zero to $C_w(\infty) = \sigma_z^2$. Because the final value of the CPS equals the variance of the signal, it clearly indicates how much power is located at which frequency.

The ASD and CAS

In this thesis we will not analyze the PSD and CPS of the performance signal, but at their square rooted versions (element-wise): the *Amplitude Spectral Density* (ASD) [SI/$\sqrt{Hz}$] and the *Cumulative Amplitude Spectrum* (CAS) [SI], which actually contain the same information. In formula:

$$\begin{aligned} \text{ASD}(f) &= \sqrt{|PSD(f)|} \quad \forall \quad f & (2.19) \\ \text{CAS}(f) &= \sqrt{|CPS(f)|} \quad \forall \quad f & (2.20) \end{aligned}$$

A motivation to use the CAS is that its final value, at ($f = \infty$), equals the standard deviation of the signal, so e.g., σ_z. Since performance specifications are often given in terms of a σ-value, using the CAS makes it easier to compare the results with the specifications. Besides this, the standard deviation is easier interpretable in the time domain than the variance. For example, the 3-σ value gives a good approximation of the maximum amplitude of a stochastic signal. A motivation to use the ASD instead of the PSD is that its units correspond better to the CAS, which is more a matter of taste.

2.5 $\mathcal{H}_2$ control, maximizing performance

2.5.1 Use of $\mathcal{H}_2$ control in DEB

Precision machines often use a feedback control loop to achieve a certain system behavior. When the used controller C is not fixed, it acts as a degree of freedom in the closed loop transfer function defining the disturbance propagation as described in § 2.4.4. This idea is illustrated in Figure 2.2. One can use this degree of freedom in the system in order to minimize the output error, giving the designer an upper bound on the achievable system performance. The controller that achieves this goal, is called the $\mathcal{H}_2$ controller $C_{\mathcal{H}_2}$ and is unique given the system and its disturbances.
The resulting $\mathcal{H}_2$ controller is also very useful to the control engineer, since it shows how to control the system optimally, given the disturbances. In the following sections the theory of $\mathcal{H}_2$ control is explained.

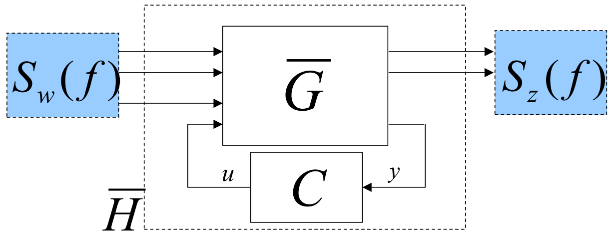

Figure 2.2 *The controller C acts as a degree of freedom in the closed loop transfer function $\bar{H}$, and therefore in the determination of the output error.*

2.5.2 The $\mathcal{H}_2$ norm and variance of the output

The $\mathcal{H}_2$ norm is a norm defined on a system and can be stated as follows:

$$\|H\|_2^2 = \int_{-\infty}^{\infty} |H(j\,2\pi f)|^2\,df \tag{2.21}$$

In order to relate the $\mathcal{H}_2$ system norm to the performance definition used in this thesis, we will look at the stochastic interpretation of the $\mathcal{H}_2$ norm; the squared $\mathcal{H}_2$ norm can be interpreted as the output variance of a system with zero mean white noise input. So, the value obtained in the (2.21) equals the output variance of the system $H(j\,2\pi f)$ having zero mean white noise input.
When the total system with its disturbance models is defined as a system with white noise inputs, the $\mathcal{H}_2$ controller will minimize the output variance of that system. In § 2.5.4 it is explained how the disturbance models S_w can be included in the system using weighting filters with zero mean white noise input. First, the $\mathcal{H}_2$ control problem is formulated.

2.5.3 The $\mathcal{H}_2$ control problem

The $\mathcal{H}_2$ control problem can be stated as follows: 'Find a controller $C_{\mathcal{H}_2}$which minimizes the $\mathcal{H}_2$ norm of the closed loop system H', or expressed in a formula:

$$C_{\mathcal{H}_2} \in \arg\min_{C} \|H(j\,2\pi f)\|_2 \tag{2.22}$$

$\mathcal{H}_2$ controller synthesis can be done using various methods. One of them is solving two Ricatti equations as described in Doyle (et.al.) [6], using the MATLAB® command `hinfsyn`. In order to synthesize an $\mathcal{H}_2$ controller, one needs to model the open loop system as a generalized plant and the generalized plant needs to meet several standard assumptions as described in Appendix A.2. But, before the generalized plant can be set up, the disturbance models need to be included in the open loop model, which is done in the next section.

2.5.4 Using weighting filters to model disturbances

In order to synthesize an $\mathcal{H}_2$ controller that will minimize the output error, the total system including disturbances needs to be modelled as a system with zero mean white noise inputs.

This is done by using weighting filter $V_w(j\,2\pi f)$, of which the output signal has the previously discussed PSD $S_w(f)$ when the input is zero mean white noise. This is illustrated in Figure 2.3.

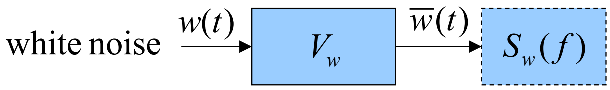

Figure 2.3 *The use of a weightingfilter $V_w(f)$ [SI] to give the weighted signal $\bar{w}(t)$ a certain PSD $S_w(f)$.*

The white noise input $w(t)$ is dimensionless [-], and when the weightingfilter has units [SI], the resulting weighted signal $\bar{w}(t)$ has units [SI]. The PSD $S_w(f)$ of the weighted signal is now given by (also see Equation 2.14):

$$|S_w(f)| = V_w(j\,2\pi f)\ S_{in}(f)\ V_w^{\mathrm{T}}(-j\,2\pi f) \tag{2.23}$$

Since the PSD of a white noise signal $S_{in}(f)$ equals unity (or the identity matrix in a multivariate case) and has units $[-/Hz]$, and V_w has units [SI], $S_w(f)$ now indeed has the units of a PSD [SI$^2/Hz$].
Since the disturbances are assumed to be uncorrelated $S_w(f)$ is diagonal, so the resulting input weighting filter $V_w(f)$ will also be diagonal. Given $S_w(f)$, $V_w(f)$ can be obtained using a technique called *spectral factorization*. However, the step of spectral factorization can be avoided by modelling the disturbances directly in terms of a weighting filter, which is the strategy followed in this research.
$\mathcal{H}_2$ controller synthesis also allows to use output weighting filters. We will use this possibility to scale different defined outputs relative to each other as will be explained in more detail in § 2.5.5. The output weighting filter is denoted by $W_z(f)$.

In Figure 2.4 it can be seen that the generalized plant G now consists of the open loop plant $\bar{G}$ in series with the weighting filter $V_w(f)$ and output scaling filter $W_z(f)$.

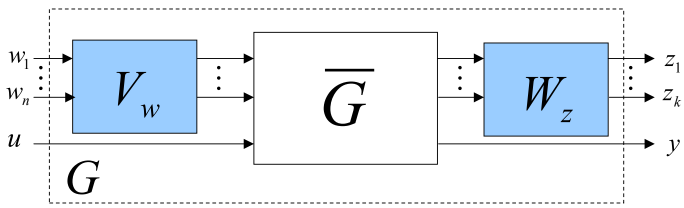

Figure 2.4 *The open loop system $\bar{G}$ in series with the diagonal input weighting filter V_w and diagonal output scaling filter W_z defining the generalized plant G.*

Now that a generalized plant is defined, is has to meet the assumptions in Appendix A.2 in order for the $\mathcal{H}_2$ controller synthesis algorithm to work. If the assumptions are not met, the weighting and/or scaling filters have to be adjusted appropriately.

2.5.5 Output scaling and the Pareto curve

The closed loop system can have more than one output. In this research the performance (error) signal e and the controller output u are defined as the outputs of the closed loop system, see Figure 2.5. In this way the system designer can analyze how much control effort (defined here as the variance of the controller signal u) is used to achieve the performance level at the performance output. When the system designer designs several different system concepts, he wants to compare them by their maximum achievable performance, to decide what concept is the most promising. When he wants to make an objective performance comparison, he can choose the amount of control effort to be equal for each system concept. The resulting problem is actually a multi-objective control problem; while constraining the variance of the controller output signal u the variance of the performance channel should be minimized. This problem can be solved by scaling e.g., the controller output u with a factor α during $\mathcal{H}_2$ controller synthesis, such that the control power used by the different $\mathcal{H}_2$ controllers is equal (see Boyd [3]). The output scaling factor α is then contained in the output scaling filter $W_z(f)$. The designer now only has to find the right scaling factor α by iteration.

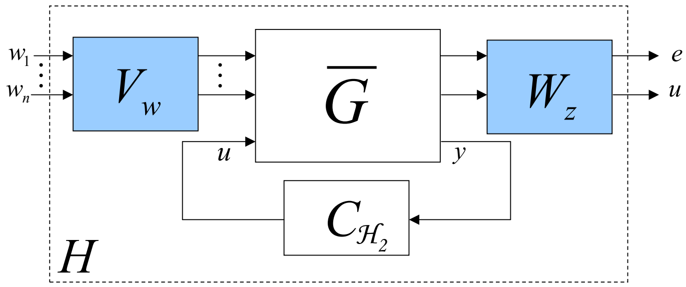

Figure 2.5 *The closed loop system, with weighting filters included. The system has n disturbance inputs and two outputs; the error e and the control signal u. The $\mathcal{H}_2$ controller minimizes the $\mathcal{H}_2$ -norm of this system.*

When varying the scaling factor α, one can plot the amount of control effort at one axis and the achieved performance on the other axis. The resulting points lie on the so-called Pareto curve (see Boyd [3]) . Every point on the curve corresponds to a certain scaling α and describes the control effort needed to achieve the corresponding performance level. Examples of Pareto curves can be found in Sections 4.2 and 4.4.

2.6 Conclusions on the theory

The theory covered in this chapter gives the designer a tool with which he can model stochastic disturbance sources, predict the performance and analyze the resulting error. He is also able to point out critical transfer functions and/or disturbance sources. All the tools to make the DEB design approach work in theory are now available.
$\mathcal{H}_2$ controller synthesis offers the designer the opportunity to optimize over the degree of freedom given by the controller. This enables the designer to calculate the maximum per-

formance level that is achievable with a certain system concept (given its configuration and disturbance models). With the use of controller output scaling during $\mathcal{H}_2$ controller synthesis, the designer is capable of objectively comparing different system concepts by synthesizing $\mathcal{H}_2$ controllers that use the same amount of control effort in each case.

Chapter 3

Case study, active vibration isolation

3.1 Introduction

Chapters 3 and 4 describe the research done during a five months stay at the Massachusetts Institute of Technology in Boston, U.S.A. in the Precision Motion Control laboratory of Professor D.L. Trumper. The main challenge taken in the research at MIT is to validate the dynamic error budgeting design approach (as theoretically described in Chapter 2) in practice. The main question that is tried to answer is: Does the Dynamic Error Budgeting (DEB) design approach also work in practice?

In order to apply the approach in practice, a complete vibration isolation setup is to be designed and build. The system that was build (see 3.1) is an improved version of the setup described in Trumper [24]. The practical implications of building the setup is not further discussed here. The goal of this chapter is to apply the DEB approach to the design of this system and identify the performance limiting factors and use this information to improve the performance of the system. Finally, the theoretical results must be compared with experimental results to validate the theoretically predicted performance of DEB approach and find out what the cause is of the possible gap between theory and practice.

The experimental setup is described and modelled in Section 3.2. In Section 3.3 all disturbances that act on the system are modelled as stochastic signals. With all the necessary system and disturbance models obtained, the performance of the experimental setup can be simulated and analyzed using the DEB approach, which is done in Section 3.4. The insight that is obtained with the DEB analysis is used to redesign the system; in Section 3.5 a preamplifier is added to the configuration and the performance improvement is analyzed. The theoretical results are compared with experimental results in Section 3.6. The chapter ends with conclusions on applying the DEB design approach in this case study.

3.2 An active vibration isolation platform

3.2.1 Description of the experimental setup

The experimental setup used in this case study can be seen in Figure 3.1, and consists of an 8-inch speaker as a one-axis vertical actuator and a geophone as an absolute velocity sensor. In the center of the speaker a cone plate is glued on which the geophone is rigidly mounted. The cone plate represents the payload location, and is to be isolated from vibrations.

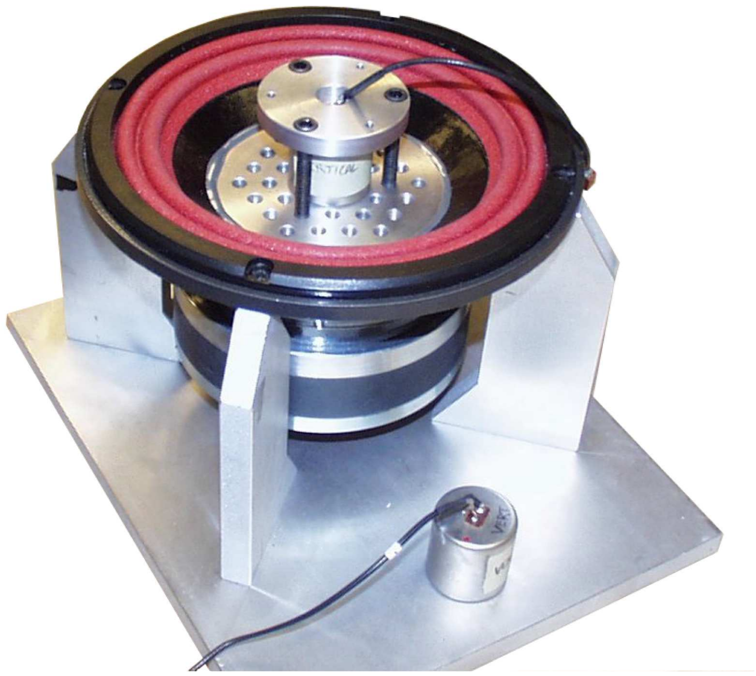

Figure 3.1 *The experimental speaker-geophone setup. An 8 inch speaker is rigidly connected to a base plate with aluminum struts. A velocity sensor (geophone) is mounted in the speaker cone. (The sensor on the base plate is not part of the actual setup, but was used to measure the input vibration level).*

A schematic configuration of the speaker and geophone can be seen in Figure 3.2. Big permanent magnets provide a permanent magnetic field. When a current is sent through the voice coil a Lorentz force F_s is created which can move the cone up or down. Ground vibrations enter the system via the base plate (X_b) and propagate through the speaker via the suspension, and cause the payload (X_l) to vibrate.

In Figure 3.3 a block scheme of the complete active vibration isolation system is given. The system was controlled using a dSpace1104 board. The voice coil is voltage driven by a Crown DC300R power amplifier. $P_{sp\_geo}(s)$ denotes the transfer function from the power amplifier input E_{in} to geophone output voltage E_g. $P_{sp\_vib}(s)$ denotes the open loop speaker model from base velocity $\dot{X}_b$ to payload velocity $\dot{X}_l$, and describes the open loop propagation of

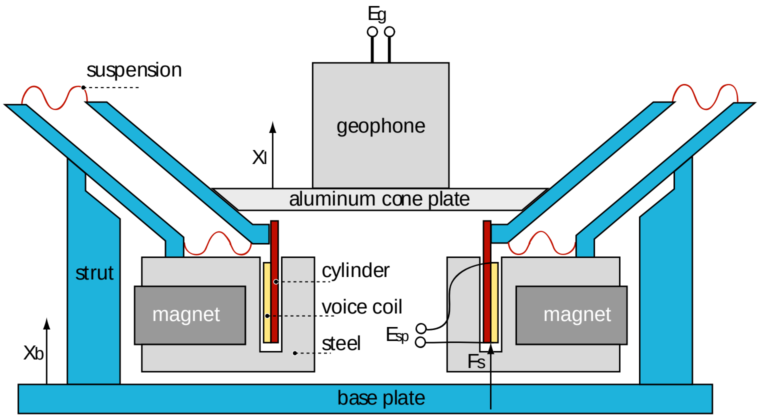

Figure 3.2 *Schematic of speaker-geophone setup. Big permanent magnets provide a permanent magnetic field. When a current is sent through the voice coil a force F_s is created which can move the cone up or down. In the center of the speaker cone a cone-plate is glued in. A velocity sensor (geophone) is mounted rigidly on the cone-plate. The cone plate is to be isolated from vibrations.*

ground vibrations into the cone plate. The dynamics of the sensor are encompassed by $P_{geo}(s)$.

3.2.2 Performance definition

To analyze the performance of the vibration isolation setup, one needs a performance variable as a model output. In this research the variance of the payload velocity $\dot{X}_l$ signal is chosen as the performance variable. To extract the performance variable $\dot{X}_l$ from the model, the transfer function $P_{speaker}(s)$ is needed, as can be seen in Figure 3.3. To obtain $P_{speaker}(s)$, $P_{sp\_geo}(s)$ can be multiplied with the inverse of the geophone dynamics $P_{geo}(s)$, such that $P_{speaker}(s) = P_{sp\_geo}(s)\ P_{geo}^{-1}(s) = \dot{X}_l/E_{in}$. $P_{sp\_geo}(s)$, $P_{sp\_vib}(s)$ and $P_{geo}(s)$ are all modelled in the next section.

3.2.3 System modelling

Vibration isolation platform

A vibration isolation platform very similar to this setup is also modelled in Trumper [24], where a 4^{th} order state space model is developed to describe the platform dynamics. This state space model was initially used to model the setup, but it turned out that the state space model differed from empirical results significantly in a crucial frequency region as will be explained at the end of this paragraph. (also see Figure 3.4). Since the model of the setup is part of the loop transfer function $L(s)$, and its accuracy will therefore influence the stability of the loop, it is chosen to base the model for the setup on the empirical data. The derivation of the state space model from Trumper [24] for this setup is done for modelling insight anyway and can be found in Appendix B.1.

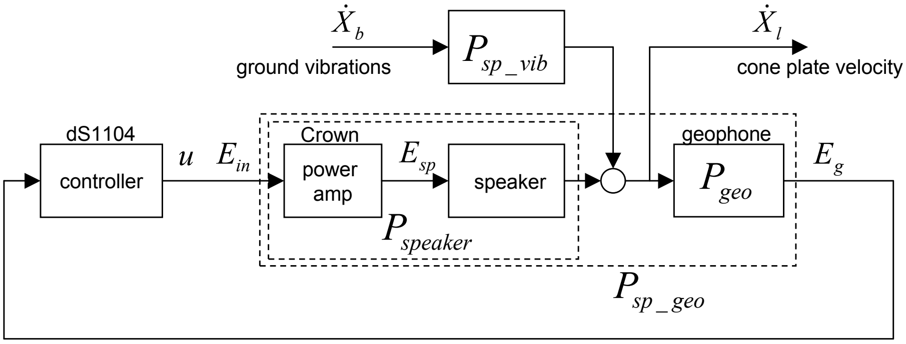

Figure 3.3 *A block scheme of the experimental setup. Ground vibrations enter the loop via the transfer function $P_{sp\_vib}(s)$, which defines the propagation of vibrations from the base plate to the cone plate. The cone plate velocity is defined as the performance variable. The system is controlled using a dSpace1104 controller board. $P_{sp\_geo}(s)$, $P_{speaker}(s)$ and $P_{geo}(s)$ define the transfer function of the speaker-geophone setup in series with the power amplifier.*

To model the transfer function $P_{sp\_geo}(s)$ (see Figure 3.3), a swept sine experiment was done using an HP35665 dynamic signal analyzer and the Crown power amplifier. The gain of the power amplifier (E_{sp}/E_{in}) was set to unity for modelling simplicity. The transfer function between the power amplifier input E_{in} and geophone output E_g was measured, on which a least square fit was made. The measured data and the resulting fitted transfer function $P_{sp\_geo}(s)$ can be seen in Figure 3.4 on the left hand side.

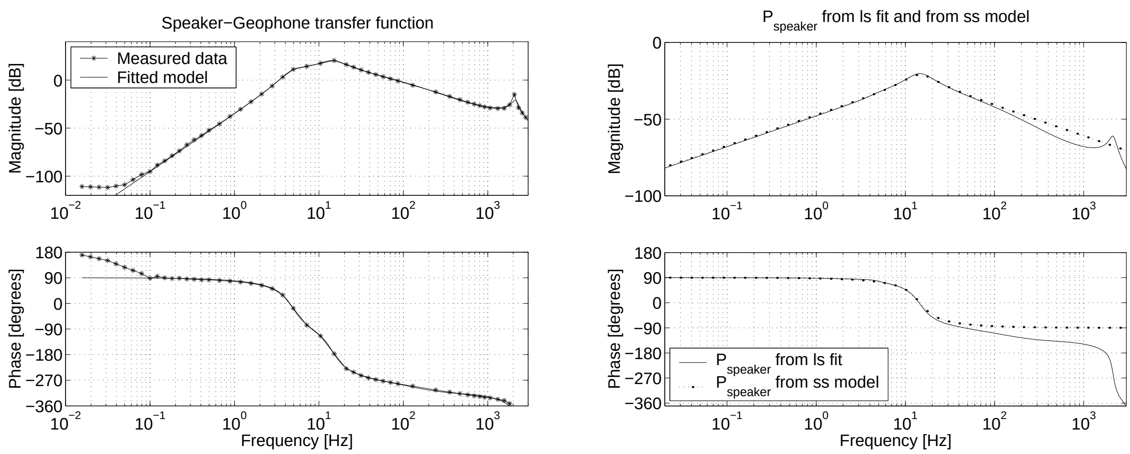

Figure 3.4 left*: The fitted transfer function $P_{sp\_geo}(s)$ together with the measured frequency response of the vibration isolation setup E_g/E_{in}.* right*: The fitted model $P_{speaker}(s)$ and the transfer function $E_{sp} = E_{in}$ to $\dot{X}_l$ extracted from state space model.*

The low frequency region, where the magnitude of the measured transfer function seems to level off, needs some special attention. Since the graph represents the transfer function from power amplifier input voltage E_{in} towards geophone output voltage E_g, the graph suggests a DC gain, which implies a certain DC geophone output voltage when a DC voltage is applied to the power amplifier. A constant geophone output voltage represents a constant velocity of the geophone coil relative to its casing, which is not possible in reality. It is not exactly known what causes the transfer function to level off, but the flat part in the low frequency region is not believed to represent the true system dynamics. The true dynamics are believed to follow the +3 slope down towards the lower frequencies. In order to match the fit with believed reality, all the poles and zeros with an absolute value smaller than 1 are placed in the origin. The resulting pole/zero pairs in the origin cancel out when obtaining a minimal realization, using the MATLAB® command `minreal`. The fitted model now has a +3 slope, starting the origin, and is given by:

$$\begin{aligned} P_{sp\_geo}(s) &= 5.20 \cdot 10^{-3} \frac{(s - 1.20 \cdot 10^4)(s + 3456)(s - 3.33 \cdot 10^{-3})}{(s + 1058)(s^2 + 19.93s + 936.9)} \cdot \\ & \quad \frac{(s^2 + 3.33 \cdot 10^{-3}s + 1.11 \cdot 10^{-5})(s^2 - 8757s + 4.94 \cdot 10^8)}{(s^2 + 57.42s + 8423)(s^2 + 2012s + 1.82 \cdot 10^8)} \end{aligned} \tag{3.1}$$

In the 5 Hz region the geophone dynamics can be seen (see § 3.2.3) and the speaker resonance frequency around 15 Hz. The peak around 2 kHz is thought to be due to a structural resonance of the speaker system (there is some flexibility between the voice coil cylinder and the aluminum cone plate, see Figure 3.2).

On the right hand side of the Figure 3.4, the model $P_{speaker}(s)$ can be seen together with the transfer function $\dot{X}_l/E_{sp}$ extracted from state space model derived in Appendix B.1. The mismatch between the two models is clearly visible. The difference in phase shift at frequencies above 100 Hz is crucial for loop stability, since the loop transfer function $L(s)$ cross-over frequency will be located in this region (see § 3.2.5). Therefore it is chosen to use the fitted model instead of the state space model.

Ground vibration propagation model $P_{sp\_vib}(s)$

Because the vibration propagation transfer function $P_{sp\_vib}(s)$ is not part of the loop transfer function $L(s)$ and thus will not influence the stability of the loop, a less accurate model can be used to model $P_{sp\_vib}(s)$. Next to that, $P_{sp\_vib}(s)$ describes the propagation of the ground vibration model towards the loop, and this ground vibration model itself is a rather rough approximation of reality as well (see § 3.3.1), so there is no issue of using a high order propagation model. Using the speaker parameters found in Appendix B.1 a second order model can be derived in terms of the speaker parameters:

$$P_{sp\_vib}(s) = \frac{N_f^2/R_s s + k_l}{m_l s^2 + N_f^2/R_s s + k_l} \tag{3.2}$$

This model assumes that the geophone dynamics have no significant contribution to the speaker dynamics. This conclusion can be drawn from the two models shown in Figure 3.4

on the right hand side. The geophone dynamics (resonance frequency at 4.8 Hz) are not visible in the extracted transfer function $\dot{X}_l/E_{in}$ from the state space model. $P_{sp\_vib}(s)$ is shown in Figure 3.8 on the right hand side.

Geophone

A geophone is a mechanism containing a proof mass which is suspended by leaf springs. The proof mass consists of a cylinder with a copper wire coil that moves in a magnetic field produced by permanent magnets fixed within the case of the geophone, see Figure 3.5. A movement of the coil generates a voltage E_g across coil output terminals, which is proportional to the velocity of the proof mass relative to the geophone's casing.

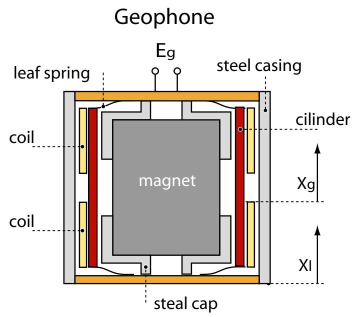

Figure 3.5 left: *Photograph of a geophone cut open. The copper coil is clearly visible.* right: *Schematic of a geophone, which generates a voltage E_g proportional to the relative velocity between the outer casing ($\dot{X}_l$) and the coil ($\dot{X}_b$).*

The geophone used in the setup is the GS11D 4.5Hz with a 4000Ω coil. A one degree of freedom model, describing the velocity sensitivity of the geophone is developed in Barzilai [2] and can be written as:

$$P_{geo}(s) = \frac{E_g}{\dot{X}_l}(s) = \frac{G_g s^2}{s^2 + 2\zeta\omega_o s + \omega_o^2} \tag{3.3}$$

and for the acceleration sensitivity we have:

$$\frac{E_g}{\ddot{X}_l}(s) = \frac{G_g s}{s^2 + 2\zeta\omega_o s + \omega_o^2} \tag{3.4}$$

where E_g is the geophone output voltage, and $\dot{X}_l$ and $\ddot{X}_l$ are the velocity and acceleration of the payload respectively. $G_g = 100\ V/(m/s)$ is the generator constant, $\omega_o = 2\pi f_o = 2\pi(4.5 \pm 0.75)$ is the natural frequency in rad/sec and $\zeta = 0.35$ the damping ratio of the geophone. The natural frequency of the geophone used in this setup turned out to be 4.8 Hz. The velocity and acceleration sensitivity can both be seen in Figure 3.6.

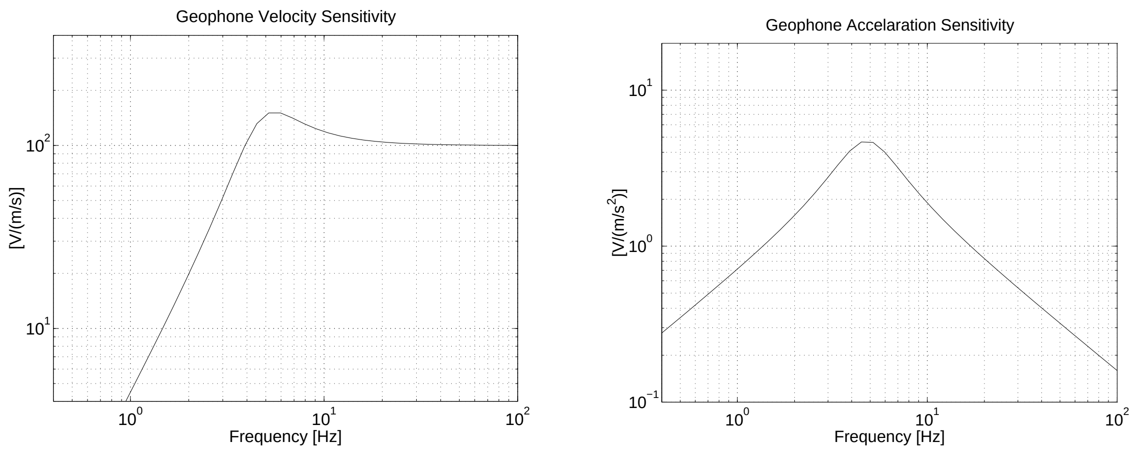

Figure 3.6 left*: The velocity sensitivity $P_{geo}(s)$ of the GS11D 4.5Hz geophone.* right*: The acceleration sensitivity of the GS11D 4.5Hz geophone.*

3.2.4 Mutual inductance of the speaker and geophone

Since the speaker and the geophone both contain coils, a phenomena called *mutual inductance* can occur. Mutual inductance is based on the idea that alternating magnetic field lines originating from one coil, generates voltages in another coil. This effect can cause the speaker and the geophone to be magnetically AC coupled. In this case, the magnetic field lines produced by the voice coil then dynamically couple in the geophone dynamics. During the swept sine experiments discussed in § 3.2.3 a magnetically shielded geophone was used. The swept sine experiment was repeated with an unshielded geophone. The shielded geophone is covered with an extra layer of shielding material as can be seen on the left hand side of Figure 3.7.

In the low frequency region the magnetic coupling has a clear effect as can be seen on the right hand side of Figure 3.7. The unshielded version shows a zero at 0.3 Hz and a much higher gain at the lower frequencies. Also, the phase shifts 180° at the frequency of the new zero. The alternating voltages in the speaker voice coil apparently couple in the geophone coil at frequencies below 1 Hz, causing the geophone output voltage not to represent the relative velocity between the casing and proof mass. Since this transfer function is part of the loop gain, this phenomena can have a dramatic effect on the stability of the control loop and must be avoided.

3.2.5 Closing the loop

The controller design for a vibration isolation platform like the one used in this setup, is covered extensively in Trumper [24]. This will not be repeated here, but a short summary of the results is given instead.

The controller used to control this setup is denoted as $C(s)$ and can be written as:

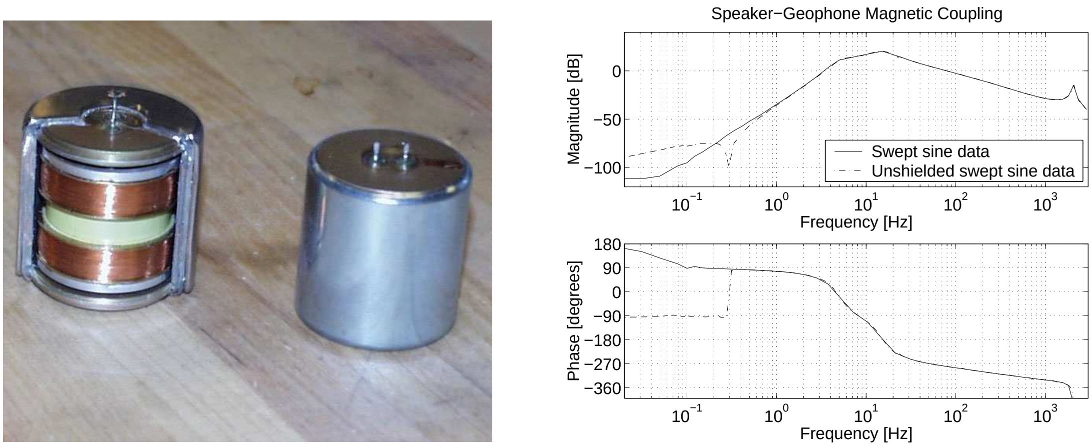

Figure 3.7 left: *Photograph of a shielded geophone cut open (left) next to an unshielded geophone (right). The shielded geophone is covered with an extra layer of magnetic shielding material.* right: *Magnetic coupling of the speaker voice coil and the geophone coil. The magnetically unshielded geophone dynamically couples with the speaker voice coil, causing a zero and a* $180°$ *phase shift at 0.3 Hz.*

$$C(s) = K_p \left(\frac{\tau_0 s}{\tau_0 s + 1}\right) \left(\frac{\tau_1 s + 1}{\alpha_1 \tau_1 + 1}\right)^2 G_{pa} \left(\frac{\tau_p s + 1}{\alpha_p \tau_p + 1}\right)^2 \left(\frac{\tau_2 s + 1}{\alpha_2 \tau_2 + 1}\right)^3 \left(\frac{1}{\tau_3 s + 1}\right) \tag{3.5}$$

with the parameters: $K_p = 64\ dB$, $\tau_0 = 100$, $t_1 = 0.5$, $a_1 = 15$, $G_{pa} = 1000$, $\alpha_p = 10$, $\tau_p = 1/(2\pi 4.5)$, $\tau_2 = 0.01$, $\alpha_2 = 3$ and $\tau_3 = 1.355 \cdot 10^{-4}$.

An important transfer function for control design is the loop transfer function $L(s)$. The loop transfer is defined as the transfer function when going around the loop. In this case $L(s)$ can be written as:

$$L(s) = C(s)\ P_{speaker}(s)\ P_{geo}(s) = C(s)\ P_{sp\_geo}(s) \tag{3.6}$$

The loop transfer functions then defines the loop sensitivity function $S(s) = (1 + L(s))^{-1}$, which defines the vibration isolation performance of the closed loop system as explained below. $L(s)$ and $S(s)$ are both shown in Figure 3.8 on the left hand side.

The open loop speaker model $P_{sp\_vib}(s)$ and closed loop speaker model $P_{sp\_vib}(s)\ S(s)$ define the propagation of ground vibrations towards the payload in the open loop respectively, closed loop case. Both transfer functions are shown in Figure 3.8 on the right hand side. Since loop sensitivity function $S(s)$ makes the difference between the open loop and closed loop vibration propagation ($P_{sp\_vib}(s)$ vs. $P_{sp\_vib}(s)\ S(s)$), it defines the increase in vibration isolation performance of the closed loop setup. Because $S(s) = (1 + L(s))^{-1}$, $S(s)$ will cause an isolating effect when $1 + L(s)$ has a gain greater than unity, as can be seen from in Figure 3.8 on the left.

It is common to refer to $P_{sp\_vib}(s)$ and $P_{sp\_vib}(s)\ S(s)$ as the open resp. closed loop *transmissibility* of the system. Comparing the open and closed loop transmissibility in Figure 3.8 (right) we can conclude that the closed loop system now isolates better than the open loop system in the 100 mHz - 100 Hz region.

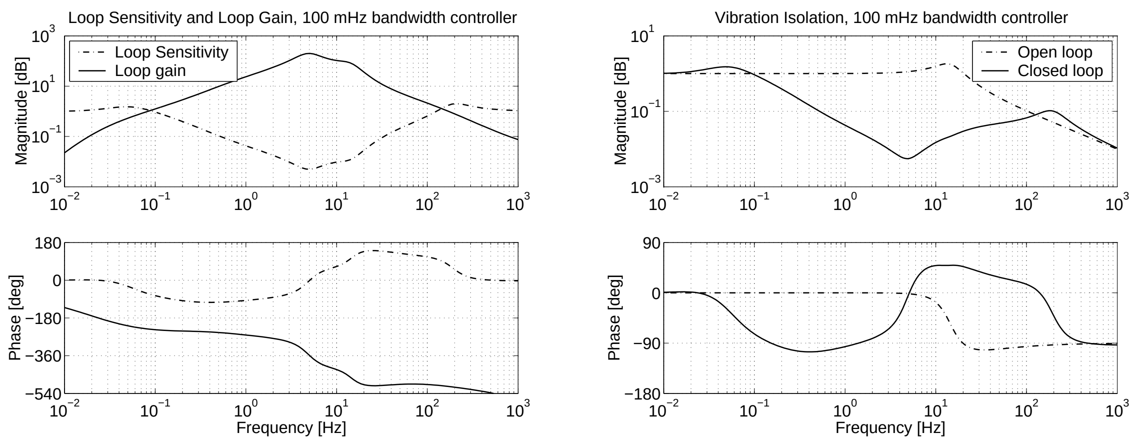

Figure 3.8 left*: Loop transfer function $L(s)$ and loop sensitivity function $S(s)$.* right*: Open loop speaker model $P_{sp\_vib}(s)$ and closed loop speaker model $P_{sp\_vib}(s)\ S(s)$, which are referred to as the open, respectively closed loop* transmissibility *of the system.*

3.3 Modelling of disturbance sources

In the real world nothing works perfectly. Most components of the setup contribute a certain amount of noise to the loop, which will set a limit to the achievable performance of the system. Examples of noise sources are electrical noise sources, such as random voltage sources and current sources originating in electrical components, e.g., resistors and operational amplifiers. In Figure 3.9 the noise sources for this setup can be seen in a schematic. The ground vibrations *ground_vib* represent the ground vibrations entering the loop via the speaker base plate. The thermal noise from the coil of the geophone is denoted by *geocoil_noise*. *Brownian_noise* is a voltage noise caused by the Brownian motion of the proof mass. ADE and ADQ represent the A/D Converter (ADC) electrical and quantization noise respectively. (DAQ and DAE similar, only for a D/A converter). All these noise sources are modelled in the paragraphs below.

The Crown power amplifier has very low-noise characteristics. Its input equivalent standard deviation equals 1.3 μV_{rms} over a 20 Hz - 20 kHz bandwidth, according to the manufacturer's specifications. This will turn out to be so low compared to e.g., the DAE electrical noise (applying at the same location), that is is not accounted for in this analysis.

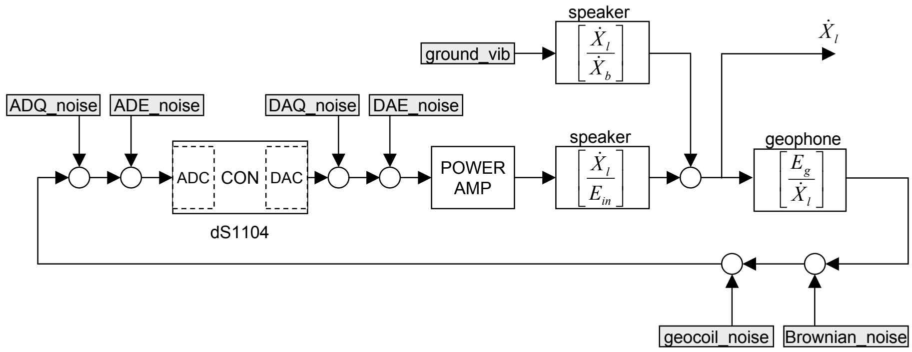

Figure 3.9 *A schematic of all the noise sources in the experimental setup.*

3.3.1 Measurements and model of ground vibrations

Using the HP35665 DSA the PSD $[V_{rms}^2/Hz]$ was measured of the output voltage of a geophone that was glued to the base plate of the setup (see Figure 3.1). To convert the obtained data to equivalent ground velocity data $[(m/s)^2/Hz]$, the PSD was divided by the squared magnitude of the geophone velocity sensitivity (3.3). The square root of the resulting equivalent ground velocity PSD data is called the Amplitude Spectral Density (ASD) $[m/s/\sqrt{Hz}]$ and can be seen in Figure 3.10 on the left hand side.

Remarkable is the steep rise around 2 Hz. Apparently, most of the power of the ground vibrations is located above this frequency. In the same figure the velocity equivalent channel noise of the HP35665 DSA is plotted. Comparing the ground vibration data with the channel noise, it can be concluded that the measured vibration data is not reliable below 1 Hz, because the magnitude of the channel noise exceeds the vibration data. (It is possible to overcome this channel noise problem, by pre-amplifying the geophone signal before it enters the DSA, as was done in Barzilai [2]).

The New High Noise Model (NHNM) and New Low Noise Model (NLNM) of Peterson [15] are also included for reference. It represents the largest and lowest seismic noise measured at seismometer stations across the globe. The seismic noise at the Precision Motion Control laboratory which in the midst of Boston city is expected to be in the order of the NHNM. The line parameters to construct the NHNM and NLNM curves can be found in Appendix B.2.

The ground velocity ASD is approximated with a 4^{rd} order transfer function, also shown in Figure 3.10. The model overestimates the acceleration level at most frequencies, especially in the 1 Hz and 30 Hz regions. The measurements are not reliable below 1 Hz, and the model is assumed to levels off in between the NHNM and NLNM, at $2 \cdot 10^{-7}\ m/s/\sqrt{Hz}$. The ASD model can be written as:

$$V_{vib}(s) = 2 \cdot 10^{-7} \left(\frac{\frac{3}{2\pi}s + 1}{\frac{3}{2\pi 7}s + 1} \right)^3 \left(\frac{\frac{100}{2\pi}}{s + \frac{100}{2\pi}} \right) \qquad [m/s/\sqrt{Hz}] \tag{3.7}$$

The model that approximates the ground velocity PSD can now be written as:

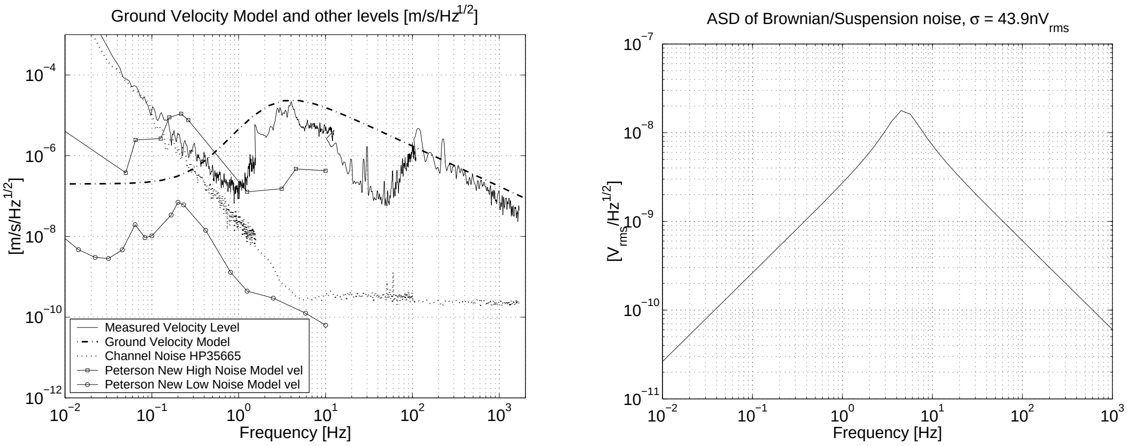

Figure 3.10 left*: ASD of the measured ground velocity level* $[m/s/\sqrt{Hz}]$ *and the obtained model* $V_{vib}(j\omega)$*, together with the channel noise of the HP35665. The New High/Low Noise Models of Peterson are shown for reference.* right*: ASD of the Brownian/Suspension noise expressed in geophone output voltage.*

$$S_{vib}(\omega) = V_{vib}(j\omega)V_{vib}(-j\omega) \qquad [(m/s)^2/Hz] \tag{3.8}$$

3.3.2 Sensor noise sources

Geophone coil thermal noise

Because the geophone coil has a certain resistance R_c $[\Omega]$, there will be thermal (also called Johnson) noise present at the output terminals of the geophone. The thermal noise of a conductor is described in Fish [7], and is the random voltage produced across the resistance R_c caused by the thermal agitation of electrons. Thermal or Johnson noise is a white noise source, having a constant PSD over frequency. The voltage PSD of thermal noise of the geophone coil is given by

$$S_{coil} = 4kTR_c = 6.47 \cdot 10^{-17} \qquad [V_{rms}^2/Hz] \tag{3.9}$$

where $k = 1.38 \cdot 10^{-23}$ J/K is the Boltzmann constant, and T is the room temperature in Kelvin, which is assumed to be 293 K.

Brownian noise

Because the proof mass is suspended in free air, air molecules constantly collide with it, causing the proof mass to follow a certain random path, called a Brownian motion. The Brownian motion of suspended objects is also referred to as *suspension noise.* The resulting motion of the proof mass can be modelled as an equivalent input acceleration spectrum as described in Usher [25, p505], Riedesel [17, p1728] and Rodgers [18, p1074]. The resulting acceleration PSD is constant over frequency and can be written as:

$$S_{acc} = 16\frac{\pi k T \zeta f_o}{m_g} = 1.45 \cdot 10^{-17} \qquad [(m/s^2)^2/Hz] \tag{3.10}$$

where k is Boltzmann's constant, T is the room temperature in Kelvin, ζ is the damping ratio of the geophone system, $m_g = 0.0236$ kg is the proof mass and $f_o = 4.8$ Hz is the geophone resonant frequency. In order to get a PSD in terms of geophone output voltage, this model is multiplied with the squared magnitude of the geophone acceleration sensitivity (3.4):

$$S_{sus}(\omega) = S_{acc}\left|\frac{G_g j\omega}{(j\omega)^2 + 2\zeta\omega_o j\omega + \omega_o^2}\right|^2 \qquad [V_{rms}^2/Hz] \tag{3.11}$$

The ASD $[V_{rms}/\sqrt{Hz}]$ of the suspension noise can be seen in Figure 3.10.

3.3.3 A/D and D/A electrical noise

Analog to Digital Converter electrical noise

When short circuiting the ADC input, the ideal output equals zero. In practice the output is not zero at all as can be seen in Figure 3.11 on the left hand side, where a time trace of the short circuited ADC is shown. The ADC of the dS1104 board uses a 16 bit converter, and was running at a sampling rate of 20 kHz. The range of this converter is fixed to $\pm 10\ V_{peak}$, giving it a total range of 20 V_{pp}. The least significant bit (lsb) equals to $20/2^{16} = 0.305\ mV$. The output of the short circuited ADC standard deviation was 1.35 bits, or, expressed in volts, $\sigma_{A/D\ elec} = 0.412\ mV_{rms}$. The PSD representing the A/D electrical noise is flat and defined up to the Nyquist frequency $F_n = 10$ kHz:

$$S_{ade} = \frac{\sigma^2_{A/D\ elec}}{F_n} = 1.7 \cdot 10^{-11} \qquad [V_{rms}^2/Hz] \tag{3.12}$$

Digital to analog converter electrical noise

A Digital to Analog Converter (DAC) with a zero input, ideally has a zero output. As is to be expected, in practice the output is not zero, but is contaminated with noise. The DAC output was measured an had a standard deviation of $\sigma_{D/A\ elec} = 0.12\ mV_{rms}$ and had white noise characteristics. The PSD representing the D/A electrical noise is flat and defined up to the Nyquist frequency F_n:

$$S_{dae} = \frac{\sigma^2_{D/A\ elec}}{F_n} = 1.4 \cdot 10^{-12} \qquad [V_{rms}^2/Hz] \tag{3.13}$$

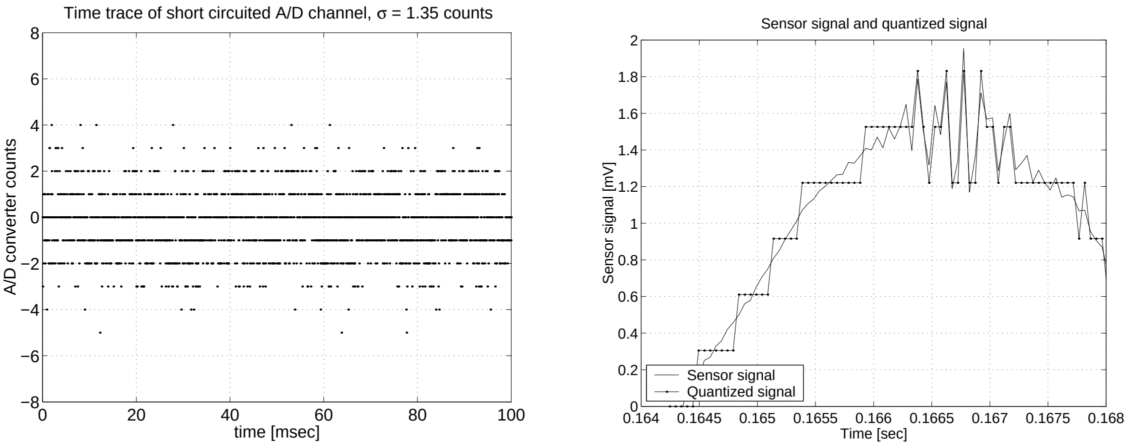

Figure 3.11 left: *Time trace of the A/D electrical noise of a dS1104 controller board. The signal value was multiplied with a factor* $2^{16}/20$, *making one unit in the graph correspond to one count of the converter.* right: *Time trace of a typical sensor signal, with a sampled and quantized version of the same signal, simulating an A/D conversion. At every sample instant a quantization error is made. defined as the mismatch between the true signal value and the quantized signal value. To quantize the signal value, the true value is rounded off towards toe nearest integer multiple of the lsb value of* $0.305\ mV$.

3.3.4 A/D and D/A quantization noise

A/D quantization noise

When a sensor signal enters an Analog to Digital Converter (ADC) a quantization error is introduced. At every sample instant, every 0.05 msec, a sample is taken which is then to be quantized by the ADC. Since only a limited set of bits are available, the sampled value must be rounded off towards the nearest multiple of the least significant bit (lsb) value of 0.305 [mV], introducing a quantization error as is illustrated in Figure 3.11 on the right hand side. Oppenheim [13] treats the quantization error as uniformly distributed zero mean white noise. This simple model is accurate enough in this case study, since the quantization error is small compared to the A/D electrical noise and they apply at the same location in the loop. The model describes the theoretical variance of the error and can be written as:

$$\sigma^2_{A/D\ quant} = \frac{\text{lsb}^2}{12} \qquad [V^2_{rms}] \tag{3.14}$$

Using the lsb value of $0.305\ mV$ and taking the Nyquist frequency into account, this leads to the following model:

$$S_{adq} = \frac{\sigma^2_{A/D\ quant}}{F_n} = 7.8 \cdot 10^{-13} \qquad [V^2_{rms}/Hz] \tag{3.15}$$

D/A quantization noise

Every output signal send to the DAC, is quantized in the same way as the A/D quantization, introducing a quantization error similar as with the ADC quantization. Since the DAC has the same lsb value as the ADC, the same model as for the A/D quantization noise can be used:

$$S_{daq} = S_{adq} = 7.8 \cdot 10^{-13} \qquad [V_{rms}^2/Hz] \tag{3.16}$$

3.4 Performance analysis

In order to analyze the system performance, the PSD of the performance output $\dot{X}_l$ will be simulated. Besides the PSD of the performance output, one can look at the PSD of the control output u, which reveals the amount of control effort needed to achieve the performance level.

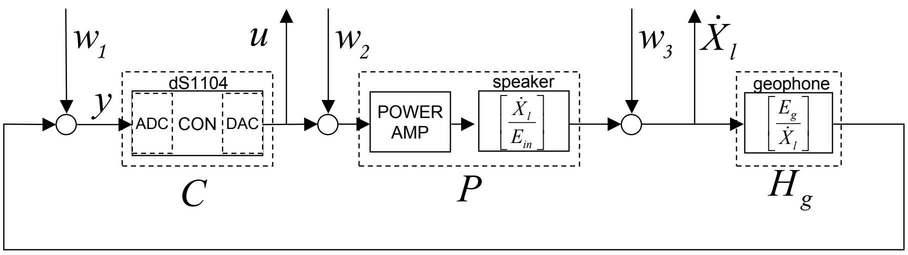

Figure 3.12 *Closed loop input-output configuration.*

In Figure 3.12 the inputs w_1-w_3 and outputs u and $\dot{X}_l$ can be seen. The closed loop transfer function from these inputs towards the outputs is denoted with $H(j\omega)$ and can be written as:

$$\begin{bmatrix} u \\ \dot{X}_l \end{bmatrix} = \underbrace{\begin{bmatrix} CS & CH_gPS & CH_gS \\ PCS & PS & S \end{bmatrix}}_{H(j\omega)} \begin{bmatrix} w_1 \\ w_2 \\ w_3 \end{bmatrix} \tag{3.17}$$

where C is the controller, S the closed loop sensitivity function, P equals $P_{speaker}$ and H_g the geophone velocity sensitivity P_{geo}, see Figure 3.12. The PSDs at the ith disturbance input, $S_{w_i}(\omega)$ simply equals the linear sum of the noise PSDs applying at that input, so:

$$\begin{aligned} S_{w_1} &= S_{coil} + S_{sus} + S_{ade} + S_{adq} \\ S_{w_2} &= S_{dae} + S_{daq} \\ S_{w_3} &= S_{vib}(\omega) \left|P_{sp\_vib}(j\omega)\right|^2 \end{aligned} \tag{3.18}$$

All the output PSDs and corresponding CPSs can now be calculated using Equation (2.15) and their corresponding ASDs and CASs can be seen in Figure 3.13. Not only the total output ASDs/CASs are shown, but also the contribution of every separate source by itself, such that one can analyze how much power each source is contributing to the total power over frequency.

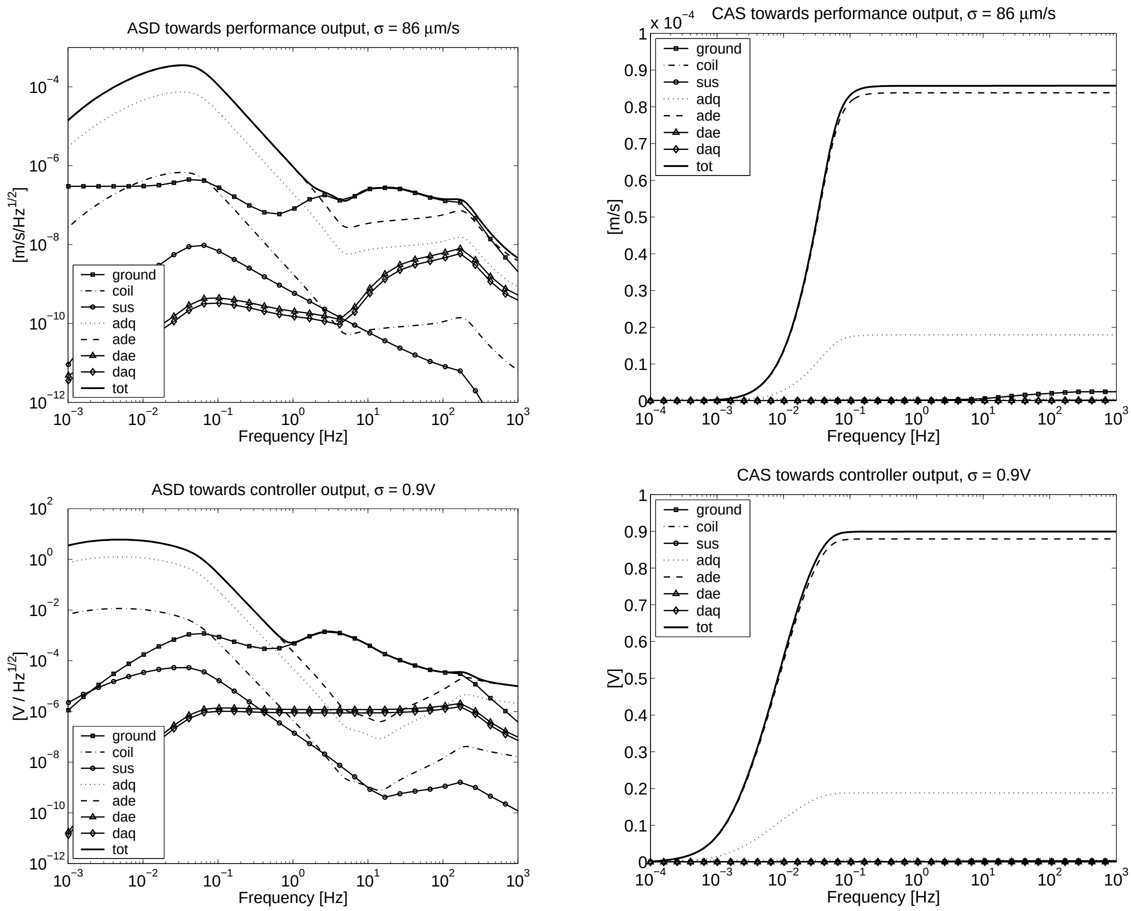

Figure 3.13 *Simulation of performance output spectra ($\dot{X}_l$) and the controller output spectra (u) using the 100 mHz controller (3.5).* above*: Simulated ASD (*left*) and CAS (*right*) of the performance signal $\dot{X}_l$.* below*: Simulated ASD (*left*) and CAS (*right*) of the control signal u.*

In the simulated performance ASD, one can see that there is a large power contribution in the lower frequency region, mainly due to the two A/D noise sources S_{ade} and S_{adq}. The simulated performance CAS confirms this, since it shows a steep rise in power between 0.01 Hz and 0.1 Hz and levels of at 86 $\mu m/s$, which is the 1-σ value of the closed loop load velocity. In the time domain this can be interpreted as follows: the cone plate moves up and down in a 10 sec - 100 sec period, causing the payload to drift.

Furthermore, one can analyze the vibration isolation performance. In the performance ASD it can be seen that the ground vibrations are the dominant noise sources in a very small frequency span from 5 Hz up to 200. The fact that other noise sources dominate the performance CAS, tells us that the isolation system itself contributes more power to the performance output at these frequencies, that the ground vibrations themselves. The open loop performance value (1-σ) equals 98.8 $\mu m/s$, so closing the loop of the isolator only increases the performance to 86 $\mu m/s$.

From the simulated ASD and CAS of the control signal, one can conclude almost all the control effort is put in 'controlling' the two dominant noise sources. In the ideal situation (no other noise sources than the ground vibrations), all the control effort is due to the ground vibrations. The standard deviation of the control signal equals 0.9 V_{rms}, and almost all its power is located in the 0.001 Hz - 0.1 region, meaning that the control output is slowly (about 100 sec) drifting up and down several volts. For comparison, the part of the control signal that is used to isolate for ground vibrations has a standard deviation of 3 mV_{rms} (too small to be visible in this CAS).

The cause of the damage done by these two sources, is the low Signal to Noise Ratio (SNR) at the location where these noise sources apply (The SNR is defined as $10 \cdot \log(\sigma_s^2/\sigma_n^2)$ [dB] or equally $20 \cdot \log(\sigma_s/\sigma_n)$ [dB]). The noise sources are both located in between the geophone and the A/D converter as can be seen in Figure 3.9. To improve the performance of the isolator, the SNR at this location should be improved. This can be done by using a preamplifier, as is discussed in the next section.

3.5 Using a preamplifier

3.5.1 Introduction preamplifier

From the performance analysis in the previous section it was concluded that the Signal to Noise Ratio (SNR) of the signal entering the ADC is far too low. There are two ways to overcome this problem.

First, one can try to decrease the magnitude of the noise sources. There is a possibility to decrease the A/D quantization noise by adjusting the range of the converter, such that it better matches the magnitude of the closed loop sensor signal. At the start-up of the system though, the geophone output is in the order of a few millivolts, whereas in the closed loop case it is in the order of a few tenths of millivolts. A dual range ADC would overcome this problem, but unfortunately, the magnitude of the A/D electrical noise does not decrease when the range of the converter is decreased, since it originates in the electronics within the converter itself.

A second option to solve this problem is to pre-amplify the sensor signal before it enters the ADC, increasing the signal level. Although a preamplifier can be used to improve the SNR, the preamplifier itself introduces noise sources as well! One has to find out if the pre-amplification of the sensor signal indeed counter balances the newly introduced noise sources and thus improves the system performance. This will be the topic of this section. The system configuration with a preamplifier included can be seen in Figure 3.14.

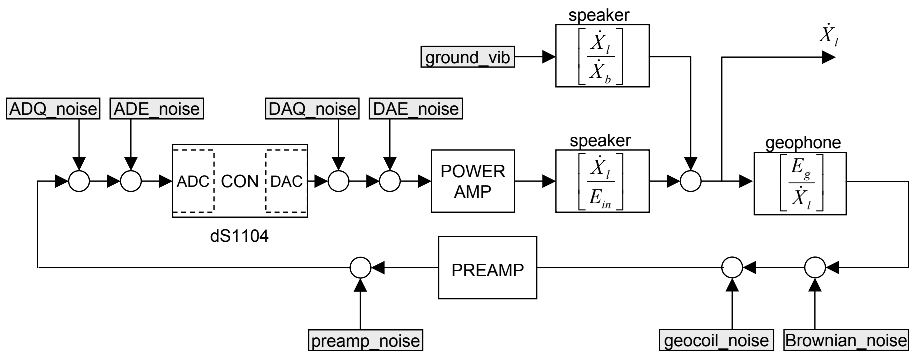

Figure 3.14 *System configuration with a preamplifier included and noise sources.*

3.5.2 Preamplifier transfer function

As can be seen in Figure 3.15 on the left hand side, the amplitude of the geophone velocity sensitivity drops off towards the lower frequencies with a +2 rate. As a consequence, input signals in this low frequency region will generate a very small output voltage and will therefore be more sensitive to noise sources. In order to improve the SNR in that frequency region it seems to make sense to amplify this low frequency region more than the high frequency part. Therefore, the preamplifier transfer function is chosen to be a second order lag filter, as can be seen in Figure 3.19 on the right hand side. The improved 'velocity sensitivity' of the geophone in series with the preamplifier can be seen in Figure 3.15 on the left hand side.

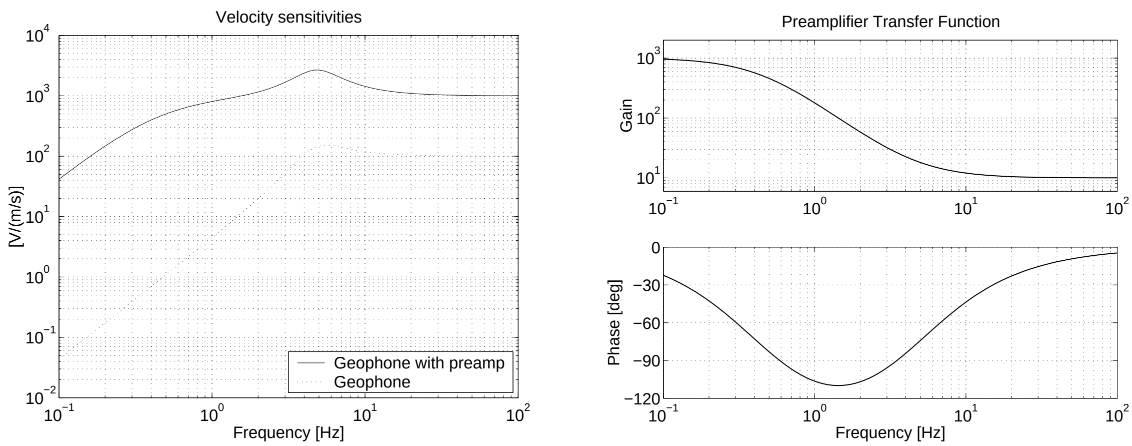

Figure 3.15 left*: The velocity sensitivities of the geophone and of the geophone in series with the preamplifier.* right*: Transfer function of the preamplifier.*

The output voltage signal of the preamplifier is denoted by E_{out}. Its input signal is the geophone output E_g. The transfer function of the used preamplifier can be written as a series connection of two first order lag filters:

$$\frac{E_{out}}{E_g} = G_{pa}\left(\frac{\tau_p s + 1}{\alpha_p \tau_p s + 1}\right)^2 \tag{3.19}$$

with $G_{pa} = 1000$, $\tau_p = 1/\omega_1 = 1/(2\pi\ 0.45)$ and $\alpha_p = 10$, which puts the corner frequencies at 0.45 hz and 4.5 Hz. The preamp now has a low frequency gain of 1000 and a high frequency gain of 10 and will be referred to as the '1000-10 preamp'.
This preamplifier was physically build using an operational amplifiers in both preamplifier stages. The physical configuration of the circuit and the derivation of the transfer function in terms of the physical components can be found in Appendix B.3.

3.5.3 Preamplifier noise model

The noise model of the preamplifier developed here, is based on the models developed in Rodgers [18], [19], Riedesel (*et al.*) [17] and Horowitz and Hill [10]. The physical preamplifier is build as series connection of two separate, first order stages. The output of the first and second stage are denoted with $E_{out,1}$ and E_{out} respectively. The two stages have transfer functions:

$$\frac{E_{out,1}}{E_g}(s) = 100\left(\frac{\tau_p s + 1}{\alpha_p \tau_p s + 1}\right) \quad , \quad \frac{E_{out}}{E_{out,1}}(s) = 10\left(\frac{\tau_p s + 1}{\alpha_p \tau_p s + 1}\right) \tag{3.20}$$

In Figure 3.16 a schematic of the first stage can be seen with all its noise sources included. (The geophone-coil noise has been left out, since it is already accounted for in S_{coil}).

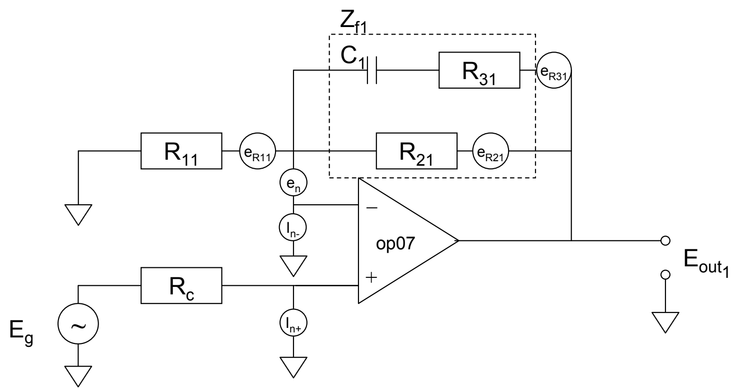

Figure 3.16 *First stage of the preamplifier and all its noise sources*

The current noise sources, i_{n-} and i_{n+} of the operational amplifier, are shown as Norton generators from the inverting and non inverting inputs to ground. The voltage noise source of the operational amplifier e_n is shown as a Thevenin generator in series with the summing junction at the intersection of R_{11} and Z_{f1}. The preamplifier is build using the op07 low-noise operational amplifier and its noise characteristics can be found in the manufacturer specifications.

The noise sources $e_{R_{11}}$, $e_{R_{21}}$, and $e_{R_{31}}$ are due to thermal noise of the resistors and are included in series with the resistors. The total noise model at the output of the first stage will be denoted by $S_{pa,1}(\omega)$ and will not be written out here, and its derivation can be found in Appendix B.4. For the second stage a similar output noise model can be developed, and will be denoted by $S_{pa,2}(\omega)$. The total noise model at the output of the preamplifier $S_{pa}(\omega)$ can now be written as:

$$S_{pa}(\omega) = S_{pa,1}(\omega)\left|\frac{E_{out,1}}{E_g}(j\omega)\right|^2 + S_{pa,2}(\omega) \qquad [V_{rms}^2/Hz] \tag{3.21}$$

The preamplifier noise model $S_{pa}(\omega)$ and the separate terms on the right hand side of (3.21) can be seen in Figure 3.17. To validate this noise model, the output of the preamplifier with short circuited input was measured using the HP35665 analyzer. The result can also be seen in Figure 3.17. The measurements match the theory very well, except in the low frequency region (<1 Hz) and at 60 Hz, where a clear '60 Hz pick-up' noise peak can be seen. The overestimation of the low frequency noise and the un-modelled 60 Hz pick up peak will be subject of discussion later in this chapter.

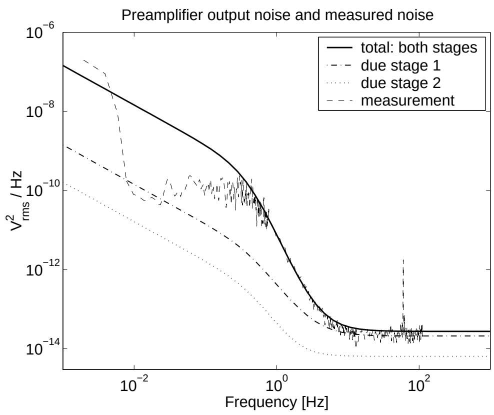

Figure 3.17 *Total preamplifier noise model PSD $S_{pa}(\omega)$ and the two separate contributions of the preamp stages at the preamplifier output, together with the measured noise. The noise model matches the measured noise very well in the 1 Hz - 100 Hz region except for the pick up peak at 60 Hz. The noise model overestimates the noise model in the low frequency region (<1 Hz).*

3.5.4 Performance analysis using a preamplifier

To make the performance comparable with the previous non-preamp case, the controller is chosen such that the loop gain transfer function $L(s)$ remains the same. This was done by multiplying the controller (3.5) used in the non-preamp case (see Section 3.4) with the inverse of the preamplifier transfer function (3.19). The output ASD's and CAS's are calculated as was done in the non-preamp case, and can be seen in Figure 3.18.

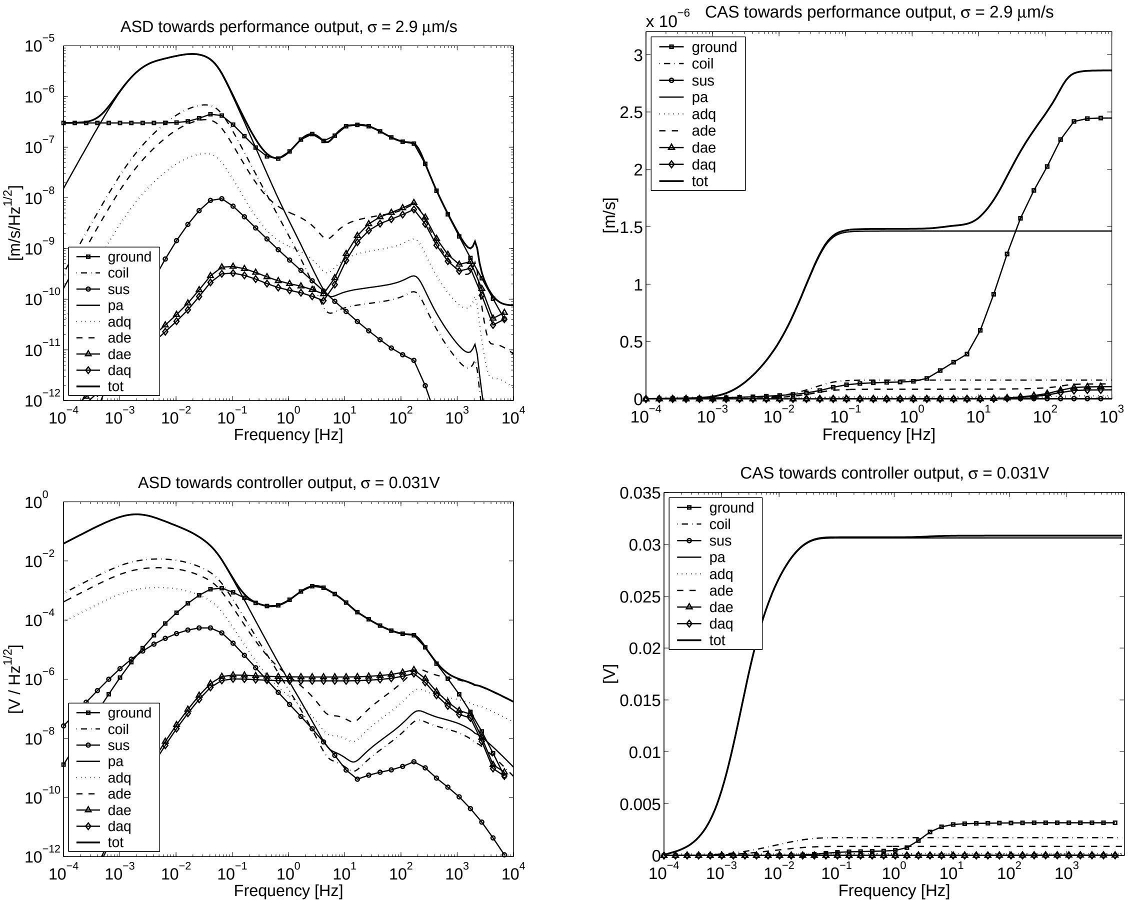

Figure 3.18 *Simulation of performance output spectra ($\dot{X}_l$) and the controller output spectra (u) using the 1000-10 preamplifier and a controller such that the loop transfer function $L(s)$ is the same as the in the non-preamp case (see Figure 3.8).*above*: Simulated ASD (*left*) and CAS (*right*) of the performance signal $\dot{X}_l$.* below*: Simulated ASD (*left*) and CAS (*right*) of the control signal u.*

The performance ASD in Figure 3.18, shows that the magnitude of the contribution of the ADC noise sources is now much smaller compared to the non-preamp case (see Figure 3.13), due to the use of the preamplifier. As a price though, preamplifier noise is introduced. The preamp noise dominates the ASDs in the low frequency region, but at a much lower level than was the case with the ADC noise sources in the non-preamp case. Apparently, the introduction of the preamplifier indeed counter balances the introduction of its own noise. The standard deviation of the performance output dropped from 86 $\mu m/s$ to 2.9 $\mu m/s$, a performance increase with a factor 30!

The control effort dropped from 0.89 V_{rms} in the non-preamp case to 31 mV_{rms} in this case. The preamplifier noise is now the major contributor to the control effort, accounting for 90 % of the control effort, meaning that the system is still mainly compensating for its own noise, instead of for ground vibrations. Because the power of the controller output is mainly located in the 0.001 Hz - 0.1 region, the controller output will slowly drift up and down circa 50 mV causing the platform to make a slow drifting motion. This causes undesired system behavior, since there is the risk that the platform will reach its physical travel limits.

Using the analysis tools available, one can try to find possible improvements that could be made to avoid the controller output to have its power located mainly in the low frequency region. The most straight forward approach is to decrease the amount of low frequency noise generated by the preamplifier. Since the low frequency noise is caused by the inherent 1/f noise of the opamps, this is hard to achieve with the current circuit configuration. On the other had, one can look at the closed loop transfer function from preamp input to controller output; $C \cdot S$ (not shown here). One can see that this transfer has a huge gain in the 0.001 Hz - 0.1 region, due to the controller used. This huge controller gain is needed to achieve the 0.1 Hz bandwidth. This analysis raises the question if the desire to have this 0.1 Hz bandwidth is a good idea concerning the effect is has on the propagation of the low frequency preamp noise.

This points out a degree of freedom in the DEB design approach: the control strategy used. The controller defines the closed loop transfer function $H(j\omega)$ and thus the propagation of the disturbances towards the outputs. The designer can use this degree of freedom, in order to optimize for performance. This topic is discussed in Chapter 4.

As mentioned earlier in § 3.5.3, the preamplifier noise model (see Figure 3.17) overestimates the measured noise in the low frequency region. Since it is this part of the preamp noise spectrum that causes the huge power contribution to the controller output, one can say that the results of the performance simulation are therefore not reliable in the low frequency region. In order to get a more reliable picture of the effect of the low frequency preamplifier noise, the propagation should be done with the actually measured noise. This will be done in the next section.

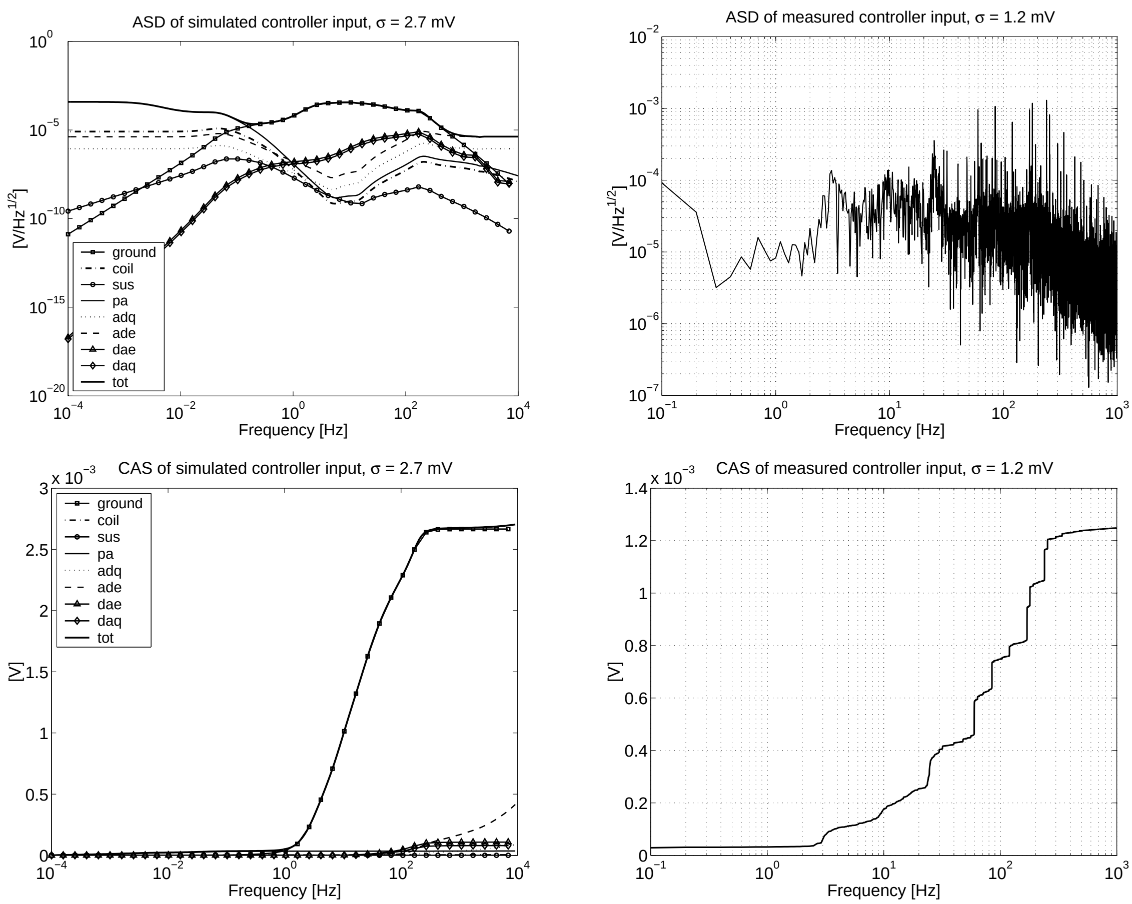

Figure 3.19 *Validation of the controller input y spectra using the 1000-10 preamplifier.* above*: Simulated ASD (*left*) and measured ASD (*right*) of the controller input signal.* below*: Simulated CAS (*left*) and measured CAS (*right*) of the controller input signal.*

3.6 Experiments and comparison with theory

In this section it is tried to close the gap between the theoretical and experimental results. It is chosen to validate the noise levels of the closed setup at the controller input, right after the ADC. This signal can be comfortably 'measured' inside the computer, avoiding the introduction of new measurement noise sources. The simulated and measured results can be seen in Figure 3.19. From the simulated and measured CAS in this figure one can see that the simulated controller input has a standard deviation $\sigma = 2.7\ mV_{rms}$ and the measured input has a deviation of $\sigma = 1.2\ mV_{rms}$.

In the simulated CAS of the controller input (Figure 3.19 below left) one can see that the ground vibrations account for the majority of the controller input power. Because the ground vibration model $V_{vib}(\omega)$ (see Figure 3.10 on page 29) overestimates the measured vibration

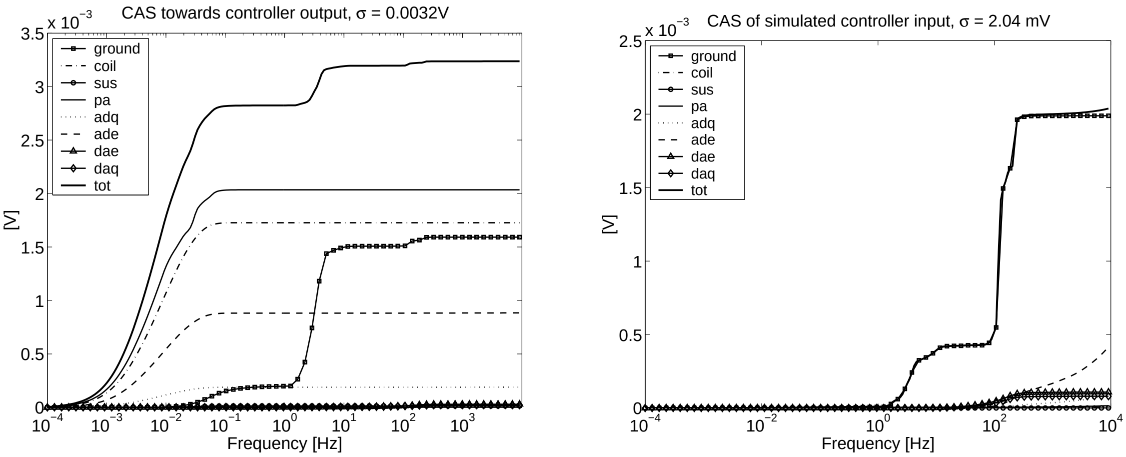

Figure 3.20 *Simulation results using the actually measured ground vibration spectrum and preamplifier noise spectrum.* left*: Simulated CAS of the controller output (compare with Figure 3.18, below right).* right*: Simulated CAS of the controller input (compare with Figure 3.19, below left).*

level at certain frequency regions, the simulated result is likely to overestimate the power in the controller input signal.

In the measured CAS (Figure 3.19 below right) electrical pick up noise can be identified as stepwise increases in power at 60 Hz, 120 Hz, 180 Hz and 240 Hz. This pick up can be the result of electromagnetic/static noise sources which are not accounted for in this analysis. From the measurements, shown in Figure 3.17 on page 37, one can see that the preamplifier noise spectrum shows a clear 60 Hz pick up peak. One might expect that part of the pick up noise is due to the preamplifier. Looking at the simulated ASD in Figure 3.19 though, it can seen the preamp noise lies far below the DAC and ADC sources. This means that the DAC and ADC are the most sensitive to pick up noise (concerning the effect it can have on the controller input), and that it is less likely that the pick up noise measured at the controller input, including the 120, 180 and 240 Hz pick up peaks, can be attributed to the preamplifier electrical circuitry. The magnitude of the pick up noise can be reduced by applying electrical/magnetic shielding to the electrical circuitry and careful cabling. If the pick up remains to have a significant impact, one should account for them in order to increase the prediction accuracy. Discarding the power due to electrical pick up, the measured level would be around 0.8 mV_{rms}. This value will be used to compare with the theoretically obtained results.

In order to increase the prediction accuracy of the simulation, the simulation is done again with the actually measured preamplifier noise and measured ground vibration spectra. Not all results are shown, only the CAS of the controller output and the the CAS of the controller input, which can be seen in Figure 3.20.
The simulated CAS of the controller output using the measured preamplifier noise and ground vibration level shows a drastic decrease in predicted controller output power when

compared with the simulation results using the actual noise models (see Figure 3.18 below right); instead of 31 mV_{rms} the predicted controller output decreased to 3.2 mV_{rms}, indicating that the prediction done in the previous section was indeed not reliable. This result shows the importance of accurate disturbance modelling, especially when the disturbance is the dominant source at the output.
The simulated CAS of the controller input in Figure 3.20 shows that ground vibration still contribute the majority of the power. In this figure one can see that more than half of the power (about 1.3 mV_{rms}) is now added at 120 Hz and 240 Hz. Looking at the measured ground vibration spectrum in Figure 3.10 on page 29 one can see that it indeed contains two power peaks at these frequencies. However, these rather large increases in power are not visible in the measured CAS of the controller input! A reason for this discrepancy can be the following: the peaks in the measured ground vibration level are due pick up noise in the measurement circuit and do not represent ground vibrations. When leaving out the contribution due to this measurement pick up noise, the simulated controller input level would be around 0.7 mV_{rms} which matches up well with the measured controller input level of 0.8 mV_{rms} where the pick up noise also has been left out.

Summarizing, the theoretical results match the measured results if the simulation is done with the actual measured disturbance spectra and the power contribution thought to be due to electrical pick up noise are left out of the comparison.
The predicted performance in terms of $\dot{X}_l$ drops from 2.9 $\mu m/s$ when using the disturbance models (see Figure 3.18) to about 0.8 $\mu m/s$ when using the measured spectra and the power due to the measurement pick up noise in the ground vibration spectrum is discarded.

3.7 Conclusions and recommendations

3.7.1 Conclusions

The improved vibration isolation setup is successfully build and made operational. The system was modelled using theoretical modelling and standard identification techniques. By means of experiments, the existence of magnetic coupling between the voice coil of the speaker and the coil of the geophone is shown. With the use of a magnetically shielded geophone the coupling could be eliminated.

All the (stochastic) disturbance thought to act on the setup are modelled by either measurement of their PSD or by theoretical modelling. Using these models in the DEB simulation tool, the error (or performance) of the open and closed loop system is predicted, resulting in σ = 98.8 $\mu m/s$ resp. σ = 86 $\mu m/s$ (1-σ). By analyzing the DEB simulation results the performance limiting factors could be identified; the disturbances introduced by the AD converter turned out to be the absolute dominant contributors to the error. The system could be improved by introducing a preamplifier before the AD converter in the loop. The DEB simulations show a huge performance improvement; a closed loop performance level of (theoretically) 2.9 $\mu m/sec$! These results show that, using the DEB approach, the designer is indeed able to predict the performance of a system concept and to gain insight in the performance limiting factors of the system.

To validate the prediction accuracy of the DEB approach, simulated results are compared with experimental results; the closed loop controller input level was simulated and measured. The simulations showed that the almost all the power of the controller input signal was due to ground vibrations. The measured results showed a significant amount of electrical pick up noise which was not accounted for in the DEB analysis. The simulated results matched the experimentally measured level when the simulations were done with the actual measured ground vibration spectra (the model representing the measured ground vibrations was too inaccurate) and the power due to electrical pick up noise in the measured controller input (which accounted for 30 % of the measured power) were discarded. This result shows that the predicted results by the DEB approach can be accurate if realistic disturbance models are used and electrical pick up noise is accounted for.

3.7.2 Recommendations

To increase the predicting accuracy of the DEB analysis the dominant disturbance sources should be measured very accurately (if a prototype is available) and it is then strongly recommended to use the actual measured spectra in the simulations. For this case study, better measurements of the ground vibrations should be made e.g., by averaging several measurements over longer periods of time and taking special care not to contaminate the measurement with electrical pick up noise.

To further increase the prediction accuracy, effort should be put in to identify and model the electrical pick up noise sources that act on the closed loop system and account for them to the DEB analysis. If possible, electrical pick up noise should be avoided by careful electrical circuit design, grounding and cabling.

If there remains to be a discrepancy between the theoretical and measured output PSD, a way to deal with it is to accredit the difference to an additional (artificial) disturbance, such that the difference in output power is contributed by this input disturbance. In this way the designer has a possibility to account for this difference in power in the simulations.

Chapter 4

$\mathcal{H}_2$ control in active vibration isolation

4.1 Introduction

When a system designer has designed different system concepts, he needs to find out which concept is the most promising. In order to compare the performance of these different concepts, the system designer needs an objective measure of performance. In this thesis an objective measure is interpreted as follows: the same amount of control effort should be used for each different system concept and the used controller should push the system to its maximum performance level given the system and disturbance models.

As is explained in Section 2.5, the $\mathcal{H}_2$ control strategy (theoretically) offers the system designer the opportunity to put a constraint on the amount of control effort used, while maximizing the performance of the system. So, $\mathcal{H}_2$ control offers the ability to objectively compare different system concepts and can be seen as an extension of the DEB design approach. The goal of this chapter is to find out if the use of $\mathcal{H}_2$ control indeed adds value to the DEB approach in practice, by applying it to the case study of Chapter 3.

In this chapter an $\mathcal{H}_2$ controller will be synthesized for the system concept using the preamplifier developed in the previous chapter. The disturbance models developed in Chapter 3 are used to obtain the weighting filters needed for $\mathcal{H}_2$ controller synthesis in § 4.2.1. In § 4.2.2 it is taken care of that the weighting filters meet the standard assumptions as discussed in Appendix A.2. Then the $\mathcal{H}_2$ controller is synthesized and compared with old controller (3.5) and the Pareto curve is calculated. In Section 4.3 the performance is simulated and compared with experimental results. Next, in Section 4.4 it is tried to find out what the best preamplifier design is by comparing the Pareto curves using different preamplifiers.

4.2 Design of an $\mathcal{H}_2$ controller

4.2.1 Weighting filters for the 10-1000 preamp case

When designing an $\mathcal{H}_2$ controller for the 10-1000 preamp configuration all the noise sources and disturbances models obtained in the previous chapter can be used to obtain the weighting filters. The chosen configuration of the weighting filters can be seen in Figure 4.1.

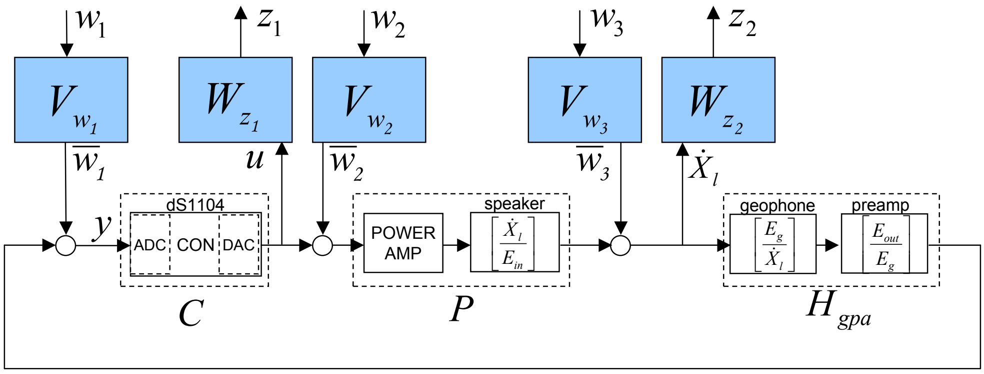

Figure 4.1 *Configuration of the weighting filters V_{w_1}, V_{w_2}, and V_{w_3} for $\mathcal{H}_2$ controller design. Two outputs are defined, a control effort output u with scaling filter W_{z_1} and a performance output ($\dot{X}_l$) with scaling filter W_{z_2}.*

The weighting filter V_{w_1} accounts for five noise sources; the two sensor noise sources S_{coil} and S_{sus}, the preamp noise source S_{pa} and the ADC noise sources S_{ade} and S_{adq}. The two sensor noise sources must be propagated to the location where the disturbance signal w_1 applies, by multiplying them with the squared magnitude of the preamplifier transfer function. The PSD of the fictional disturbance signal w_1 can then be written as:

$$S_{w_1}(\omega) = (S_{coil} + S_{sus}) \left| \frac{E_{out}}{E_g}(j\omega) \right|^2 + S_{ade} + S_{adq} + S_{pa} \tag{4.1}$$

and the weighting filter $V_{w_1}(j\omega)$ equals the spectral factorization of $S_{w_1}(\omega)$. A way to avoid the problem of obtaining a spectral factorization is to make a least square fit on the square root of a frequency response data of $S_{w_1}(\omega)$ (so directly on ASD data) on a certain grid. This approach is followed using the MATLAB® command `fitmag` and the resulting 6^{th} order weighting filter $V_{w_1}(s)$ can be seen in Figure 4.2.

$$\begin{aligned} V_{w_1}(s) &= 4.22 \cdot 10^{-6} \frac{(s+0.57)(s+1.43\cdot 10^{-3})}{(s+0.187)(s+4.56\cdot 10^{-2})} \cdot \\ &\quad \frac{(s^2+9.95\cdot 10^{-2}s+2.93\cdot 10^{-3})(s^2+8.63s+31.0)}{(s+1.75\cdot 10^{-2})(s+1.45\cdot 10^{-3})(s^2+3.95s+3.98)} \quad [V_{rms}] \end{aligned} \tag{4.2}$$

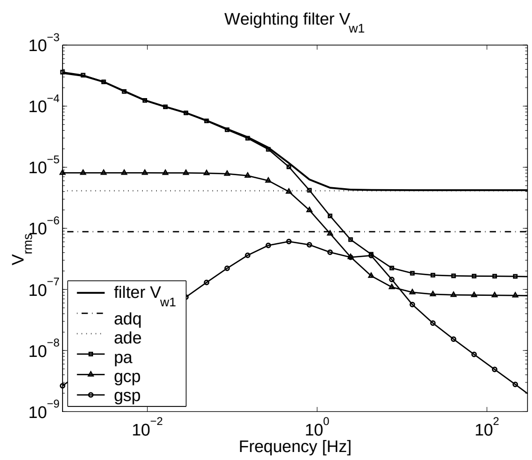

Figure 4.2 *The weighting filter $V_{w_1}(s)$. The filter is a least square fit to square rooted values of $S_{w_1}(\omega)$ on a certain frequency grid.*

To obtain $V_{w_2}(s)$ a similar approach can be followed. $V_{w_2}(s)$ accounts for the two DAC noise sources S_{dae} and S_{dae}, which are both constant over frequency (see Section 3.3), and thus V_{w_2} is easily calculated by hand as:

$$V_{w_2} = 1.48 \cdot 10^{-6} \quad [V_{rms}] \tag{4.3}$$

The third filter accounts only for the ground vibrations and is given by the floor noise model $V_{vib}(j\omega)$ (3.7) multiplied with the open loop speaker model $P_{sp\_vib}(s)$ (3.2):

$$V_{w_3}(s) = V_{vib}(s)\ P_{sp\_vib}(s) \quad [V_{rms}] \tag{4.4}$$

The two output scaling filter W_{z_1} scales the controller output u and W_{z_2} scales the performance output $\dot{X}_l$. Actually, only their ratio is of importance. They are given the values:

$$W_{z_1} = 1, \qquad W_{z_2} = 1 \cdot 10^5 \tag{4.5}$$

In § 4.2.4 it is explained why these particular values are chosen.

4.2.2 Meeting the standard assumptions

As discussed in Appendix A.2, the open loop system, including the weighting filters, has to meet the standard assumptions. From Figure 4.1 one can see that the open loop system can be written as:

$$
\begin{aligned}
\begin{bmatrix} z_1 \\ z_2 \\ \cdots \\ y \end{bmatrix} &= \begin{bmatrix} 0 & 0 & 0 & \vdots & W_{z_1} \\ 0 & W_{z_2}PV_{w_2} & W_{z_2}V_{w_3} & \vdots & W_{z_2}P \\ \cdots & \cdots & \cdots & & \cdots \\ V_{w_1} & H_{gpa}PV_{w_2} & H_{gpa}V_{w_3} & \vdots & H_{gpa}P \end{bmatrix} \begin{bmatrix} w_1 \\ w_2 \\ w_3 \\ \cdots \\ u \end{bmatrix} \\
&= \begin{bmatrix} G_{11} & G_{12} \\ G_{21} & G_{22} \end{bmatrix} \begin{bmatrix} w_1 \\ w_2 \\ w_3 \\ \cdots \\ u \end{bmatrix}
\end{aligned} \tag{4.6}
$$

corresponding to Figure 2.4 on page 16 (repeated in Appendix A.2 as Figure A.1). For the open loop plant to meet the standard assumptions, implies the following:

Assumption 1: D_{11} must be 0

The direct feedthrough from w to z, D_{11} must be zero. Since four of the six are already zero, we only have to pay attention to the remaining two. The two transfer functions $W_{z_2}PV_{w_2}$ and $W_{z_2}V_{w_3}$ must have high frequency roll-off such that D_{11} equals zero. To meet this assumption, the filter V_{w_2} and V_{w_3} are adjusted to have high frequency roll-off. When the roll-off is given well beyond the bandwidth (which is ca. 200 Hz) of the system, it will not influence the performance analysis. Both the filters are multiplied with a first order transfer function which has its cut-off frequency at 1 kHz:

$$
V_{w_2}(s) = 1.48 \cdot 10^{-6} \left(\frac{1}{\frac{1}{2\pi 1000}s + 1} \right) \quad [V_{rms}] \tag{4.7}
$$

$$
V_{w_3}(s) = V_{vib}(s)\ P_{sp\_vib}(s) \left(\frac{1}{\frac{1}{2\pi 1000}s + 1} \right) \quad [V_{rms}] \tag{4.8}
$$

Assumption 2 and 3: (A, B_2) is stabilizable and (A, C_2) is detectable

In a well defined plant (stabilizable and detectable), the only uncontrollable or unobservable unstable modes can come from the weighting filters. Since none of the weighting filters have unstable poles, this assumption is met.

Assumption 4: D_{12} has full column rank

The matrix D_{12} denotes the direct feedthrough matrix of G_{12}, the transfer function from the control signal u to the controlled output z:

$$
G_{12} = \begin{bmatrix} W_{z_1} \\ W_{z_2}P \end{bmatrix} \tag{4.9}
$$

When one of the matrices has full column rank the assumption is met. Since W_{z_1} is a nonzero scalar, this assumption is met.

Assumption 5: D_{21} has full row rank

The matrix D_{21} denotes the direct feedthrough matrix of G_{21}, the transfer function from noise and disturbance signals w to controller input y:

$$G_{21} = \left[\begin{array}{ccc} V_{w_1} & H_{gpa} P V_{w_2} & H_{gpa} V_{w_3} \end{array} \right] \tag{4.10}$$

When one of the matrices has full row rank the assumption is met. Since $V_{w_1}(j\omega)$ is nonzero for $\omega \in R \cup \infty$ this assumption is met.

Assumption 6 and 7

When these assumptions are not met the plant has poles on the imaginary axis or one of the transfer functions G_{12} or G_{21} has transmission zeros. This is not the case so the assumption is met.

4.2.3 Closed transfer functions using an $\mathcal{H}_2$ controller

The weighting filters are build and all the assumptions are met. An $\mathcal{H}_2$ controller can now be synthesized. The resulting transfer functions can be seen in Figures 4.3 and 4.4. The transfer functions when using the 100 mHz controller (3.5) developed in § 3.2.5 are also shown for comparison.

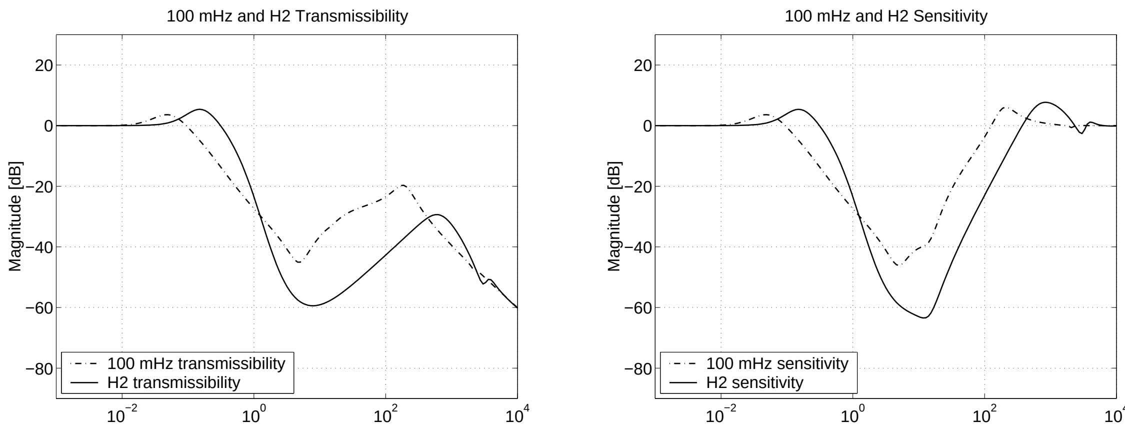

Figure 4.3 left*: Closed loop transmissibilities for the 100 mHz and the $\mathcal{H}_2$ controller case. The $\mathcal{H}_2$ controller tends to isolate the system more at the higher frequencies.* right*: Loop sensitivity functions $S(s)$ and $S_{\mathcal{H}_2}(s)$ when using the 100mHz and the $\mathcal{H}_2$ controller respectively. The loop sensitivity defines the amount of isolation. It is clearly visible in this graph, that the $\mathcal{H}_2$ controller tends to isolate more in the high frequency region.*

In Figure 4.3 the closed loop transmissibilities (see § 3.2.5) when using an $\mathcal{H}_2$ controller and a 100 mHz controller can be seen. Analyzing the transmissibilities, a clear difference in control strategy can be seen. The 100 mHz controller puts the first 0 dB cross-over at 0.1 Hz, as it was designed for. The $\mathcal{H}_2$ controller puts its first cross-over at about 0.3 Hz, decreasing the vibration isolation performance in this region, but apparently, it is better when taking the disturbances in account. This can also be concluded from the sensitivity functions in Figure 4.3; the $\mathcal{H}_2$ control strategy tends to shift the whole sensitivity function $S_{\mathcal{H}_2}(s)$ towards a higher frequency region. Since the sensitivity defines the increase in vibration isolation performance (see § 3.2.5), the isolation performance of the system is shifted to a higher frequency region.

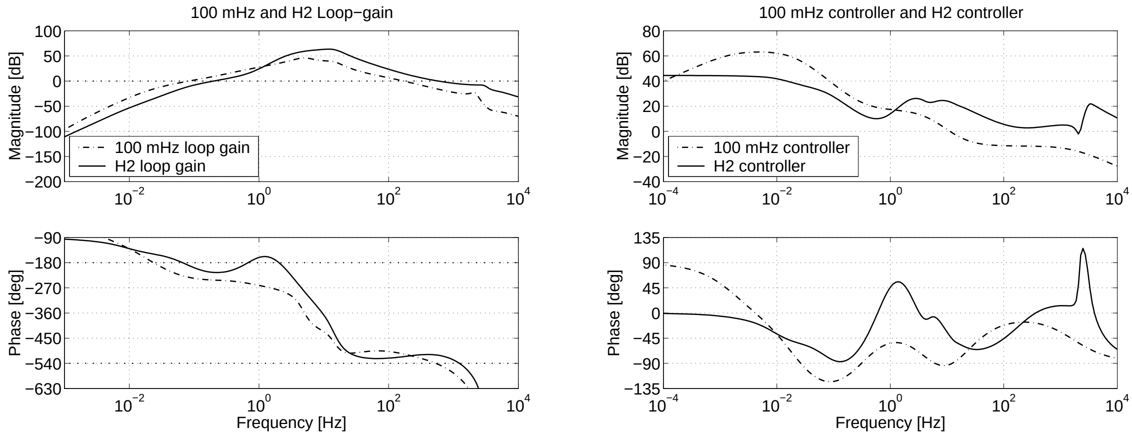

Figure 4.4 left: *Loop transfer functions $L(s)$ for the 100 mHz and $\mathcal{H}_2$ controller case. In the $\mathcal{H}_2$ case the 0 dB cross-overs lie at higher frequencies, suggesting a different control strategy.* right: *The 100 mHz controller together with the $\mathcal{H}_2$ controller. The $\mathcal{H}_2$ controller uses less gain in the low frequency region, and more gain in the high frequency region.*

From the loop gains in Figure 4.4 one can see that the $\mathcal{H}_2$ controller gives good phase and gain margins at both the cross-over frequencies, making it a robust and implementable controller. The $\mathcal{H}_2$ controller puts both the loop transfer function cross-over frequencies at a higher frequency than the 100 mHz controller, suggesting a different control strategy when one wants to optimize performance. Looking at the controllers in Figure 4.4, it can be seen that this difference in closed loop behavior is due to less gain at the low frequency region. At the higher frequencies, the $\mathcal{H}_2$ controller has more gain, achieving more isolation there.

4.2.4 The Pareto curve

As was discussed in the previous section, every ratio between the values of the scaling filters returns a different controller. Each controller uses a certain control effort level to achieve a certain performance level (given the disturbances filters). These levels can be plotted against each other, defining a Pareto curve. In Table 4.1 the different ratio's and obtained levels can be seen, which are plotted in Figure 4.5. One can see that there is a part on the curve where an increase of control effort stops causing a significant increase in performance (a decrease in the actual value). The sharp bend in the curve corresponds to an output filter ratio of 10^4. The $\mathcal{H}_2$ controller above was synthesized with ratio of 10^5, just to be sure the maximum achievable performance is squeezed out of the system.

Ratio W_2/W_1		effort u $[mV_{rms}]$		Performance $\dot{X}_l$ $[\mu m/sec]$
10^0	:	0.00469	-	98.6
10^1	:	0.349	-	83.2
$5{\cdot}10^1$	:	1.97	-	29
10^2	:	2.66	-	11.6
$5{\cdot}10^2$	:	3.18	-	1.25
10^3	:	3.24	-	0.91
10^4	:	3.65	-	0.696
10^5	:	5.73	-	0.667
10^6	:	12	-	0.666
10^7	:	16.7	-	0.666

Table 4.1 *Ratios and obtained levels defining the Pareto curve*

4.3 System performance using the $\mathcal{H}_2$ controller

4.3.1 Performance analysis using an $\mathcal{H}_2$ controller and a preamplifier

Now an $\mathcal{H}_2$ controller is synthesized with a ratio of 10^5, its performance can be analyzed as in the previous cases. The simulation results can be seen in Figure 4.6. Comparing these results with the fixed loop-gain case using a preamp (see Figure 3.18 on page 38), two things must be said. To objectively compare the two performance levels, the effort to achieve this should be the same. The control effort level in the that case was 31 mV_{rms} achieving a performance level of 2.9 $\mu m/s$. Comparing this control effort level with Table 4.1, the performance achieved using an $\mathcal{H}_2$ controller at that effort level would be near $0.666\mu m/sec$. So, with the use of an $\mathcal{H}_2$ controller the performance value decreases with a factor of 4.35! From the Pareto curve it can be observed that this effort level is a little bit overdone, and a lower level was chosen: 5.73 mV_{rms} resulting in a performance level of 0.667 $\mu m/sec$. The use of an $\mathcal{H}_2$ controller thus gives, even on this lower effort level, a serious performance improvement compared to the 100 mHz controller.

4.3.2 Experimental results using an $\mathcal{H}_2$ controller

An interesting question is if this controller strategy also works in practice. Is the performance improvement a pure theoretical result or does it also work when an $\mathcal{H}_2$ controller is really implemented? To validate the theoretical result an $\mathcal{H}_2$ controller was implemented on the dSpace 1104 board and the results were measured. Before the $\mathcal{H}_2$ controller could be implemented, the order was reduced from 25 to 15 and it was put in a discrete state

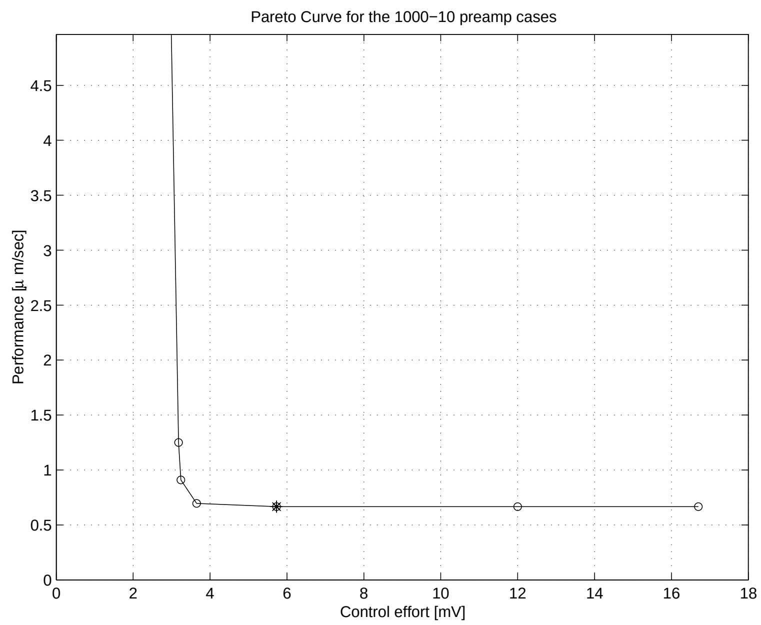

Figure 4.5 *Pareto curve of the 10-1000 preamp case. The curve shows how much effort is needed to achieve a certain performance level (More performance implies a lower performance value). The dots represent calculated points. When travelling the curve from left to right, the performance increases rapidly (value decreases) when the control effort increases. Somewhere near a performance value of 0.66 $\mu m/sec$ the curve levels off, implying that a large increase in control effort would only gives a small increase in performance. The curve bends at a ratio of approximately 10^4, as can be seen in the table. The $\mathcal{H}_2$ controller used above was computed with the ratio 10^5, which position on the curve is marked with an asterisk.*

space representation using MATLAB command `d2c`. The order reduction was done with the MATLAB command `modred`, deleting 10 weakly coupled states. After the model reduction, the gain and phase margins of the loop transfer function $L(s)$ with the reduced controller were carefully checked to make sure closed loop stability was not lost by the reduction step. To validate the performance of the $\mathcal{H}_2$ controller the controller input level (as in Section 3.6, the signal right after the ADC) is simulated and compared with the theoretical results. Next to the controller input level, the controller output level is also simulated and compared with the theoretical results. The controller output signal is defined as the signal value just before entering the DAC. These signals are conveniently available inside the computer, avoiding the introduction of new noise sources introduced by new measurements. The theoretical and experimental results can be seen in figures 4.7 and 4.8.

Analyzing the controller input results in Figure 4.7, one can see that the ground vibrations account for the majority of the (theoretical) control input power. The simulated level of 0.66 mV_{rms} matches almost perfectly with the measured level of 0.69 mV_{rms}. Since the ground vibration model overestimates the true ground vibration level, the simulated level is likely to

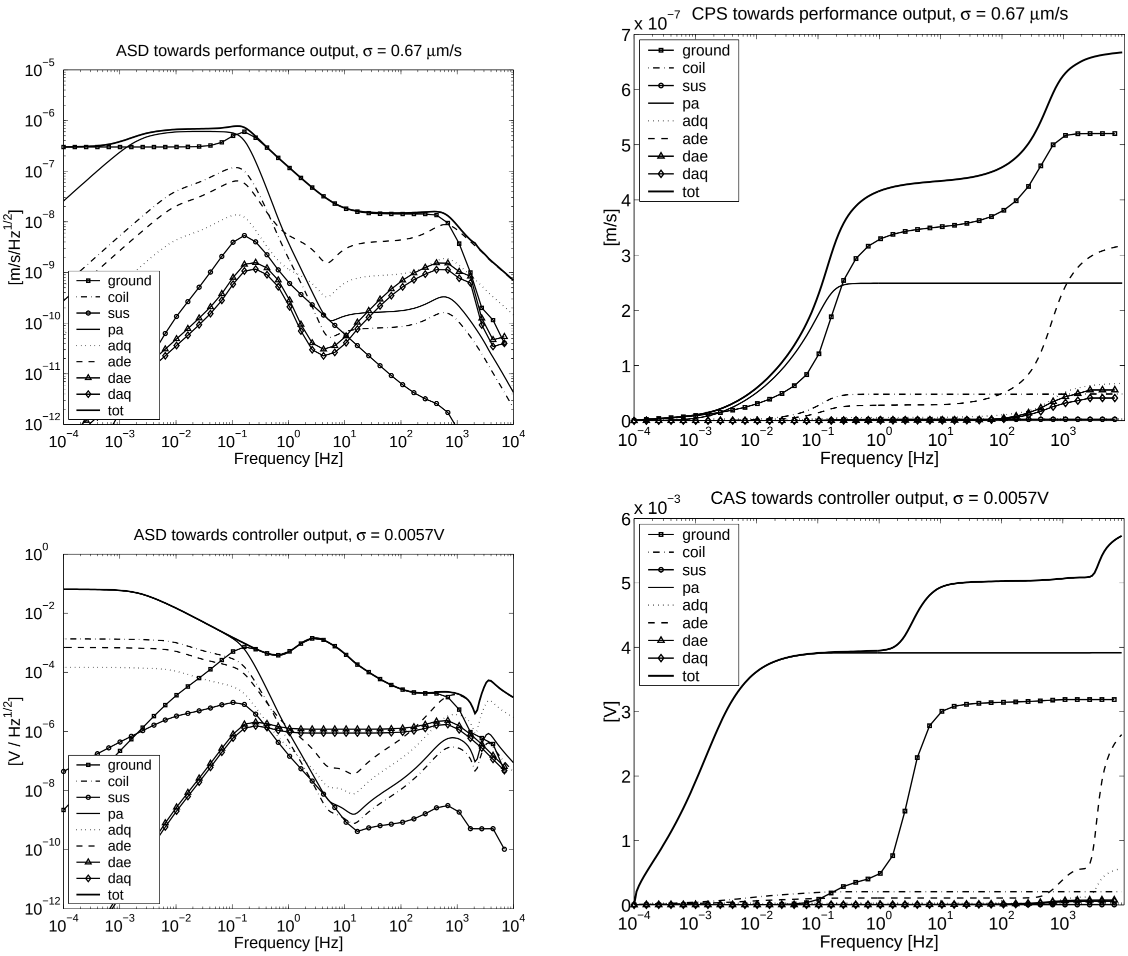

Figure 4.6 *Simulation of performance output spectra ($\dot{X}_l$) and the controller output spectra (u) using the 1000-10 preamplifier and an $\mathcal{H}_2$ controller.* above*: Simulated ASD (*left*) and CAS (*right*) of the performance signal $\dot{X}_l$ using an $\mathcal{H}_2$ controller and a preamplifier.* below*: Simulated ASD (*left*) and CAS (*right*) of the control signal u using an $\mathcal{H}_2$ controller and a preamplifier.*

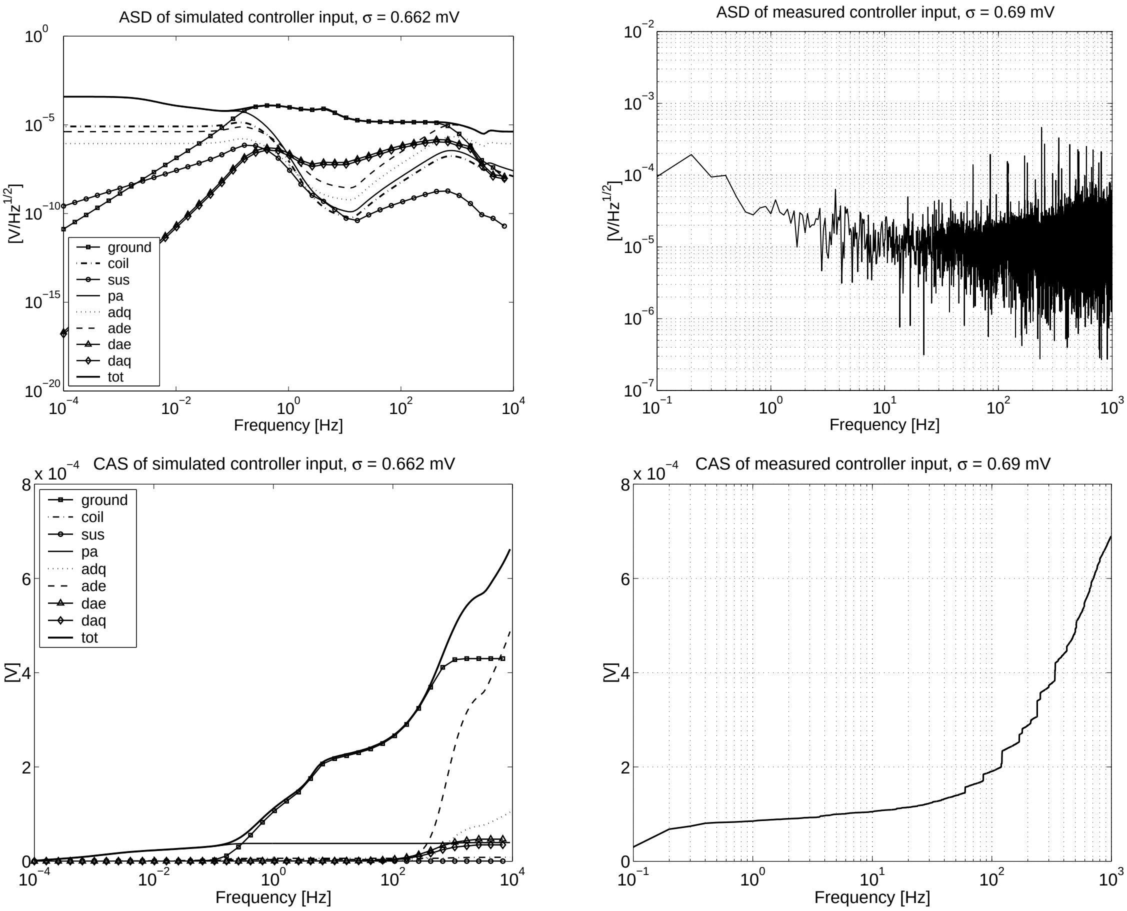

Figure 4.7 *Validation of the controller input y spectra using the 1000-10 preamplifier and an $\mathcal{H}_2$ controller.* above*: Simulated ASD (*left*) and measured ASD (*right*) of the controller input signal using an $\mathcal{H}_2$ controller and a preamplifier.*below*: Simulated CAS (*left*) and measured CAS (*right*) of the controller input signal using an $\mathcal{H}_2$ controller and a preamplifier.*

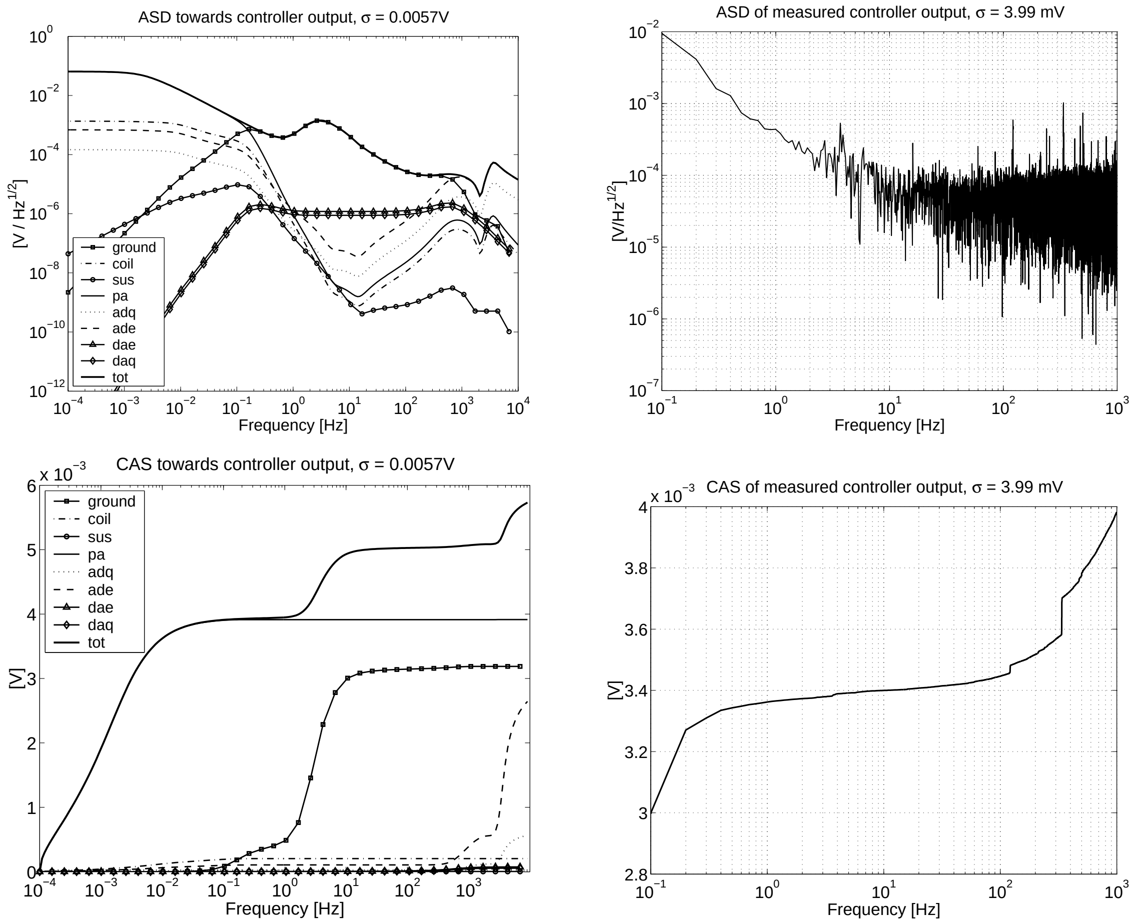

Figure 4.8 *Validation of the controller output u spectra using the 1000-10 preamplifier and an $\mathcal{H}_2$ controller.* above*: Simulated ASD (*left*) and measured ASD (*right*) of the controller output signal using an $\mathcal{H}_2$ controller and a preamplifier.*below*: Simulated CAS (*left*) and measured CAS (*right*) of the controller output signal using an $\mathcal{H}_2$ controller and a preamplifier.*

overestimate the measured level, therefore, the perfect match is more of a coincidence than due to prediction accuracy. The $\mathcal{H}_2$ controller achieves a lower controller input level than the 100 mHz controller. The measured controller input level decreased from 1.2 mV_{rms} to 0.67 mV_{rms}, an improvement of 50 %! On the right hand side of Figure 4.9 one can see the 10 sec time trace on which the measured ASD and CAS in Figure 4.7 is based.
Looking at Figure 4.8, one can see that the simulated controller output (which is the same as the control effort) of 5.7 mV_{rms} is still mainly due to the low frequency preamp noise, as can be seen in the simulated CAS. The measured controller output level also shows this low frequency power, but because the measured output was only measured over a period of 10 seconds, the lowest measured frequency is only 0.1 Hz. The low frequency noise of the preamp can therefore not be validated from this experiment. It is very apparent though when one looks at a controller output time trace as shown on the left hand side in Figure 4.9;

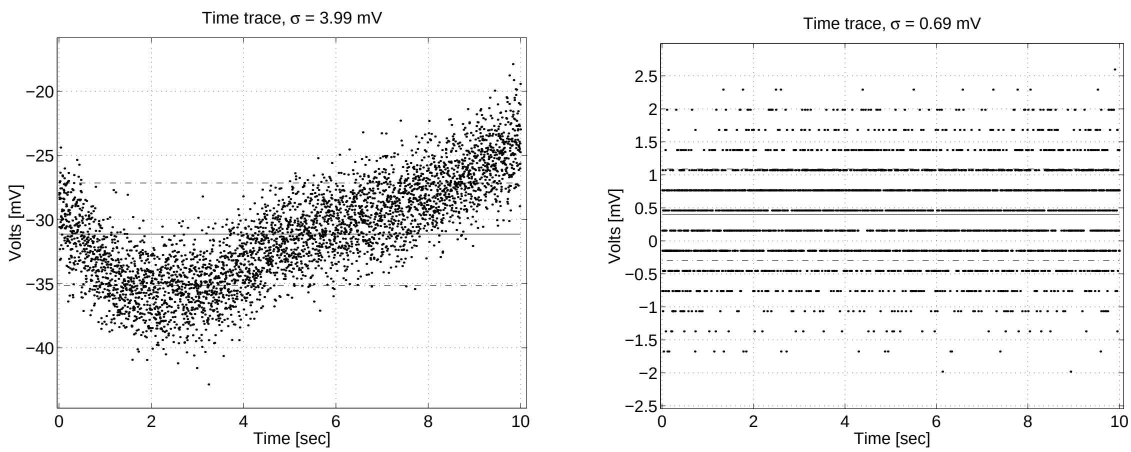

Figure 4.9 left*: Time trace of a controller output signal using an $\mathcal{H}_2$ controller and the 10-1000 preamp. The low frequency noise of the preamp is clearly visible as the controller output signal slowly moves up and down.* right*: Time trace of the controller input signal using an $\mathcal{H}_2$ controller and the 10-1000 preamp.*

the control signal is slowly drifting up and down.

4.4 Making a design decision using $\mathcal{H}_2$ control in DEB

4.4.1 The best preamplifier

With the DEB strategy in mind, one can ask what the best preamplifier transfer function is considering system performance? The preamplifier was introduced to improve the SNR of the geophone signal and its transfer function was designed with the geophone velocity sensitivity in mind, see § 3.5.2. But it is not guaranteed at all that the used preamplifier transfer function is the best transfer function to use when considering performance. In this paragraph the performance of a different preamplifier transfer function will be investigated using the DEB analysis approach. An $\mathcal{H}_2$ controller will be used to cancel the degree of freedom introduced by the controller, optimizing the system configuration for maximum performance.

To improve the SNR of the geophone signal the most simple strategy that comes in mind is to pre-amplify the signal as much as possible. There are two things that limit the preamplifier gain though; first, the preamplifier introduces noise. In general can be said, the more gain the preamplifier provides, the more noise it will introduce (see § 3.5.3). So, introducing gain comes with a price: an increase of noise in the circuit. Second, the gain of the preamplifier is limited by clipping of the A/D converter, which can only cope with signals in between $\pm 10\ V$. A practical limit in the open loop setting turned out to be a gain of 100 (the open loop setting is needed during start up of the system and is the worst case; it has the largest preamplifier output values, since the vibrations are not yet compensated for).

balancing of disturbances

A good design consideration to make is: how much preamplifier gain is actually needed? How high must the SNR be? Actually, the SNR must be considered frequency dependent; in one frequency region the SNR can be high enough, while in an other region the noise dominates the signal. The DEB performance analysis can give some clarity in this matter. One can say: the preamplifier has to amplify a certain frequency region just enough, such that on the one hand, the ADC noise are suppressed and on the other hand, the introduced preamplifier noise does not dominate the region. There is a balance that has to be found. In short, balancing of disturbances implies that the disturbance introduced by e.g., an extra gain and the disturbance itself (which the gain is supposed to suppress by improving the SNR) are balanced against each other such that they contribute an equal amount of power (over frequency) at the performance output.
Analyzing the performance CAS in Figure 4.6, one can see that the preamplifier noise now contributes a significant amount of power in the low frequency region up to 0.1 Hz. The A/D electrical noise then adds a significant part in the 1 kHz region. From this analysis the following questions arise: Does the preamplifier have to much gain in the low frequency region, introducing more preamplifier noise than necessary? Does the preamplifier have enough gain in the high frequency region, since the A/D electrical noise still pops up? In the following paragraph a different preamplifier will be analyzed in order to try to answer the questions above.

4.4.2 The constant gain preamplifier

To improve the performance as discussed above, less gain was needed in the low frequency region and more in the high frequency region. The old preamplifier transfer function (see Figure 3.15) then suggest that a constant gain preamplifier with the gain somewhere in between its low frequency gain of a 1000 and its high frequency gain of 10 would be a better choice. Therefore a preamp with a gain of 100 is chosen. Since the transfer function of the preamplifier is changed, its noise model is changed accordingly, as well and the weighting filter V_{w_1} used to synthesize the $\mathcal{H}_2$ controller.

Judging the preamp performance by its Pareto curve

Every different system configuration will obtain a certain performance level given a certain control effort level, defined by the Pareto curves. To compare the configurations, the two Pareto curves are computed and shown in Figure 4.10 on the left hand side.
Both the curves start at the open loop performance level of 98.8 $\mu m/sec$. As the control effort increases, the performance increases as well. Up to 3 mV_{rms} control effort the curves almost coincide, meaning that it does not really matter if the 1000-10 preamp is used or the 100 preamp. But, above 3 mV_{rms} control effort the 100 preamp curve drops below the 1000-10 preamp curve, meaning the the 100 preamp configuration can achieve a higher performance level than the 1000-10 preamp case. The absolute performance of the 1000-10 preamp case is 0.66 $\mu m/s$, compared to 0.55 $\mu m/s$ in the 100 preamp case, a 20 % improvement!

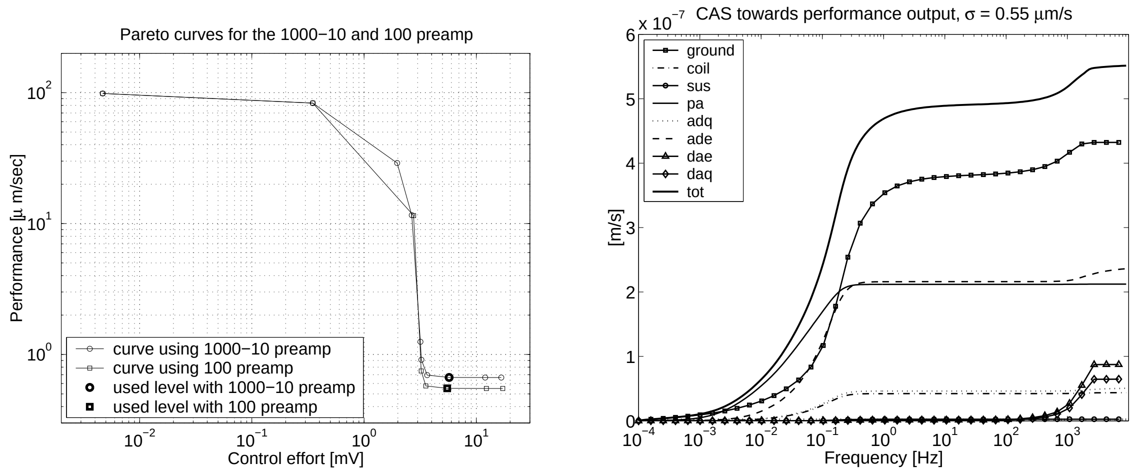

Figure 4.10 left*: Pareto curves using the 1000-10 preamp and the 100 preamp.* right*: Simulated CAS of the performance signal $\dot{X}_l$ using the 100 preamp and an $\mathcal{H}_2$ controller.*

On the right hand side Figure 4.10 the simulated CPS of the performance output can be seen. When analyzing the power contribution of the ADC electrical noise and the preamplifier noise one can see that their contributions are now well balanced (both contribute about the same amount of power at each frequency). So, designing the preamplifier by analyzing the noise levels of the preamplifier and the ADC and try to balance them, seems a good strategy to improve the system performance.

What can be concluded from these results is that the frequency dependent second order (lag shaped) preamplifier based on the geophone velocity sensitivity, does not result in a system which handles noise best. With the much simpler first order constant gain preamplifier a higher performance level can be achieved. There is one disadvantage to the constant gain preamplifier though, the constant gain 100 preamp makes the risk of clipping the A/D converter about 10 times higher. If the system clips when the loop is not yet closed, this can result in start-up problems. If clipping is not a problem e.g., when using a dual gain preamplifier, which can switch from low gain to high gain when the system is at its normal working point, then the constant gain 100 preamp is the preferred preamplifier. It is not only much easier to build (only one stage using one opamp and two resistors) but it can also achieve a higher performance level than the 1000-10 preamp.

4.5 Conclusions

The $\mathcal{H}_2$ control strategy is successfully applied to the vibration isolation system. An $\mathcal{H}_2$ controller is synthesized and the (theoretical) performance of the system is maximized, showing the system designer the performance potential of the system concept. The simulated results show a significant increase in performance when using an $\mathcal{H}_2$ controller compared to the (standard) controller used in the previous chapter. The performance level dropped from 2.9 $\mu m/s$, when using a preamplifier and standard controller, to 0.66 $\mu m/s$ using the same preamplifier and an $\mathcal{H}_2$ controller.

The performance level achieved by the $\mathcal{H}_2$ controller is validated with experiments, showing that the theoretical increase in performance displays a realistic image. The synthesized $\mathcal{H}_2$ controller is therefore a good indicator for the control designer how to control the system in practice to optimize the system performance. The 0.1 Hz bandwidth used in the previous chapter turned out not to be such a good control strategy, since it needed in a very high low frequency controller gain, resulting in a high level of low frequency noise at the performance output. The $\mathcal{H}_2$ controller suggested a 0.3 Hz bandwidth, resulting in significantly less low frequency noise at the performance outputs.

The use of Pareto curves to judge different system also turned out to be feasible in practice. Two different preamplifier designs were compared and their performance analyzed. Their Pareto curves showed that the much simpler constant gain 100 preamp can achieve a higher performance level than the second order 1000-10 preamp designed in the previous chapter. This design exercise shows that the use of $\mathcal{H}_2$ control in the DEB design approach can be of great value for the designer.

Chapter 5

Case study, Advanced Isolation ModuleS

5.1 Introduction

The research presented in this chapter is done during a 3 months stay at Philips Center for Industrial Technology (Philips CFT) in Eindhoven, the Netherlands. At Philips CFT a new vibration isolation system is being developed which carries the name 'Advance Isolation ModuleS' (AIMS). The main challenge of this case study is to apply the DEB design approach in the way it was developed for; to predict the performance of a vibration isolation system which is still on the drawing board, check if the desired performance specification is met and point out critical performance limiting components.

The AIMS system is designed to be used parallel with another passive isolator system. In Figure 5.1 this configuration is illustrated. The performance of the passive isolator, here characterized by its main resonance frequency of 2 Hz, is improved by the parallel introduction of the AIMS. A crucial question to the system designer now is: is the total isolating performance indeed improved by the introduction of the AIMS? Another interesting question is: Is the performance of the AIMS parallel with the passive isolator, comparable with the performance of the better and more expensive 0.5 Hz passive isolator? Since it is a design aim that the AIMS and 2 Hz isolator together is less expensive than the 0.5 Hz isolator, this would imply a reduction in costs of the total isolation system.

The goals of this chapter can be formulated as follows: Show that the DEB approach can be applied during the design phase of the AIMS system. By doing this, find out if the AIMS concept is feasible and point out the performance limiting components. Investigate the influence of different control strategies to the final performance of the system. Compare the performance of the AIMS (parallel with the 2 Hz passive isolator) with the performance of a 0.5 Hz passive isolator.

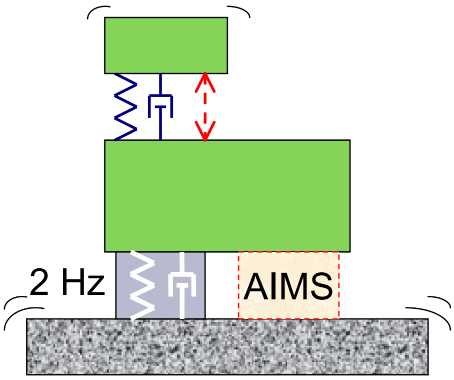

Figure 5.1 *The AIMS vibration isolator is designed to be used parallel with a passive isolator.*

5.2 Advanced vibration isolation

The AIMS works with a different isolation concept than the isolator in the previous case study. This new concept is referred to as *Advanced Vibration Isolation* (AVI) and is explained in this section. The AVI concept is based on a 'payload system' mimicking an other, 'ideal system'. The payload system and the ideal system are both subject to the same input vibrations, and since the payload system 'follows' the response of the ideal system, the payload system now also has ideal system behavior. The output of the ideal system actually acts as a reference for the payload system.

An ideal vibration isolation system, is softly suspended to the ground and very strongly attached to a virtual point in the sky, a configuration referred to as a 'sky hook configuration'. This way the ground vibrations do almost not propagate into the system and payload disturbance forces almost have no effect on the payload since the system is hooked to the sky. In the AVI concept this behavior is approached as follows. The ideal system consists of a reference mass which is suspended in a control loop at 0.5 Hz, which we will call the reference loop. The main system follows the position of the reference mass via another control loop, the payload loop. The payload reacts on vibrations as an (almost ideal) 0.5 Hz suspended system. Payload disturbance forces F_d act on the payload part of the AVI system and not on the reference mass and thus do not cause any disturbance forces on the reference mass. Because the payload follows the reference mass, the payload loop will suppress displacements due to payload disturbance forces, achieving the sky hook effect. A model of the system configuration can be seen in Figure 5.2.
Besides the AIMS, the payload mass is also suspended with a simple vibration isolation system, which is modelled with a spring k_p. This simple isolator can be seen as a basic passive isolation system and the AIMS as an add-on system, to further improve the isolation performance.

The relative position $x_s - x_h$ between the reference mass and the ground is measured with a capacitive position sensor, and fed back via a reference controller into a Lorentz actuator,

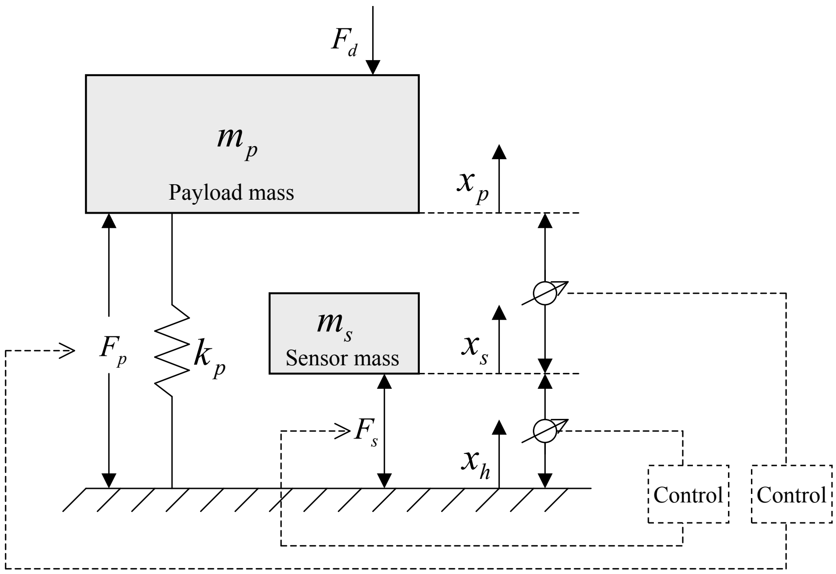

Figure 5.2 *AVI model*

which generates a force F_s. The closed loop would typically achieve a 0.5 Hz suspension behavior.

The relative position $x_p - x_s$ between the reference mass and payload mass is also measured with a capacitive position sensor, which is fed back via a payload controller into a second lorentz actuator which generates a force F_p between the ground and the payload mass. The force F_p is the actual compensating force which actively isolates the payload mass from vibrations.

5.2.1 Performance specification

The AIMS is designed to isolate high performance machinery from vibrations. A typical maximum acceleration level for this kind of machinery has a 1-σ value of 1 mm/s^2. In order to achieve this acceleration level it is believed that the isolator may only contribute about 10% of that value (Vervoordeldonk [26]). So in this case, the noise level of the AIMS (excluded the contribution by ground vibrations) may not be larger than 0.1 mm/s^2. This performance value will be the aim of this case study. The frequency distribution of the noise is also of importance. In general the power of the noise should be located well below the first internal resonance frequency of the payload.

5.3 Transfer function of the AIMS

The AIMS system contains two separate control loops, the reference loop and the payload loop, as can be seen in the block diagram in Figure 5.3.

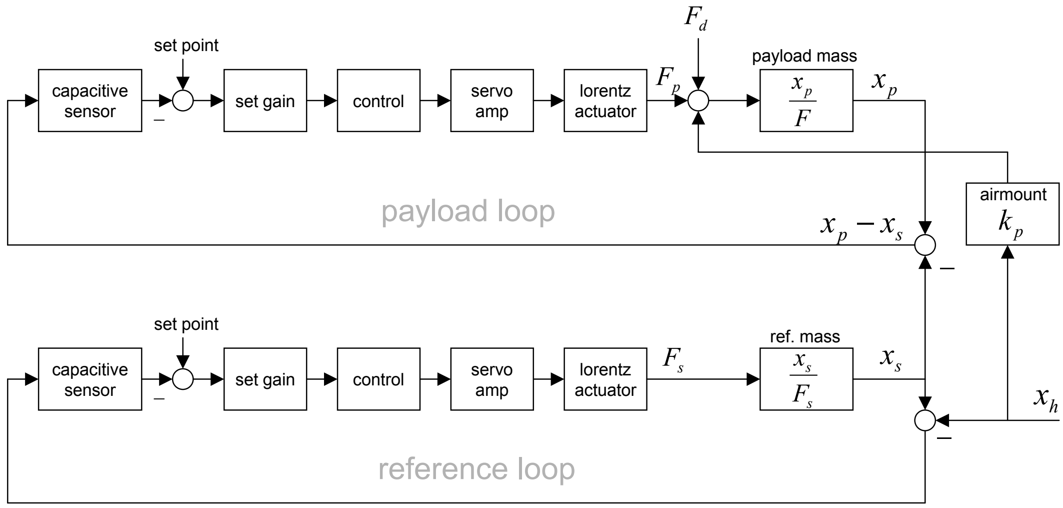

Figure 5.3 *AVI control configuration*

The reference loop is totally independent from the payload loop. It acts as a reference generator for the payload loop, giving the payload loop a position reference: x_s. This reference acts as a disturbance on the payload loop. The better the payload loop can suppress this disturbance, the more the payload will mimic the 0.5 Hz behavior of the reference mass, achieving vibration isolation within the bandwidth of the payload loop.

The ground vibrations x_h enter the system at two different locations; as a position disturbance in the reference loop and, via the basic isolation system, as a disturbance force in the payload loop. Payload disturbance forces F_d enter the system in the payload loop and can not influence the reference loop, giving the system the 'sky hook' effect within the payload loop bandwidth.

5.3.1 Reference loop transfer function

In this section all the components of the reference loop will be discussed briefly and the loop transfer function will be determined.
The first component in the reference loop is the capacitive reference sensor, which converts a position into a voltage signal using a capacitive measuring technique. It has a sensitivity of 3300 V/m and contains an internal second order low pass filter with cut-off frequencies at 100 and 160 Hz (transfer function not shown):

$$P_{sen,r}(s) = 3300 \left(\frac{2\pi 100}{s + 2\pi 100}\right)\left(\frac{2\pi 160}{s + 2\pi 160}\right) \quad [\text{V/m}] \tag{5.1}$$

The set-point, where the height between the ground and the reference mass can be set, has a gain on its own. This can be modelled as a addition point as shown in Figure 5.3 in series with a static gain $P_{set,r}$. The gain of the reference set-point is 0.2. The set-point is discussed in more detail in Section 5.4.2 on page 72. Looking at Figure 5.11 on page 73, the (static) transfer function can written as $-R_{spf}/R_{spi}$.

$$P_{set,r} = 0.2 \quad [\mathrm{V/V}] \tag{5.2}$$

The reference controller is designed to achieve a closed loop 0.5 Hz suspension behavior of the reference mass. To achieve this a PID controller is used with a transfer function which can be seen in Figure 5.4. The transfer function of the PID controller is discussed in more detail in Section 5.4.2 on page 72.

$$P_{pid,r}(s) = 0.051 \left(\frac{s+0.45}{s+0.041}\right)\left(\frac{1.06s+1}{0.21s+1}\right) \quad [\mathrm{V/V}] \tag{5.3}$$

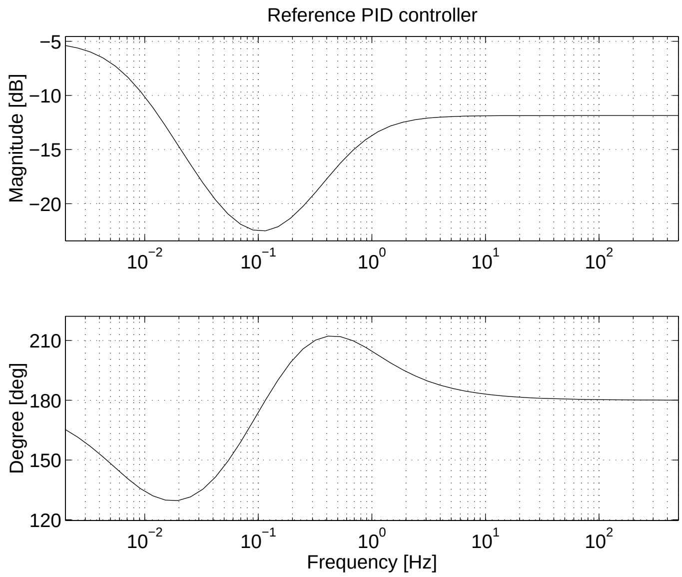

Figure 5.4 *Reference PID controller*

The controller voltage signal is transformed into a current signal using a servo amplifier. The reference servo amplifier is referred to as the 'umi' and has a static gain of 0.0096 and an internal first order low pass filter with a cut-off frequency of 2 kHz (transfer not shown).

$$P_{umi}(s) = 0.0096 \left(\frac{2\pi 2000}{s+2\pi 2000}\right) \quad [\mathrm{A/V}] \tag{5.4}$$

The Lorentz actuator converts the current signal into the force F_s. The gain of the actuator is static and has the value 1.2 N/A.

$$P_{lor,r} = 1.2 \quad [\mathrm{N/A}] \tag{5.5}$$

Finally, the open loop model of the reference mass dynamics is given by

$$\frac{x_s}{F_s} = \frac{1}{m_s s^2 + b_s s} \tag{5.6}$$

where $m_s = 0.12\ kg$ is the mass of the reference sensor, and $b_s = 0.01\ Ns/m$ models the parasitic damping of the air bearing of the reference mass.

The series connection of all these components returns the loop gain function $L_r(s)$.

$$L_r(s) = P_{sen,r}(s)\ P_{set,r}\ P_{pid,r}(s)\ P_{umi}(s)\ P_{lor,r}\ \frac{x_s}{F_s} \quad [m/m] \tag{5.7}$$

A Bode diagram of the reference loop gain function $L_r(s)$, together with its complementary sensitivity function $L_r(s)(L_r(s)+1)^{-1}$, can be seen in Figure 5.5. From the complementary sensitivity one can conclude that the closed loop reference system indeed has as a 0.5 Hz suspension behavior.

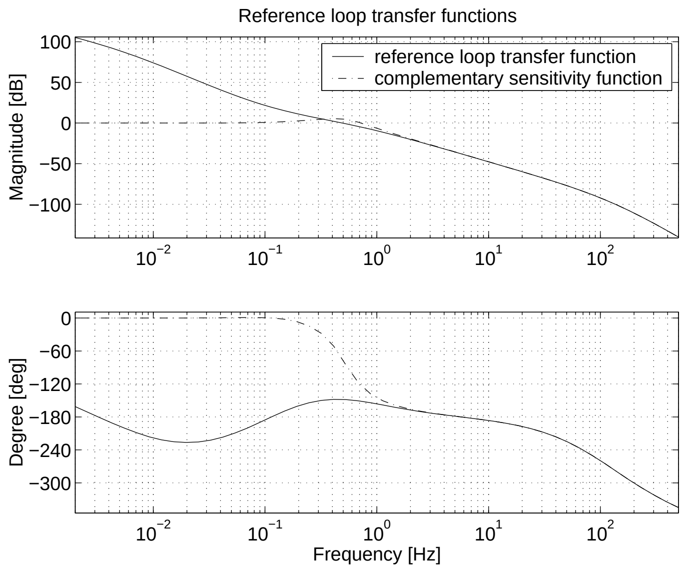

Figure 5.5 *Reference loop gain function $L_r(s)$, together with the complementary sensitivity function. From the latter one can conclude that the closed loop reference system has as a 0.5 Hz suspension behavior.*

5.3.2 Payload loop transfer function

In this section all the components of the payload loop will be discussed briefly and the loop transfer function will be determined.
The capacitive payload sensor has a sensitivity of 9000 V/m and an internal second order low pass filter with cut-off frequencies at 1 kHz and 2 kHz (transfer function not shown).

$$P_{sen,p}(s) = 9000 \left(\frac{2\pi 1000}{s + 2\pi 1000}\right)\left(\frac{2\pi 2000}{s + 2\pi 2000}\right) \quad [\mathrm{V/m}] \tag{5.8}$$

The gain of the payload set-point is 10.

$$P_{set,p} = 10 \quad [\text{V/V}] \tag{5.9}$$

The payload controller is designed such that the closed payload loop can suppress reference disturbances up to 30 Hz. To achieve this, a PID controller $P_{pid,p}(s)$ is used, of which the transfer function can be seen in Figure 5.6.

$$P_{pid,p}(s) = 0.58 \left(\frac{s+27}{s+2.4}\right)\left(\frac{0.013s+1}{0.0027s+1}\right) \quad [\text{V/V}] \tag{5.10}$$

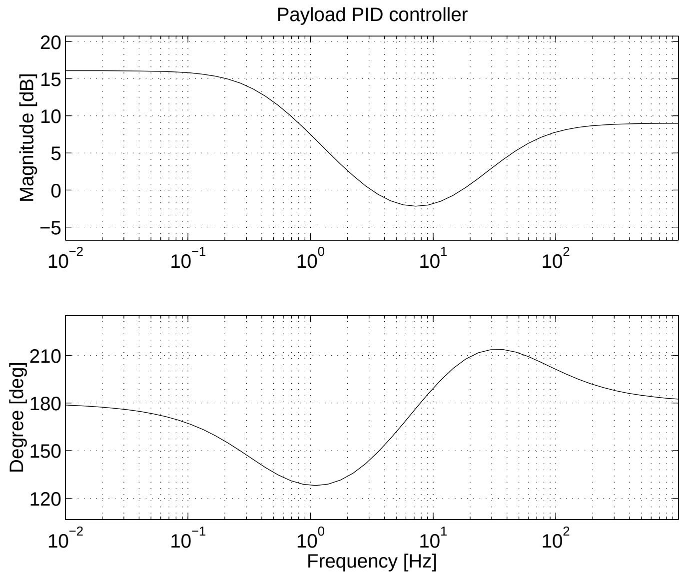

Figure 5.6 *Payload PID controller*

The payload servo amplifier, referred to as 'uma', has a gain of 15 and also an internal first order low pass filter with a cut-off frequency of 2 kHz (transfer not shown).

$$P_{uma}(s) = 15\left(\frac{2\pi 2000}{s+2\pi 2000}\right) \quad [\text{A/V}] \tag{5.11}$$

The gain of the payload Lorentz actuator is 9.5 N/A.

$$P_{lor,p} = 9.5 \quad [\text{N/A}] \tag{5.12}$$

The open loop model of the payload mass x_p/F also contains the basic isolator dynamics and is given by

$$\frac{x_p}{F} = \frac{1/m_p}{s^2 + 2\zeta_p\omega_n s + \omega_n^2} \tag{5.13}$$

where $m_p = 500\ kg$ is the mass of the payload, $\zeta_p = 0.05$ and $\omega_n = 2\pi(2Hz)\ rad/sec$ (The damping of the airmount is not shown in Figure 5.2).

The series connection of all these components returns the payload loop gain function $L_p(s)$.

$$L_p(s) = P_{sen,p}(s)\ P_{set,p}\ P_{pid,p}(s)\ P_{uma}(s)\ P_{lor,p}\ \frac{x_p}{F} \quad [m/m] \tag{5.14}$$

The loop gain function $L_p(s)$ can be seen in Figure 5.7, together with the sensitivity function $(L_p(s)+1)^{-1}$ of the payload loop. From the sensitivity function one can conclude that the closed loop payload system can suppress reference disturbances up to 30 Hz, enabling the AIMS to improve the isolation performance compared to the basic isolation system up to this frequency.

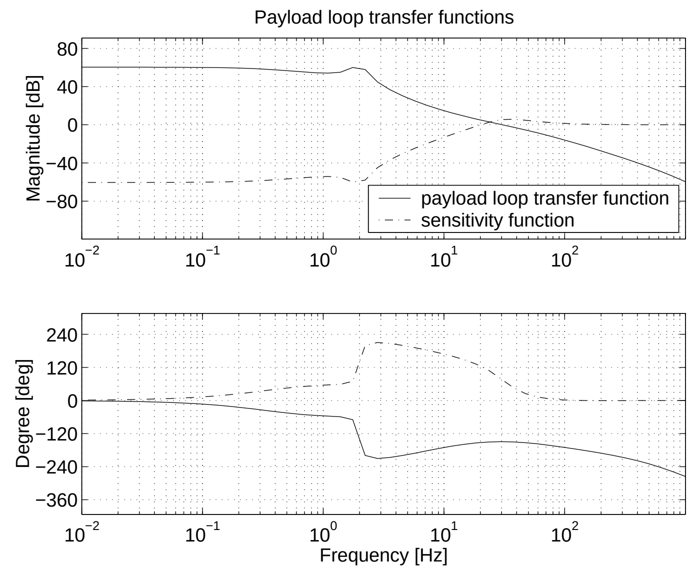

Figure 5.7 *Payload loop gain function $L_p(s)$ together with its sensitivity function. From the sensitivity function one can see that payload loop reference disturbances are suppressed up to 30 Hz.*

5.3.3 Open and closed loop transfer function of total system

The payload has to be isolated from vibrations. An important measure of performance is the acceleration of the payload $\ddot{x_p}$, since below the first resonance frequency of the payload (e.g., 100 Hz) accelerations of the payload are proportional with physical deformations within the payload, causing measurements errors etc. When the ground vibrations are described by an acceleration spectrum $[\ddot{x_h}^2/Hz]$, the transfer function to analyze is $\ddot{x_p}/\ddot{x_h}$, which is equal to the transfer function x_p/x_h. One can see that this transfer function is given by:

$$\frac{x_p}{x_h} = T_r T_p + k_p[x_p/F]S_p \tag{5.15}$$

where T_r and T_p are the complementary sensitivity function of the reference loop and payload loop respectively, and S_p is the sensitivity function of the payload loop. This closed loop transfer function is called the *transmissibility*, and defines the performance of the AIMS in terms of vibration isolation. The open loop transfer function is also given for comparison:

$$\text{open loop} = k_p[x_p/F] \tag{5.16}$$

Both these transfer functions are plotted in Figure 5.8. Comparing the two transfer functions, one can see that the closed loop AIMS improves the vibration isolation performance in the 0.8 Hz - 20 Hz region.

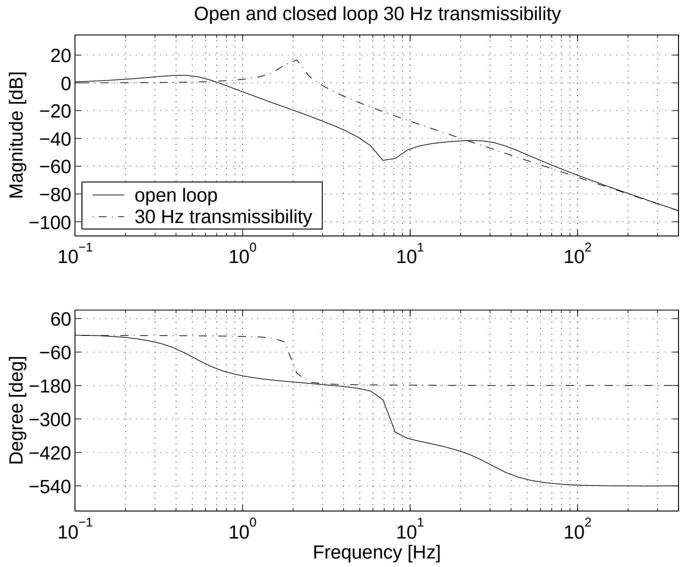

Figure 5.8 *The open and closed loop transfer function (30 Hz transmissibility) of the AIMS.*

5.4 Modelling of disturbances and noise sources

In this section the disturbance and noise sources acting on the AIMS are discussed. Several physical disturbances act on the AIMS, like ground vibrations, payload disturbance forces, and air pressure variations. Next to that, there are several electrical noise sources originating from the electrical circuitry, e.g., the capacitive sensor and controller electronics.

Figure 5.9 presents the identified noise sources in a schematic. Transfer functions are denoted with a P, and the power spectral densities [SI^2/Hz], used to model the disturbance sources, are denoted with a S. In total, 11 noise sources are identified, giving the closed loop system 11 inputs, $w_1 ... w_{11}$. In the following sections the disturbance sources will be modelled.
The transfer functions $P_{..}$ are analogue to Figure 5.3 on page 64, except that the transfer function $P_{sys,p}$ now has two outputs: x_p and $\ddot{x}_p$, the position and acceleration of the payload

respectively. The payload acceleration is defined as the performance output of the closed loop system.

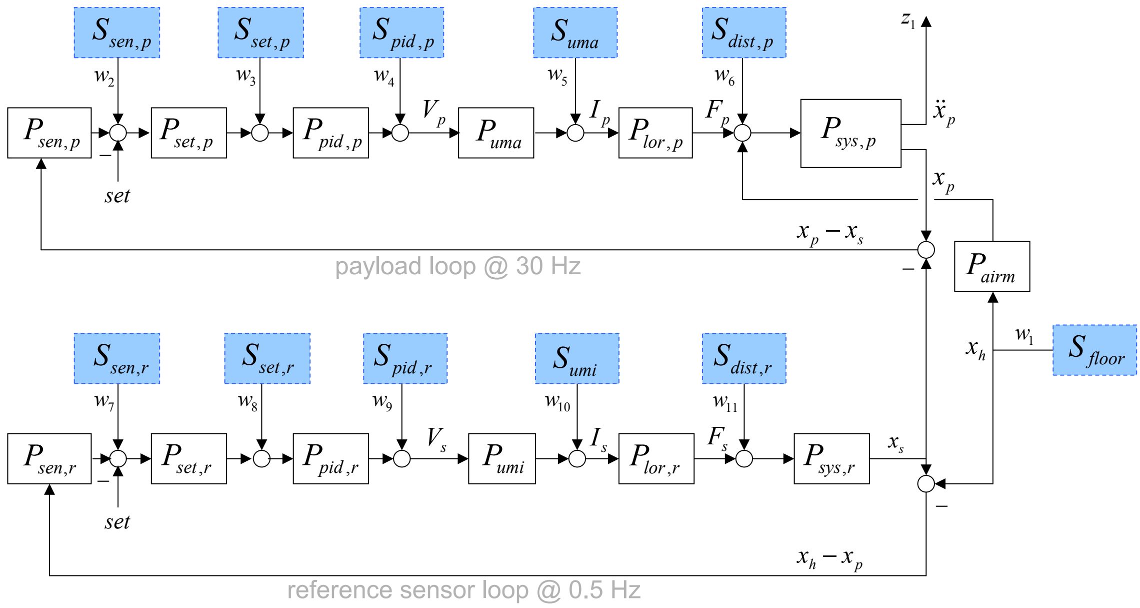

Figure 5.9 *Closed loop AIMS with disturbance and noise sources modelled with Power Spectral Densities $S_{..}$. The acceleration of the payload is defined as the performance output.*

5.4.1 Ground vibrations

The most important disturbance source in this vibration isolation case study are the ground vibrations. To model the ground vibrations a filter is used which is based on the ground vibration measurements shown in Figure 3.10 on page 29. The filter is developed in a similar manner as the filter (3.7), but now it is expressed in terms of acceleration. The filter is given by:

$$V(j\omega)_{floor} = 10^{-6}\left(\frac{\frac{3}{2\pi}j\omega+1}{\frac{3}{2\pi 10}j\omega+1}\right)^3\left(\frac{\frac{5}{2\pi}j\omega}{\frac{5}{2\pi}j\omega+1}\right)^3 \qquad [(m/s^2)/\sqrt{Hz}] \tag{5.17}$$

The 3^{rd} order high pass filter (last factor on the right hand side) was added because one does not want the filter to define a DC *position* disturbance on the AIMS (this would imply that the ground itself is off-set with some constant value, which is unrealistic). The relation with the PSD S_{floor} shown in Figure 5.9 is as follows:

$$S_{floor}(\omega) = V_{floor}(j\omega)V^*_{floor}(j\omega) \tag{5.18}$$

where $V^*(j\omega)$ denotes the complex conjugate transpose of $V(j\omega)$.

As stated earlier, the ground vibrations enter the system at two different locations, via the airmount and as a position disturbance in the reference loop.

5.4.2 Electrical noise sources

The payload loop and reference loop both consist of the same electrical components: a capacitive sensor, a set-point, a PID controller and a servo amplifier. Each of these components introduces an amount of noise. The noise models will be described below.

Capacitive sensor noise

At the time of this research, the two capacitive sensors are still in development. Therefore the modelled noise level here can deviate from the final noise model and the model must thus be seen as a preliminary model. The noise of the capacitive payload sensor was measured using an HP Dynamic Signal Analyzer. The measured power spectral density can be seen in Figure 5.10. The PSD of the sensor noise can be modelled with a fourth order model with corner frequencies at 70 Hz and 700 Hz and an asymptotic high frequency level of $(10n^2)$ V_{rms}^2/Hz. The sensor noise model is modelled such that its power matches the measured power level over the 4Hz - 800Hz frequency grid. This can be seen in the right part of Figure 5.10. The payload sensor has an internal low pass filter as was discussed in the previous section. The noise model must therefore be multiplied with the square of the low pass filter transfer function to make sure the high frequency energy content of the model corresponds with reality. The model is denoted by $S_{sen,p}(\omega)$, where the subscript refers to payload sensor, and can be written as:

$$S_{sen,p}(\omega) = (10n)^2 \left(\frac{j\omega + 2\pi700}{j\omega + 2\pi70}\right)^4 \left(\frac{2\pi1000}{j\omega + 2\pi1000}\,\frac{2\pi2000}{j\omega + 2\pi2000}\right)^2 \quad [V^2/Hz] \tag{5.19}$$

This model can also be seen in Figure 5.10.
The same model is used for the reference sensor, which is equal to the payload sensor (it was not measured separately), except that its low pass filter is different. To be safe, its asymptotic noise level is taken 1.5 times higher. The noise PSD model used for the reference sensor is denoted by $S_{sen,r}(\omega)$:

$$S_{sen,r}(\omega) = (15n)^2 \left(\frac{j\omega + 2\pi700}{j\omega + 2\pi70}\right)^4 \left(\frac{2\pi100}{j\omega + 2\pi100}\,\frac{2\pi160}{j\omega + 2\pi160}\right)^2 \quad [V^2/Hz] \tag{5.20}$$

The surface of the sensor noise PSD is equal to the variance, or squared standard deviation, of the noise signal. The standard deviation found for the payload sensor equals 7.3 μV_{rms} (over a frequency grid from 4Hz to 800Hz). When the sensor noise PSD is converted to the input of the sensor, an equivalent position noise level can be computed, giving a value of 0.81 nm on the same frequency grid.

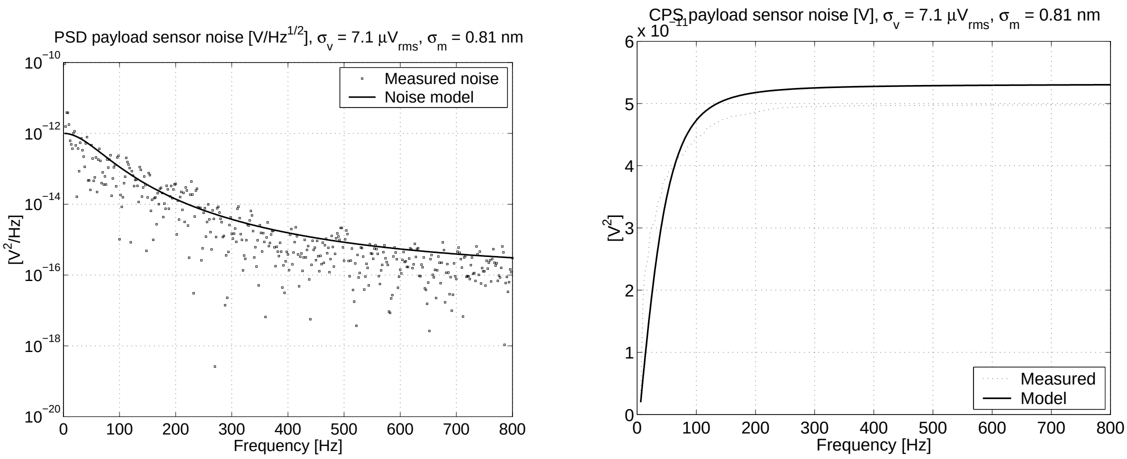

Figure 5.10 left: *PSD of the payload sensor noise in the 4-800 Hz range. The noise model* $S_{sen,p}(\omega)$ *is also plotted* right: *The CPS of the measured sensor noise in the 4-800Hz range and the CPS of the noise model. The noise model is modelled such that the measured power matches the modelled power.*

Set-point noise

The set-points electrical circuits comprises an operational amplifier, the op27, and four resistors, as can be seen in Figure 5.11. The resistors generate thermal noise and the opamp generates voltage noise and current noise. set-points. The thermal noise generated by the resistors was accounted for in this analysis as described by Rodgers [18], but is not worked out here. Since the contribution to the performance output by the set-point noise sources will turn out to be of minor importance (see § 5.5.2), not all noise sources are modelled here, only the contribution by the opamp noise is discussed.

The voltage and current noise model of the op27 opamp have already been discussed in Section B.4.2, but are repeated here for convenience:

$$S_{e_n}(\omega) = e_o^2 \left(1 + \frac{2\pi f_v}{\omega}\right) \quad [V_{rms}^2/Hz] \tag{5.21}$$

$$S_{i_n\pm}(\omega) = i_o^2 \left(1 + \frac{2\pi f_c}{\omega}\right) \quad [A_{rms}^2/Hz] \tag{5.22}$$

with parameter values as listed in Table 5.1.

The propagation of the noise towards the output is very similar to the preamp case covered in Section B.4.3 and is based on Rodgers [18].

Asymptotic high frequency voltage level e_o	:	$3.0 \cdot 10^{-9}\ V_{rms}$
Asymptotic high frequency current level i_o	:	$0.4 \cdot 10^{-12}\ A_{rms}$
Voltage noise corner frequency f_v	:	$2.7\ Hz$
Current noise corner frequency f_c	:	$140\ Hz$

Table 5.1 *Specifications of the op27*

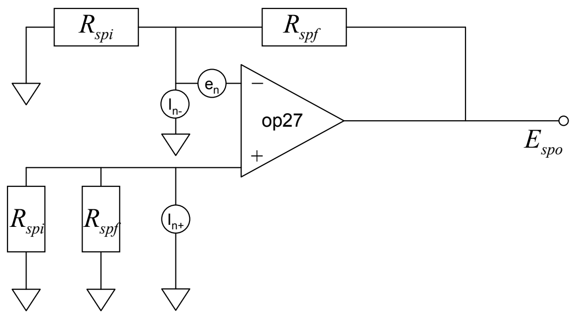

Figure 5.11 *Set-point circuit configuration with a voltage noise model e_n and two current noise models i_{n-} and i_{n+}.*

Voltage noise

The noise at the set-point output due to e_n is denoted by S_{spo,e_n} (read subscript as: set-point output due to e_n). From the voltage divider relationship between e_n and E_{spo}, S_{spo,e_n} can be obtained as:

$$S_{spo,e_n}(\omega) = \left(1 + \frac{R_{spf}}{R_{spi}}\right)^2 S_{e_n}(\omega) \tag{5.23}$$

Current noise

The noise at the set-point output due to i_n is denoted by S_{spo,i_n}. The currents coming from i_{n+} can not flow through the resistors R_{spi} and R_{spf} (below), since they are grounded at the bottom. Their top side is at virtual ground, so there will be no potential difference across the two resistors due to i_{n+}.

The currents from i_{n-} will not flow through R_{spi} (above), because the left side is at ground and the right side is at virtual ground, so there is no potential difference across R_{spi} due to i_{n-}. Therefore, all of i_{n-} flows through R_{spf}, and none of it flows through R_{spi}.
So for the current noise at the set-point output due to i_{n-} we can write :

$$S_{spo,i_{n-}}(\omega) = R_{spf}^2\ S_{i_n}(\omega) \tag{5.24}$$

Adding up both obtained PSD's gives the total PSD of the set-point noise at the set-point output S_{spo}:

$$S_{spo}(\omega) = \left(1 + \frac{R_{spf}}{R_{spi}}\right)^2 S_{e_n}(\omega) + R_{spf}^2 \; S_{i_n}(\omega) \tag{5.25}$$

The set-point noise PSD at the set-point output in the payload loop will be denoted by $S_{set,p}$ and the PSD in the reference loop by $S_{set,r}$. The resistor values for R_{spi} and R_{spf} for the payload loop are $5k\Omega$ and $50k\Omega$ resp. and for the reference loop $10k\Omega$ and $2k\Omega$ resp.

Analogue PID controller noise

A schematic of an analogue PID controller can be seen in Figure 5.12. The transfer function from E_{pidi} to E_{pido} is given by $-Z_f(s)/Z_i(s)$, which defines the transfer function of the PID controller. The transfer functions of $Z_f(s)$ and $Z_i(s)$ are given by:

$$Z_f(s) = R_{f1}\left(\frac{\tau_2 s + 1}{\tau_1 s + 1}\right) \tag{5.26}$$

$$Z_i(s) = \frac{1}{R_{i1}}\left(\frac{\tau_3 s + 1}{\tau_4 s + 1}\right) \tag{5.27}$$

where the time constants can be written in resistor and capacitor values as follows

$$\begin{aligned} \tau_1 &= C_f(R_{f1} + R_{f2}) && (5.28)\\ \tau_2 &= C_f(R_{f2}) && (5.29)\\ \tau_3 &= C_i(R_{i1} + R_{i2}) && (5.30)\\ \tau_4 &= C_i(R_{i2}) && (5.31) \end{aligned}$$

making the total PID transfer function:

$$P_{pid}(s) = -\frac{R_{f1}}{R_{i1}}\left(\frac{R_{f2}C_f s + 1}{(R_{f1} + R_{f2})C_f s + 1}\right)\left(\frac{(R_{i1} + R_{i2})C_i s + 1}{R_{i2}C_i s + 1}\right) \tag{5.32}$$

which can be written in classical PID form:

$$P_{pid}(s) = -\underbrace{\frac{R_{f1}||R_{f1}}{R_{i1}}}_{P}\underbrace{\left(\frac{s + \frac{1}{R_{f2}C_f}}{s + \frac{1}{(R_{f1}+R_{f2})C_f}}\right)}_{I}\underbrace{\left(\frac{(R_{i1} + R_{i2})C_i s + 1}{R_{i2}C_i s + 1}\right)}_{D} \tag{5.33}$$

The resistor and capacitor values for the payload and reference controller are listed in Table 5.2.

Thermal noise

The thermal noise generated by the resistors was accounted for in this analysis as described by Rodgers [18], but is not worked out here. Since the contribution to the performance output by the controller noise sources will turn out to be of minor importance (see Section 5.5.2) only the contribution by the opamp noise is covered.

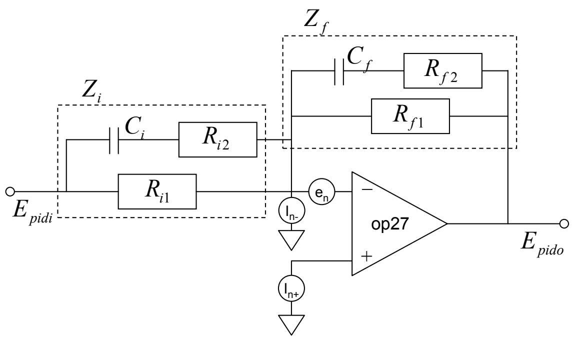

Figure 5.12 *Schematic of analogue PID controller*

Payload			Reference		
C_f	:	$0.29\ \mu F$	C_f	:	$83\ mF$
R_{f1}	:	$1.27\ M\Omega$	R_{f1}	:	$264\ k\Omega$
R_{f2}	:	$0.127\ M\Omega$	R_{f2}	:	$26.4\ k\Omega$
C_i	:	$53\ nF$	C_i	:	$1.8\ \mu F$
R_{i1}	:	$200\ k\Omega$	R_{i1}	:	$470\ k\Omega$
R_{i2}	:	$51.7\ k\Omega$	R_{i2}	:	$117\ k\Omega$

Table 5.2 *Parameters of the PID controllers*

Voltage noise

The noise at the PID output due to e_n is denoted by S_{pido,e_n}. From the voltage divider relationship between e_n and E_{pido}, S_{pido,e_n} can be obtained as (see Rodgers [18]):

$$S_{pido,e_n}(\omega) = \left|1 + \frac{Z_f(j\omega)}{Z_i(j\omega)}\right|^2 S_{e_n}(\omega) = |1 - P_{pid}(j\omega)|^2\, S_{e_n}(\omega) \tag{5.34}$$

since $-Z_f(j\omega)/Z_i(j\omega) = P_{pid}(j\omega)$.

Current noise

There is no noise generated by i_n since it directly connected to ground.
For currents from i_{n-} the same reasoning as in the set-point case holds, therefore, all of i_{n-} flows through Z_f, and none of it flows through Z_i (Rodgers [18]).
So for the current noise at the PID output due to i_{n-} we can write:

$$S_{pido,i_{n-}}(\omega) = |Z_f(j\omega)|^2\ \ S_{i_n}(\omega) \tag{5.35}$$

Adding up both obtained PSD's gives the total PSD at the PID output:

$$S_{pido}(\omega) = |1 - P_{pid}(j\omega)|^2\, S_{e_n}(\omega) + |Z_f(j\omega)|^2\ \ S_{i_n}(\omega) \tag{5.36}$$

The PID noise in the payload loop will be denoted by $S_{pid,p}$ and the noise in the reference loop by $S_{pid,r}$.

Servo amplifier noise

The task of the servo amplifier is to generate a current I_{umao} to drive the Lorentz actuator. A simplified electrical circuit configuration can be seen in Figure 5.13.

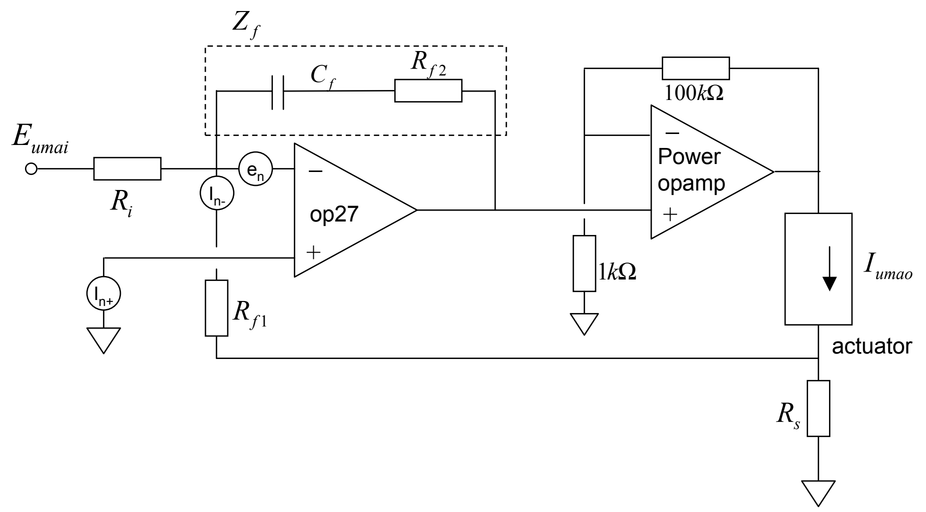

Figure 5.13 *Schematic of servo amplifier*

The input of the amplifier is the voltage signal E_{umai}. The opamp configuration will drive the power opamp that will provide for the necessary currents. The feedback loop via resistor R_{f1} closes the loop. It can be seen that the transfer function from input voltage E_{umai} to output current I_{umao} is equal to $R_{f1}/(R_i R_s)$.
The resistor and capacitor values for the payload and reference controller are listed in Table 5.3.

Payload			Reference		
C_f	:	$100\ nF$	C_f	:	$100\ nF$
R_{f1}	:	$6\ k\Omega$	R_{f1}	:	$750\ \Omega$
R_{f2}	:	$10\ k\Omega$	R_{f2}	:	$6\ k\Omega$
R_i	:	$2\ k\Omega$	R_i	:	$390\ k\Omega$
R_s	:	$0.2\ k\Omega$	R_s	:	$0.2\ k\Omega$

Table 5.3 *Parameters of the servo amplifiers*

The following noise analysis is based on Goossens [8]. The noise of the power opamp is negligible at the output I_{umao} because of the suppression of the feedback loop. The noise sources of the opamp cannot be neglected and will be modelled. The used opamp is an op27, and its noise can be modelled with three equivalent noise sources, also is shown in Figure 5.13. The currents of source I_{n+} cannot go anywhere, so this source will not cause noise at the output of the servo amp. The two remaining sources will cause noise at the current output as follows:

$$S_{uma,e_n}(\omega) = \left|1 + \frac{Z_f(j\omega)}{R_i}\right|^2 S_{e_n}(\omega) \quad [A^2/Hz] \tag{5.37}$$

$$S_{uma,i_{n-}}(\omega) = |Z_f(j\omega)||R_{f1}|^2 \; S_{i_n}(\omega) \quad [A^2/Hz] \tag{5.38}$$

where S_{e_n} and S_{i_n} are the voltage and current PSD of the op27 resp. as given in Section 5.4.2. Adding up both obtained PSD's gives the total PSD at the servo amp output:

$$S_{umao}(\omega) = \left|1 + \frac{Z_f(j\omega)}{R_i}\right|^2 S_{e_n}(\omega) + |Z_f(j\omega)||R_{f1}|^2 \; S_{i_n}(\omega) \tag{5.39}$$

The servo amp in the reference loop is similar to the one in the payload loop. The noise in the payload loop will be denoted by S_{uma} and the noise in the reference loop by S_{umi}.

5.4.3 Other disturbances and noise sources

Reference and payload mass disturbance forces

Disturbance forces can act on the reference mass and the payload mass. Reference disturbance forces can be caused by friction in the bearing or air pressure fluctuations above and underneath the reference mass. Acoustic noise can also be an important noise source. Unfortunately, it is unknown what the magnitudes these forces are and it is thus not possible yet to model these sources. Therefore, reference mass disturbance forces are not analyzed any further.

Payload disturbance forces can also be caused by air pressure variations and acoustic noise, but will mainly be due to forces caused by the payload itself, like internal vibrations or moving parts. These payload disturbance forces are characteristic to a certain payload application, and since the application is not fixed, it is not possible to make a model at this point.

5.4.4 Summary of disturbances and noise sources

Now all the disturbance and noise sources are discussed, lets summarize the results:
First of all, the floor noise was modelled as V_{floor} $[m/s^2/\sqrt{Hz}]$:

$$V(j\omega)_{floor} = 10^{-6} * \left(\frac{\frac{3}{2\pi}j\omega + 1}{\frac{3}{2\pi 10}j\omega + 1}\right)^3 \tag{5.40}$$

Then eight electrical noise sources were modelled as PSDs; the capacitive sensor noise in the payload and reference loop, $S_{sen,p}$, $S_{sen,r}$, the set-point noise in both the loops: $S_{set,p}$, $S_{set,r}$, and both the analogue PID controller noise sources: $S_{pid,p}$, and $S_{pid,r}$, all with units

$[V_{rms}^2/Hz]$. Finally the two servo amp PSDs S_{umi} and S_{uma} were modelled with units $[A_{rms}^2/Hz]$.

$$S_{sen,p}(\omega) = (10n)^2 \left(\frac{j\omega + 2\pi 700}{j\omega + 2\pi 70}\right)^4 \left(\frac{2\pi 1000}{j\omega + 2\pi 1000} \frac{2\pi 2000}{j\omega + 2\pi 2000}\right)^2 \tag{5.41}$$

$$S_{sen,r}(\omega) = (15n)^2 \left(\frac{j\omega + 2\pi 700}{j\omega + 2\pi 70}\right)^4 \left(\frac{2\pi 100}{j\omega + 2\pi 100} \frac{2\pi 160}{j\omega + 2\pi 160}\right)^2 \tag{5.42}$$

$$S_{set,p}(\omega) = \left(1 + \frac{5 \cdot 10^3}{50 \cdot 10^3}\right)^2 S_{e_n}(\omega) + (50 \cdot 10^3)^2 \; S_{i_n}(\omega) \tag{5.43}$$

$$S_{set,r}(\omega) = \left(1 + \frac{10 \cdot 10^3}{2 \cdot 10^3}\right)^2 S_{e_n}(\omega) + (2 \cdot 10^3)^2 \; S_{i_n}(\omega) \tag{5.44}$$

$$S_{pid,p}(\omega) = |1 - P_{pid,p}(j\omega)|^2 \, S_{e_n}(\omega) + |Z_{f\_p}(j\omega)|^2 \; S_{i_n}(\omega) \tag{5.45}$$

$$S_{pid,r}(\omega) = |1 - P_{pid,r}(j\omega)|^2 \, S_{e_n}(\omega) + |Z_{f\_r}(j\omega)|^2 \; S_{i_n}(\omega) \tag{5.46}$$

$$S_{uma}(\omega) = \left|1 + \frac{Z_{umaf}(j\omega)}{R_{umai}}\right|^2 S_{e_n}(\omega) + |Z_{umaf}(j\omega)||R_{umaf1}|^2 \; S_{i_n}(\omega) \tag{5.47}$$

$$S_{umi}(\omega) = \left|1 + \frac{Z_{umif}(j\omega)}{R_{umii}}\right|^2 S_{e_n}(\omega) + |Z_{umif}(j\omega)||R_{umif1}|^2 \; S_{i_n}(\omega) \tag{5.48}$$

The disturbance forces on the payload mass and reference mass are unknown and thus $S_{dist,p}$ and $S_{dist,r}$ are not modelled.

5.5 System performance

In this section the output noise level is calculated, using the noise models from the previous section. In order to calculate the noise propagation through the closed loop system, one needs a closed loop model, with inputs where the noise sources apply and with the performance variable as output. After that, the noise level at the performance output due to all the internal AIMS noise sources (so excluded ground vibrations) is calculated; every noise model is propagated towards the performance output of the system and the total noise level due to the internal AIMS noise sources is then calculated by adding the separate contributions quadratically. Finally, the vibration isolation performance of the AIMS is evaluated by comparing the performance of the passive basic isolator with the performance of the basic isolator together with the AIMS, which is build up out of two parts, one part due to the internal AIMS noise sources and one part due to the ground vibrations.

5.5.1 Modelling the closed loop system

Making a generalized plant

To propagate the noise models towards the performance output, a closed loop model with inputs there where the noise sources apply and with the performance variable as output is required, the closed loop system will have 11 inputs, $\bar{w_1}...\bar{w_{11}}$ and one single output z_1, as is depicted in Figure 5.14. The variable names correspond to Figure 5.9, over-bar denote that the variable is weighted by a filter $V_{..}(s)$ such that the signal contains the PSD of the noise source. A convenient way to make the closed loop model is by defining a generalized plant P, using the Matlab command `sysic` and to close the loop afterwards with the Matlab command `starp`. In this case the loop is closed with a two-by-two controller, with just the PID controllers on the diagonal. The result is the closed loop model H shown in Figure 5.15, which defines 11 transfer functions, one from every noise input towards the performance output. All these transfers are plotted in Figures 5.15-5.16. In the previous section only nine noise sources were actually modelled, corresponding to transfer functions 1-5 and 7-10. In the propagation analysis in the next section, only these transfers are used.

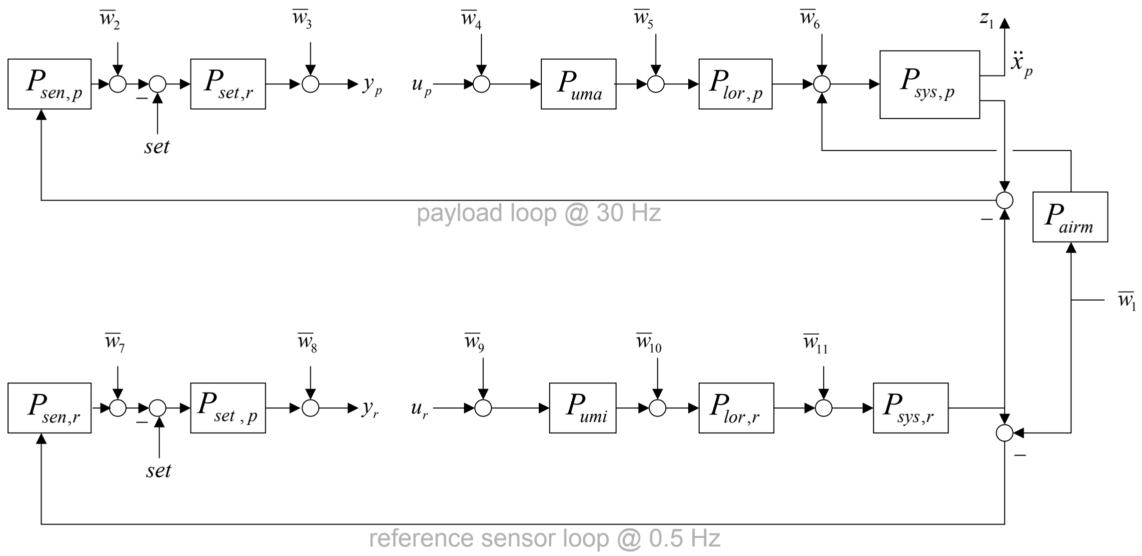

Figure 5.14 *The open loop system, defined in a, so-called, 'generalized plant' setting. The open loop system is denoted by P.*

5.5.2 Noise propagation

Now the closed loop transfer functions are available, the noise sources can be propagated towards the performance output. This is done for every noise source separately, using the equation

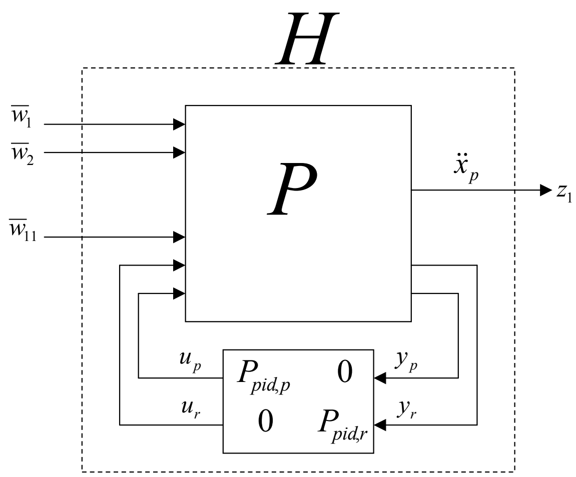

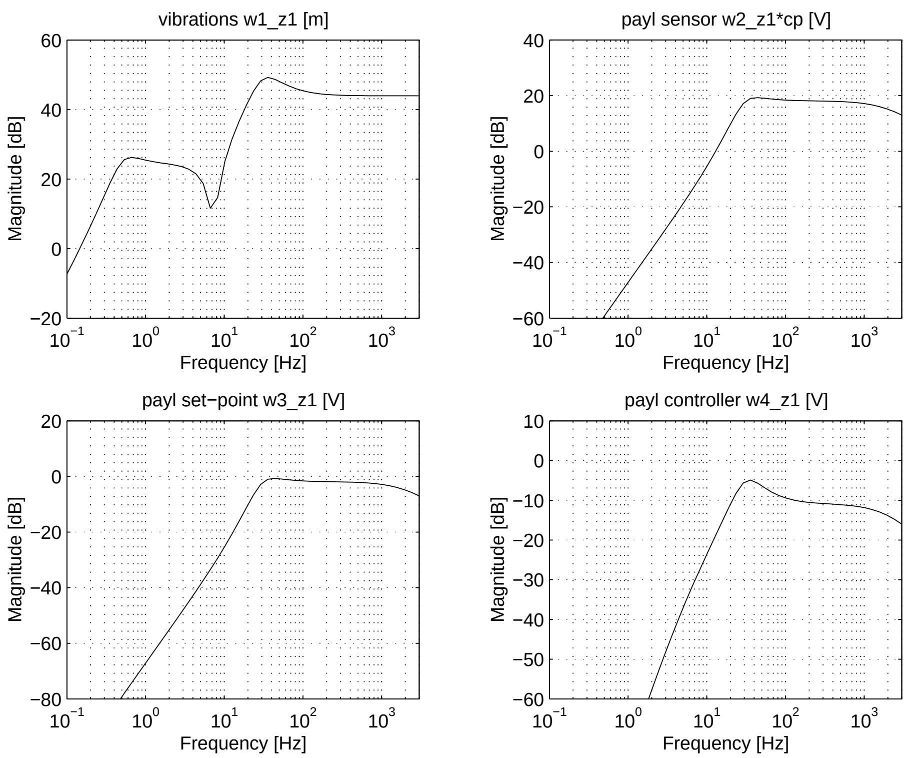

Figure 5.15 above: *The closed loop system H.* below: *Closed loop transfer functions from inputs 1-4 to the performance output $[m/s^2]$. (1) Ground vibrations $[m]$, (2) Payload sensor noise $[V]$, (3) Payload set-point noise $[V]$, (4) Payload PID controller noise $[V]$.*

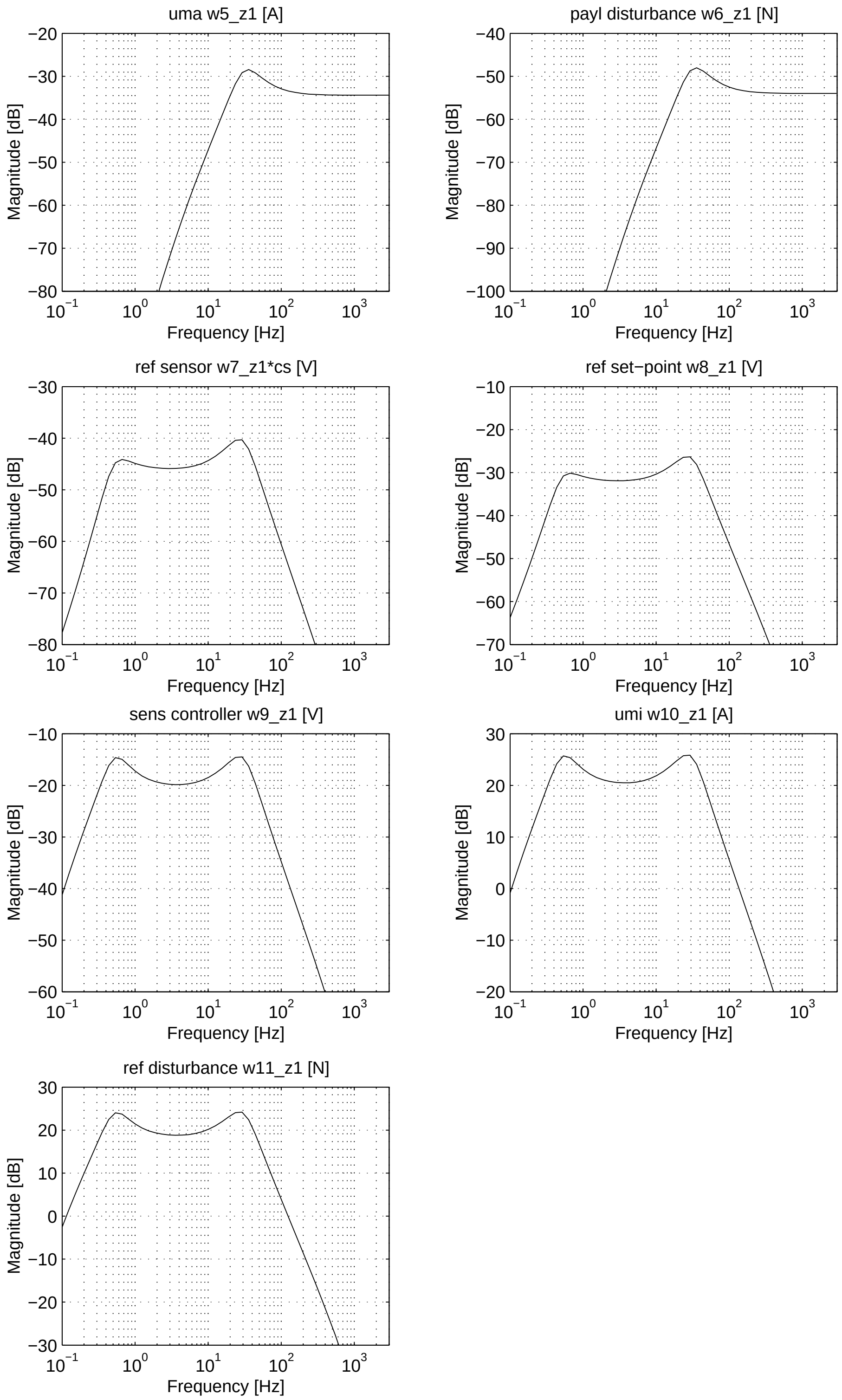

Figure 5.16 *Closed loop transfer functions from inputs 5-11 to the performance output [m/s^2]. (5) Payload servo amplifier noise [V], (6) Payload disturbance forces [N], this transfer function is generally known as the* compliance *of the vibration isolation system, (7) Reference sensor noise [V], (8) Reference set-point noise [V], (9) Reference PID controller noise [V], (10) Reference servo amplifier noise [V], (11) Reference disturbance forces [N].*

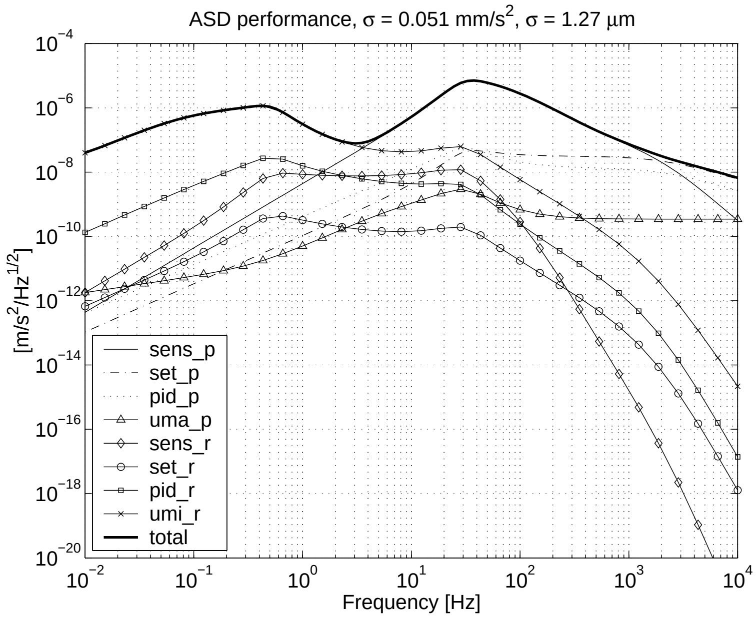

Figure 5.17 *Amplitude Spectral Density of the propagated noise sources separately and the ASD of the total signal.*

$$S_{out,i}(\omega) = |H_i(j\omega)|^2 \;\; S_{in,i}(\omega) \tag{5.49}$$

where $S_{in,i}$ is the input PSD and $S_{out,i}$ the resulting output PSD, both with units $[V_{rms}^2/Hz]$ and $H_i(j\omega)$ is the transfer function towards the performance output, corresponding to the noise source. In order to get the total output PSD, that is, the PSD of the output signal with all the noise sources acting on the system, all the separate output PSD's are simply added.

$$S_{out,tot}(\omega) = S_{out,1}(\omega) + \cdots + S_{out,4}(\omega) + S_{out,7}(\omega) + \cdots + S_{out,9}(\omega) \tag{5.50}$$

Performance analysis is commonly done using the resulting *Amplitude Spectral Density* (ASD) and the *Cumulative Amplitude Spectra* (CAS) instead of the PSD and CPS (see § 2.4.4). In Figure 5.17 the separate (ASDs) and the total ASD can be seen. The CAS can be seen in Figure 5.18 and in Figure 5.19 (left), which both represent the same CAS but with a different y-scale.

Analysis of the propagation results

Looking at the ASD in Figure 5.17, one can see that two noise sources are dominant; the servo amplifier noise in the reference loop is dominant in the lower frequency region and the sensor noise in the payload loop in the higher frequency region (>4 Hz). The servo amplifier noise has a peak around 3-5 Hz, and its power contribution to the error will therefore be

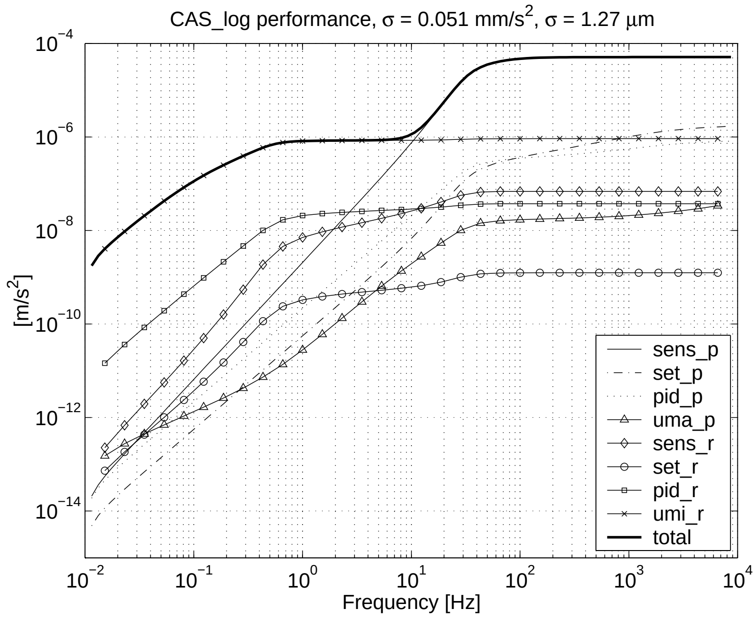

Figure 5.18 *Cumulative Amplitude Spectrum with a logarithmic y scale. Thanks to the logarithmic y scale one can still see the magnitude of the contribution of the other noise sources.*

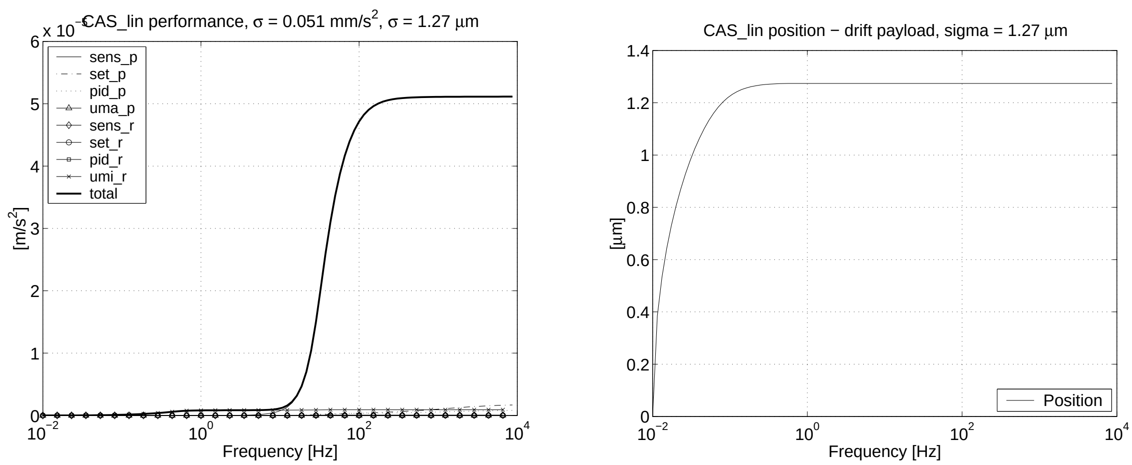

Figure 5.19 left*: Cumulative Amplitude Spectrum with a linear y scale. The separate and total CAS is plotted. The payload sensor contributes about 90% of the energy of the error signal.* right*: Cumulative Amplitude Spectrum with a linear y scale of the position error. The error is build op in the low frequency region (<0.1 Hz) and is due to the reference servo amplifier noise.*

mainly in that region. The payload sensor noise peaks at about the bandwidth of the payload loop, at 30 Hz.
In the logarithmic CAS in Figure 5.18 one can easily see that the payload sensor noise and the umi servo amplifier noise are indeed thé main contributors to the power of the performance signal, and in the linear CAS in Figure 5.19 (left) one can see that the payload sensor contributes about 90% of the power. The total power has a value of 0.051 mm/s^2 (1-σ).
Since the capacitive sensors are still in development, the noise model of the capacitive sensor is a preliminary noise model. Now that it turns out that the sensor is thé main contributor to the error, the designer knows that the development of this sensor is *crucial* to the success of the system. The knowledge that the sensor contributes most of the power at the performance output in the high frequency region, can be of help to the sensor designer.

In the logarithmic CAS it is visible that the second largest error contributor is the set-point noise of the payload loop, which adds a 1-σ value of about 0.002 mm/s^2 (relative to a 0.051 mm/s^2 from the payload sensor). So, although this noise source is not dominant in some frequency region, it adds more power than the dominant servo amplifier noise.
Due to the accelerations observed at the performance output, the payload also has a position disturbance. The ASD of this position error is found when the ASD expressed in $(mm/s^2)/\sqrt{Hz}$ is multiplied with $1/s^2$ (equalling double integration with respect to time). The final value of the corresponding CAS, shown in Figure 5.19 on the right hand side, gives the 1-σ value of the position disturbance. In this figure one can see that the error is build up in the low frequency region (<0.1 Hz). From the acceleration ASD of the error in Figure 5.17, it is visible that the error in this region is due to the reference servo amplifier noise, which caused a payload to drift 1.27 μm (1-σ).

Case: payload loop with 100 Hz open loop bandwidth

An interesting question is, how does the noise picture change when the payload loop bandwidth is increased, e.g., to 100 Hz. A motivation to increase the payload loop bandwidth is that the vibration isolation performance is then increased. This can be seen in Figure 5.20, where the 100 Hz transmissibility is shown (the 30 Hz transmissibility is also shown for reference). When one compares the 100 Hz transmissibility with the 30 Hz case, shown in Figure 5.8 on page 69, it is visible that the 100 hz case isolates up to 70 Hz, instead of 20 Hz in the 30 Hz case.
Another motivation to increase the bandwidth, is that payload disturbance forces are then suppressed up to 100 Hz instead of 30 Hz. One can see this when one looks at the transfer function from payload disturbance forces $\bar{w}_6$ to performance output z_1, or the compliance of the AIMS. The compliance for the 30 Hz case can be seen in Figure 5.16 above right, which starts to level at about 30 Hz. This will become 100 Hz in this case, achieving payload disturbance suppression up to this frequency. So, by increasing the open loop bandwidth of the payload loop, both the transmissibility and the compliance of the AIMS are increased! This improvement comes with a cost though, in the form of an increase in noise. The question now is, does the increase in performance counter balance the increase in noise? This

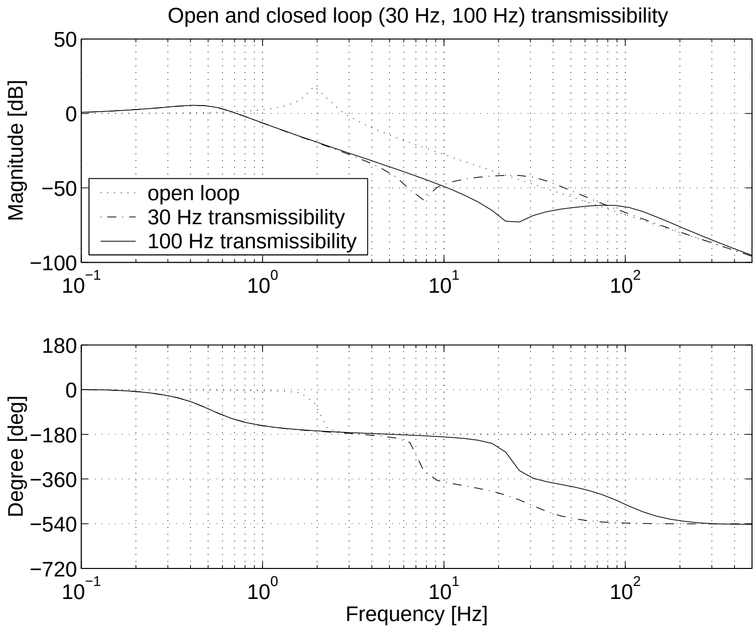

Figure 5.20 *The open and closed loop transfer function (transmissibility) of the AIMS with a 100 Hz open-loop payload loop bandwidth.*

question will be answered below.

The loop transfer function $L_p(s)$ is altered, by changing the PID controller $P_{pid,p}$, such that the open loop bandwidth of the payload loop is 100 Hz. The new coefficients of the controller are not given here. Since the components in the PID controller are different from the 30 Hz case, its noise contribution changes as well. The model was altered accordingly.

With the new loop gain function and noise model in place, the output error spectrum is calculated again. The propagation results can be seen in Figures 5.21-5.22.
Comparing Figure 5.17 with Figure 5.21, one can see that the overall noise picture is the same, except for that the total ASD being a bit higher. The reference servo amplifier noise and the payload PID controller noise are still the main contributors to the error spectrum, but their contribution is increased. So, by increasing the open loop bandwidth of the payload loop, the payload force disturbance suppression increases, but the total error due to the AIMS components increases as well.

Comparing the logarithmic CAS, one can see that the high frequency contribution of the payload set-point gain and the payload PID controller is increased, compared to the reference servo amplifier noise. This is also visible in the linear CAS, where the total error power even increases in the high frequency region due to these two noise sources.

The 1-σ value of the total error power now is 0.30 mm/s^2, compared to a value of 0.051

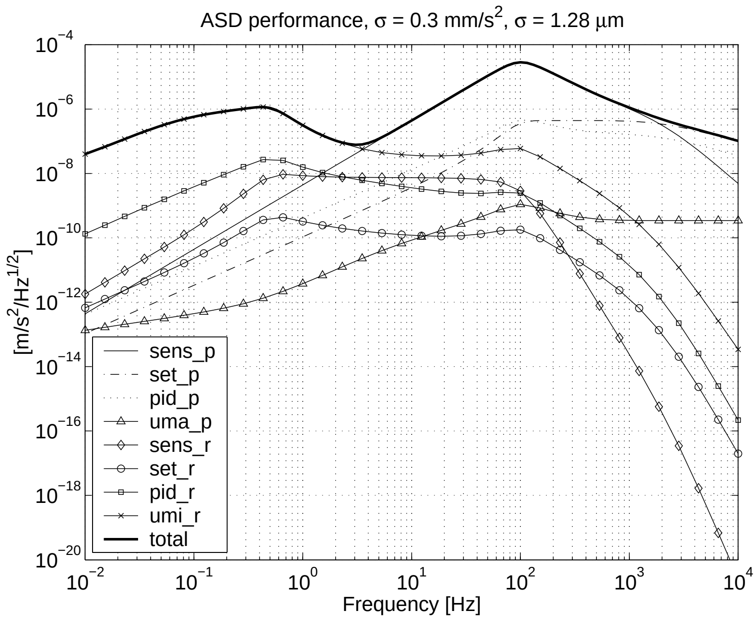

Figure 5.21 *Amplitude Spectral Density of the propagated noise sources separately and the ASD of the total signal in the 100 Hz case.*

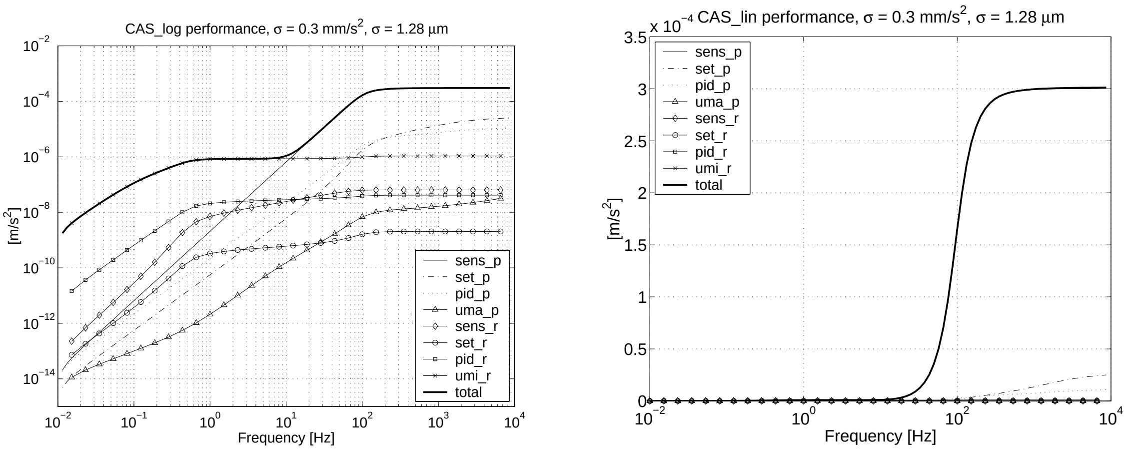

Figure 5.22 left*: Cumulative Amplitude Spectrum with a logarithmic y scale in the 100 Hz case.* left*: Cumulative Amplitude Spectrum with a linear y scale in the 100 Hz case.*

mm/s^2 in the 30 Hz case. Changing the system to a 100 Hz configuration, apparently decreases the performance with a factor of about 6. So, increasing the bandwidth to 100 Hz comes with rather large costs, and must be traded off with the gain in transmissibility and compliance. Since the performance specification of 0.1 mm/s^2 is exceeded with a factor three (0.30 mm/s^2), it is obvious that the increase in transmissibility alone does not counter balance the gain in noise. An appropriate trade off can only be made, when the ASD of the payload disturbance forces is known and brought into the analysis as a disturbance source.

The 1-σ value of the total position disturbance is increased from 1.27 μm to 1.28 μm, which is a negligible increment. This is because the noise due to the reference servo amplifier noise (which causes the drift) did not increase when the bandwidth was changed, as can be concluded from Figure 5.17 and 5.21.

5.5.3 Vibration isolation performance of the AIMS

How well does the AIMS perform concerning vibration isolation? The ground vibration model $V(j\omega)_{floor}$ $[m/s^2/\sqrt{Hz}]$, developed in Section 5.4.1 is used in this analysis to investigate the vibration isolation performance of the AIMS.
To investigate the vibration isolation performance, one can look at the open loop and closed loop (30 Hz case) ground vibration propagation transfer function. The ground vibration model (5.17) is defined in units $[m/s^2/\sqrt{Hz}]$, so the corresponding propagation transfer function is the transfer from acceleration of the ground: $\ddot{x_h}$ towards payload acceleration: $\ddot{x_p}$. This transfer function is the same as the one from ground position x_h to payload position x_p. The open and closed loop transfer function are already derived in Section 5.3.3 and can be seen in Figure 5.8 on page 69.
Using the open and closed loop transfer function, the floor noise spectrum is propagated towards the performance output. The performance of the AIMS can now be analyzed by comparing the open loop ASD (using only the basic isolator to isolate from vibrations) with the closed loop ASD due to vibrations combined with the closed loop ASD due to its noise sources, which was already calculated in Section 5.5.2. In the context of performance, the ASD due to the noise sources can be seen as the costs that have to be paid to use the AIMS in the closed loop setting.
Besides the performance of the open loop AVI using a basic (cheap) 2 Hz isolator, the (open loop) performance of a more expensive passive 0.5 Hz isolator (without using the AIMS) is also calculated. A 0.5 Hz isolator with 20% damping is the type of (passive)isolator which is used nowadays in industry e.g., an airmount. The performance level of the expensive 0.5 Hz isolator is the level that should be achieved by the cheap 2 Hz isolator in combination with the AIMS. The results can be seen in Figure 5.23 and 5.24.

In this figure it can be seen that the open loop 2 Hz isolator ASD is higher than the total closed loop ASD in the mid-frequency range. In the low and high frequency regions, the noise sources due to the AIMS dominate the closed loop spectrum, making the closed loop performance worse than the open loop performance. In the mid-frequency range, where the error due to ground vibrations dominate the total closed loop spectrum, the isolation

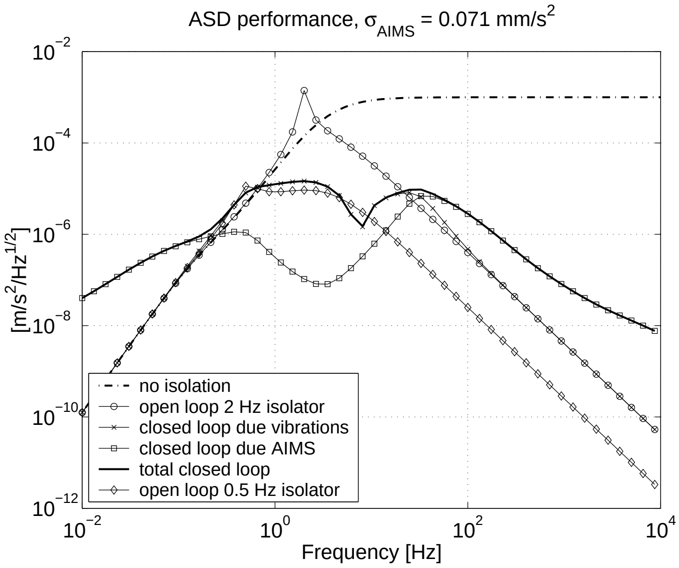

Figure 5.23 *ASD of the open loop and closed loop AIMS vibration isolation performance, together with the ASD of the ground itself (no isolation). The closed loop PSD is the ASD due to ground vibrations added with the PSD due to the noise sources of the AIMS.*

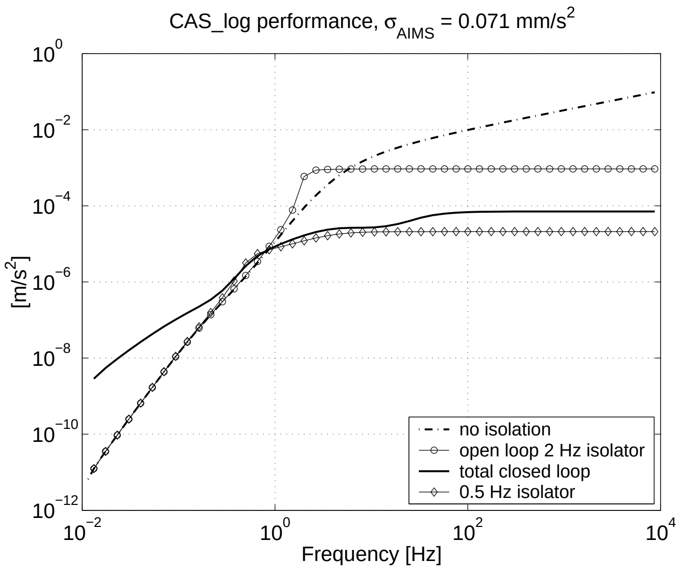

Figure 5.24 *CAS of the open and closed loop (30 Hz) AIMS, together with the CAS of the ground vibration itself (no isolation).*

performance of the AIMS proves its value, since it takes a huge 'bite' out of the open loop ASD.

To analyze the performance of the AIMS one has to look at the resulting power (1-σ) of the acceleration signal, and compare the no-isolation, open loop 2 Hz isolator, total closed loop and the 0.5 Hz isolator case. In Figure 5.24 four different CAS can be seen. The final value of the CAS equals the 1-σ value of the signal. The CAS of the ground vibrations (no isolation) gradually rises to 10 cm/s^2 at 10 kHz. The open loop CAS shows a steep rise in power around 2 Hz, where the 2 Hz isolator has its resonance frequency, and levels at a value of 0.94 mm/s^2. Because of the mass-spring characteristics of the 2 Hz isolator, the open loop CAS does not show any increase in power at frequencies higher than 2 Hz. The total closed loop CAS starts at a higher level in the lower frequency region, because of the power contributed by the electrical components of the AIMS in this region (see Figure 5.24). Around 1 Hz the level dives below the open loop level, because of the vibration-isolation performance of the AIMS. After 10 Hz it still rises a little, due to the payload sensor noise, but finally levels to 0.071 mm/s^2 around 100 Hz. The 0.5 Hz isolator still achieves the highest performance level: 0.021 mm/s^2. Comparing the CAS's, one can see that the main difference is made in the 10 - 30 Hz region, where the closed loop CAS shows an increase in power rises due to the payload sensor noise of the AIMS.
Summarizing; it is clear that the closed loop case performs significantly better than the open loop 2 Hz isolator; 0.071 mm/s^2 in the closed loop case compared to 0.94 mm/s^2 in the open loop case, which is about 13 times better. On the other hand, the more expensive 0.5 Hz isolator still achieves the highest performance level of 0.021 mm/s^2, 3.4 times better than the closed loop case!

5.6 Conclusions and recommendations

5.6.1 Conclusions

In this chapter it is shown that the DEB approach can be applied to a system that is still in the design phase. The DEB analysis shows that the AIMS concept is feasible in practice and points out the payload sensor noise as *the* main contributor of power to error signal. The simulations show that the 1-σ performance specification of 0.1 mm/s^2 is met when the payload loop-gain function has an open loop bandwidth of 30 Hz. In this case the power of the error due to the noise sources of the AIMS contribute 0.051 mm/s^2 to the total budget. When the ground vibrations themselves are added to the analysis, the final performance level increased to 0.071 mm/s^2. The closed loop AIMS system (parallel with the passive 2 Hz isolator) does not achieve a higher performance level than the more expensive 0.5 Hz passive isolator, which achieves an open loop performance level of 0.021 mm/s^2.

When using a 100 Hz payload-loop-bandwidth, the AIMS will not achieve the performance specification, since the electrical components of the AIMS themselves already contribute 0.30 mm/s^2, which is three times the performance specification of 0.1 mm/s^2. Almost all of this error is due to the payload sensor. So, the 30 Hz case is the configuration to choose, unless a better payload sensor is developed.

It has to be said that it is likely that other un-modelled disturbances, like air pressure fluctuations and disturbance (friction) forces, will also add a significant part to the error budget. So, in order to achieve the spec of 0.1 mm/s^2 in practice, the simulated value has to be significantly smaller than the specification, which is fortunately the case in the 30 Hz configuration (0.051 mm/s^2).

5.6.2 Recommendations

The capacitive payload sensor turns out to be *the* main contributor of power to the performance output, and most of this power is contributed in the high frequency region (>100 Hz). Since the sensor is still in development, the designer should design the sensor with this knowledge in mind, such that the final system meets the performance specification.

The $\mathcal{H}_2$ control strategy can be used in this case study to find out if the control strategy used in the case study is close to optimal. The two PID controllers used in the setup now are designed with a certain closed loop behavior in mind. The reference controller is designed to achieve a closed loop 0.5 Hz suspension behavior of the reference mass. The payload controller is designed such that the closed payload loop can suppress reference disturbances up to 30 Hz. It could well be that this control strategy is far from the optimal strategy, which is given by the $\mathcal{H}_2$ control strategy. The $\mathcal{H}_2$ control strategy could be used to synthesize e.g., only the payload loop controller and consider the reference loop controller as fixed and vice versa. With this approach two SISO controllers can be found. On can also go one step further, by considering both controllers as a degree of freedom and synthesize a MIMO $\mathcal{H}_2$ controller. The extra control degree of freedom given by the of diagonal terms of the MIMO controller might offer and opportunity to increase performance even more. One disadvantage of this approach is that the MIMO controller might be hard to interpret.

Chapter 6

Conclusions and recommendations

6.1 Conclusions on the DEB design approach

In this research the Dynamic Error Budgeting (DEB) design approach is developed. With the tools offered by the DEB design approach, the designer is able to account for stochastic disturbances during the design of a mechatronic system. The DEB approach requires disturbance models, a model of the system and a controller as input and then offers the designer tools to predict the performance of the system a priori and gain insight in the performance limiting factors of the system. With this insight, the designer is able to point out critical system components/properties and make design decisions that improve the performance of the system.
$\mathcal{H}_2$ control strategy is presented as an extension to the DEB approach. It offers the designer the opportunity to optimize over the degree of freedom given by the controller, enabling the designer to predict the maximum achievable performance level of a system concept. Using this technique, the designer is able to objectively compare the performance potential of different system concepts.
When different system components are designed at different locations, the DEB design approach reaches the system designer a tool to keep the overview of the total system and to keep track of the final performance of the system, taking in account all disturbances. This helps the designer to design complex systems 'first time right', significantly reducing design costs and time.

By applying the DEB approach in two (one DOF) vibration isolation case studies, its feasibility in practice is shown. In both studies, the disturbances are modelled and the performance of the system predicted. In the first case study the gap between theory and practice is analyzed and the discrepancies between theoretical and experimental results explained. Both case studies show that, using the DEB analysis tool, the designer is able to point out critical components and to make design decisions that improve the performance of the system.

In the first case study the critical system component turned out to be the AD converter. The design of the system was improved by introducing a preamplifier just before the converter, increasing the performance level with a factor of 30. Then another improvement was made by applying an $\mathcal{H}_2$ control strategy to control the system, which increased the performance even further with a factor of about 4. The theoretical performance improvements were validated with experiments. It is also shown that, with the use of Pareto curves, the designer is able to objectively compare different system designs in practice.

In the second case study the DEB approach is applied to the design of a system in practice. Using the tools available it is shown that the performance of the concept design can be predicted and critical disturbances/components can be pointed out a priori, showing that the approach is feasible in practice. It is shown that the design concept is feasible and that the critical system component is the capacitive payload sensor. The effect of changing the bandwidth of the system on performance was analyzed by comparing the performance using two different bandwidths, showing a big difference in final performance.

6.2 Recommendations and further work

An interesting and very important question in the DEB design approach is what performance variable to choose? The analysis would have been different when in the first case study, instead of the load velocity, e.g., the load acceleration level was chosen as the performance measure. This choice greatly depends on the application of the system. An interesting point for further research is to investigate what the consequences are for the design of the system when a different performance variable is chosen and how this is related to the performance objective of the system in practice.

The accuracy of the predicted performance by DEB with respect to the measured results, can be improved by using higher order models of the disturbances. Increasing the order of the disturbance model might even allow (approximate) modelling of harmonic disturbances by using inverse notches. How accurate this can be done is an interesting item for future research. To achieve the highest degree of prediction accuracy is it recommended to use the actual measured disturbance spectra in the simulations.
If there is a discrepancy between the theoretical and measured performance PSD, a way to deal with it is to accredit the difference to an additional artificial disturbance, such that the difference in output power is contributed by this input disturbance. In this way the designer has a possibility to account for this difference in power in the simulations. An interesting question that remains is where to put the input of the additional disturbance.
An explanation for such a discrepancy could be that the input disturbances are not uncorrelated and that the disturbance propagation relation should also contain cross power spectra such the correlation is accounted for. Another way to deal with correlated disturbances, is to (re)model the disturbances such that they originate from the a new single input. In this way the need to use cross power spectra in the propagation relation is circumvented.

In this research the DEB approach is applied to a one DOF (SISO) system. An interesting follow-up of this research is use the approach with the design of a MIMO setup e.g., a 2

DOF system.

When an $\mathcal{H}_2$ controller is synthesized for a particular system, it can give the control designer useful hints about how to control the system best for optimal performance. Drawbacks however are, that no robustness guarantees can be given and that the order of the $\mathcal{H}_2$ controller will generally be too high for implementation. Research can be done on how to use the information given by the $\mathcal{H}_2$ controller to the designers advantage in practice.

Further work can also be done on developing a DEB design *strategy*. In this thesis it is discussed that the DEB analysis tools enable the designer to make performance improving design decisions. The decisions must be made on the basis of the analysis and designer instinct. It is interesting to investigate if a strategy can be developed that can be followed to improve the system performance. A suggestion for this strategy is the balancing approach as discussed in Section 4.4. In this approach the disturbances introduced by a noise source and e.g., an extra gain, which is supposed to suppress the negative effect of the disturbance on performance, must be balanced at the performance output.

Appendix A

Mathematics

A.1 MATLAB code for computing the PSD and CPS

Consider the discrete time signal $x_L[n]$, containing L samples in variable `datavec`, using sample time T_s seconds. If the data set is too big, you might want to re-sample the time signal using the MATLAB® command `decimate`, before applying the code below. Mind, that the original continuous time signal is not allowed to have power content above the Nyquist frequency $1/(2T_s)$, to avoid anti-aliasing effects.

```
T_r = L*T_s;                      % signal time range
d_f = 1/T_r;                      % width of frequency grid
F_s = 1/T_s;                      % sample frequency
F_n = F_s/2;                      % Nyquist frequency
F = [0:d_f:F_n];                  % one sided frequency grid

% Discrete Time Fourier Transform Wxx
Wxx = fft(datavec - mean(datavec))/L;

% Two-sided Power Spectrum Pxx [SI^2]
Pxx = Wxx.*conj(Wxx);

% Two-sided Power Spectral Density Sxx_t [SI^2/Hz]
Sxx_t = Pxx/d_f;

% One-sided Power Spectral Density Sxx_o [SI^2/Hz] defined on F
Sxx_o = 2*Sxx_t;

% Two-sided Cumulative Power Spectrum CPxx [SI^2]
CPxx = cumsum(Pxx);

% Variance of signal from time data and frequency data
var_time = var(datavec); var_psd = 2*CPxx(floor(L/2));
```

A.2 Standard assumptions in the $\mathcal{H}_2$ framework

The material covered in this appendix is discussed in more detail in a feasibility study of the dynamic error budgeting approach by Monkhorst [12].
For $\mathcal{H}_2$ controller synthesis using the MATLAB® command `hinfsyn`, the system needs to be defined in a generalized plant setting, which has to meet the standard assumptions. The open loop system G in Figure A.1 is shown in a generalized plant setting, having n stacked disturbance inputs w and k stacked performance outputs z. The controller input y is defined as output and the controller output u as input of G. The input weighting filters $V_w(j\,2\pi f)$, used to model the disturbances can also be seen.

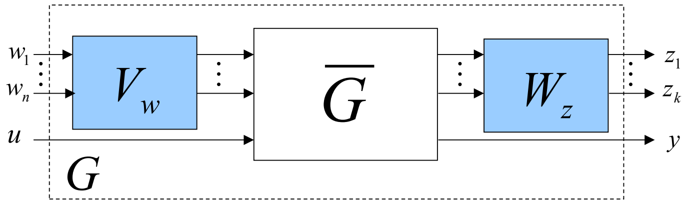

Figure A.1 *The open loop system $\bar{G}$ in series with the diagonal input weighting filter V_w and diagonal output scaling filter W_z defining the generalized plant G.*

Assume that $G(s)$ can be written as:

$$\begin{bmatrix} \bar{z} \\ y \end{bmatrix} = \underbrace{\begin{bmatrix} G_{11}(s) & G_{12}(s) \\ G_{21}(s) & G_{22}(s) \end{bmatrix}}_{G(s)} \begin{bmatrix} \bar{w} \\ u \end{bmatrix} \tag{A.1}$$

and each subsystem $G_{ji}(s)$ is defined by the state space matrices A, B_i, C_j and D_{ji}, as depicted in Figure A.1.

		w	u
	A	B_1	B_2
z	C_1	D_{11}	D_{12}
y	C_2	D_{21}	D_{22}

Table A.1 *State space matrices and signals of the open loop generalized plant*

For the controller design techniques described by Doyle *(et.al.)* [6] to be applicable, the following technical assumptions on the generalized plant G have to be met, see [5, 4, 27].

1. D_{11} must be zero.
2. (A, B_2) is stabilizable.
3. (A, C_2) is detectable.
4. D_{12} has full column rank.

5. D_{21} has full row rank.
6. $\begin{bmatrix} A - j\omega I & B_2 \\ C_1 & D_{12} \end{bmatrix}$ has full column rank at all frequencies ω.
7. $\begin{bmatrix} A - j\omega I & B_1 \\ C_2 & D_{21} \end{bmatrix}$ has full row rank at all frequencies ω.

Assumption 1 implies that there is no direct feedthrough from disturbance signals w to performance outputs z. Assumptions 2 and 3 imply that the generalized plant G must be detectable and stabilizable by the controller. Assumption 4 means that a part of *every* entry in u is present in the performance variable z, such that the control effort u is always penalized. Assumption 5 means that every measured output y must always be contaminated with a disturbance.
Finally, assumptions 7 and 6 imply that $G_{12}(s)$ and $G_{21}(s)$ may not have transmission zeros.

Appendix B

Noise and system modelling

B.1 State space model of the vibration isolation setup

In Trumper [24] a state space model is derived to model a two degree of freedom vibration isolation setup. This model is here derived again for the setup used in the first case study in this thesis.
The speaker, together with the rigidly mounted geophone can be modelled as a fourth order, two degree of freedom system, with a force f_s acting as the driving actuator force as shown in Figure B.1.

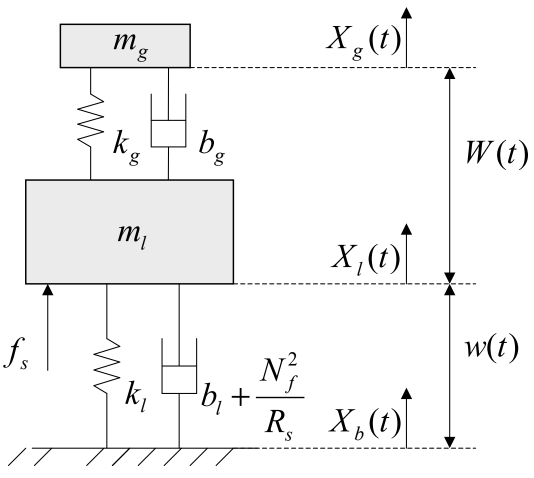

Figure B.1 *Model of the speaker with the mounted geophone. The system has two degrees of freedom, defined as $w(t)$ and $W(t)$.*

The parameters m_l, k_l, b_l and N_f represent the weight of the cone structure (including the geophone casing, cone plate etc.), the speaker suspension-stiffness, the speaker suspension damping-coefficient and the speaker force constant resp. Note the extra damping term N_f^2/R_s to account for the back emf in the voice coil. The geophone proof mass m_g, leaf spring stiffness k_g and suspension damping b_g are derived in § 3.2.3.

To derive an expression for the force f_s, let us look at the electrical relations of the voice coil. When a current I_s is send through the voice coil a force F_s is created. This force is given by $F_s = N_f I_s$, where N_f [N/A] is called the speaker force constant. This constant is characteristic for a particular speaker type and also varies with the axial position of the voice coil relative to the magnets. For the sake of simplicity this value is now assumed constant. More details on calculating N_f can be found in [24]. The electrical relationship for the voice coil is:

$$E_{sp} = R_s I_s + \underbrace{N_f(\dot{X}_l - \dot{X}_b)}_{back\ emf} \tag{B.1}$$

where E_{sp} is the voltage applied at the input terminals of the voice coil and R_s is the voice coil impedance. The second term on the right is to account for the back emf generated when the voice coil moves relatively to the magnets. Rewriting for I_s and substituting I_s in to $F_s = N_f I_s$ gives us for F_s

$$F_s = \underbrace{\frac{E_{sp} N_f}{R_s}}_{f_s} - \underbrace{\frac{N_f^2(\dot{X}_l - \dot{X}_b)}{R_s}}_{additional\ damping} \tag{B.2}$$

Note that the second term on the right-hand side acts as an additional damping term on the speaker motion and that the term f_s is the actual driving force applied to the voice coil, as shown in Figure B.1.

Defining the relative positions as the states of the system:

$$\begin{aligned} w(t) &= X_l(t) - X_b(t) && \text{(B.3)} \\ W(t) &= X_g(t) - X_l(t) && \text{(B.4)} \\ & && \text{(B.5)} \end{aligned}$$

and defining input $\mathbf{u} = [\mathbf{E_{sp}} \quad \ddot{\mathbf{X}}_\mathbf{b} \quad \mathbf{F_d}]^{\mathrm{T}}$ and output $\mathbf{y} = [\mathbf{E_g} \quad \ddot{\mathbf{X}}_\mathbf{l}]^{\mathrm{T}}$, the state space model can be written as

$$\begin{aligned} \dot{\mathbf{x}} &= \mathbf{Ax} + \mathbf{Bu} \\ \mathbf{y} &= \mathbf{Cx} + \mathbf{Du} \end{aligned} \tag{B.6}$$

with

$$
\begin{aligned}
\mathbf{A} &= \begin{bmatrix} 0 & 0 & 1 & 0 \\ 0 & 0 & 0 & 1 \\ -\frac{k_l}{m_l} & \frac{k_g}{m_l} & -\frac{b_l+N_f^2/R_s}{m_l} & \frac{b_g}{m_l} \\ \frac{k_l}{m_l} & -k_g\left(\frac{1}{m_l}+\frac{1}{m_g}\right) & \frac{b_l+N_f^2/R_s}{m_l} & -b_g\left(\frac{1}{m_l}+\frac{1}{m_g}\right) \end{bmatrix} \\
\mathbf{B} &= \begin{bmatrix} 0 & 0 & 0 \\ 0 & 0 & 0 \\ \frac{N_f}{R_s m_l} & -1 & \frac{1}{m_l} \\ -\frac{N_f}{R_s m_l} & 0 & -\frac{1}{m_l} \end{bmatrix} \\
\mathbf{C} &= \begin{bmatrix} 0 & 0 & 0 & G_g \\ -\frac{k_l}{m_l} & \frac{k_g}{m_l} & -\frac{b_l+N_f^2/R_s}{m_l} & \frac{b_g}{m_l} \end{bmatrix} \\
\mathbf{D} &= \begin{bmatrix} 0 & 0 & 0 \\ \frac{N_f}{R_s m_l} & 0 & \frac{1}{m_l} \end{bmatrix} \\
\mathbf{x} &= \begin{bmatrix} w & W & \dot{w} & \dot{W} \end{bmatrix}^{\mathrm{T}} \\
\mathbf{u} &= \begin{bmatrix} E_{in} & \ddot{X}_b & F_d \end{bmatrix}^{\mathrm{T}}
\end{aligned}
\tag{B.7}
$$

Half of the parameters in the state space model are still unknown, except for the geophone parameters m_g, b_g and k_g, which are derived in § 3.2.3, and the voice coil impedance $R_s = 4\Omega$ given by the manufacturer. To identify the remaining parameters m_l, b_l, k_l and N_f, the state space mode was fitted by hand on the the empirical model $P_{speaker}$ obtained in § 3.2.3.
The resulting parameters values are given in Table B.1. The following parameters are obtained from fitting the model to the swept sine data: k_l, b_l, m_l and N_f. A remarkable result is the zero damping coefficient of the speaker, which can be interpreted as follows; the damping in the speaker system is mainly due to the back emf generated in the voice coil. The value of b_l is probably not zero in reality, but can be assumed zero for the modelling purposes in this case study.

Stiffness coefficient k_l	:	4000 N/m
Damping coefficient b_l	:	0 N/m/s
Mass coefficient m_l	:	485 grams
Speaker force constant N_f	:	11 N/A
Voice coil impedance R_s	:	4 Ω

Table B.1 *Speaker parameter values*

B.2 Peterson New High/Low Noise Model

The material in this appendix is copied out Peterson [15] and is repeated here for convenience in case of later use. The New High Noise Model is a spectrum of average high seismic background noise at seismometer stations across the globe and can be viewed as an upper bound of seismic background noise. The Low High Noise Model represents the average low seismic background noise at the quietest sites across the globe.
The New High Noise Model (NHNM) can be expressed in acceleration, velocity or position density as follows:

$$\mathrm{NHNM}_{acc} = A + B\log(P) \quad [10\log((m/sec^2)^2/Hz)] \tag{B.8}$$
$$\mathrm{NHNM}_{vel} = \mathrm{NHNM}_{acc} + 20.0\log(P/(2\pi)) \quad [10\log((m/sec)^2/Hz)] \tag{B.9}$$
$$\mathrm{NHNM}_{pos} = \mathrm{NHNM}_{acc} + 20.0\log(P^2/(4\pi^2)) \quad [10\log(m^2/Hz)] \tag{B.10}$$

For the NLNM identical equations hold. Line parameters are given in Table B.2.

P_{nhnm}	A_{nhnm}	B_{nhnm}	-	P_{nlnm}	A_{nlnm}	B_{nlnm}
0.10	-108.73	-17.23		0.10	-162.36	5.64
0.10	-108.73	-17.23		0.17	-166.70	0
0.22	-150.34	-80.50		0.40	-170.00	-8.30
0.32	-122.31	-23.87		0.80	-166.40	28.90
0.80	-116.85	32.51		1.24	-168.60	52.48
3.80	-108.48	18.08		2.40	-159.98	29.81
4.60	-74.66	-32.95		4.30	-141.10	0
6.30	0.66	-127.18		5.00	-71.36	-99.77
7.90	-93.37	-22.42		6.00	-97.26	-66.49
15.40	73.54	-162.98		10.00	-132.18	-31.57
20.00	-151.52	10.01		12.00	-205.27	36.16
354.80	-206.66	31.33		15.60	-37.65	-104.33
				21.90	-114.37	-47.10
				31.60	-160.58	-16.28
				45.00	-187.50	0
				70.00	-216.47	15.70
				101.00	-185.00	0
				154.00	-168.34	-7.61
				328.00	-217.43	11.90
				600.00	-258.28	26.60
				10000	-346.88	48.75

Table B.2 *Line parameters for constructing the NHNM and NLNM curve given the period (P) or frequency (1/P).*

B.3 Building the preamplifier

B.3.1 Preamplifier transfer function

The output voltage signal of the preamplifier is denoted by E_{out}. Its input signal is the geophone output E_g. The transfer function of the preamplifier can be written as a series connection of two first order lag filters:

$$\frac{E_{out}}{E_g} = \underbrace{\left(G_{pa1}\frac{\tau_p s+1}{\alpha_p \tau_p s+1}\right)}_{first\ stage}\underbrace{\left(G_{pa2}\frac{\tau_p s+1}{\alpha_p \tau_p s+1}\right)}_{second\ stage} = G_{pa}\left(\frac{\tau_p s+1}{\alpha_p \tau_p s+1}\right)^2 \tag{B.11}$$

with $\tau_p = 1/\omega_1 = 1/(2\pi\ 0.45)$ and $\alpha_p = 10$, which puts the corner frequencies in the right place. With the gains chosen as $G_{pa1} = 100$ and $G_{pa2} = 10$ ($G_{pa} = 1000$), the total transfer equals the wanted preamplifier transfer shown in Figure 3.15. The two first order parts of the preamplifier are referred to as the *first* and the *second stage*.

As one might have noticed, the preamplifier transfer function resembles exactly a part of the controller (3.5 on page 26). So, by using *this* preamplifier, a part of the controller is actually shifted up the control loop to improve the SNR.

B.3.2 Preamplifier circuit design

The wanted preamplifier must have a second order transfer function (B.11), which can be written as a series connection of two first order stages, the *first stage* and *second stage*. A preamplifier stage with a second order transfer function can be physically achieved with the circuit configuration as shown in Figure B.2.

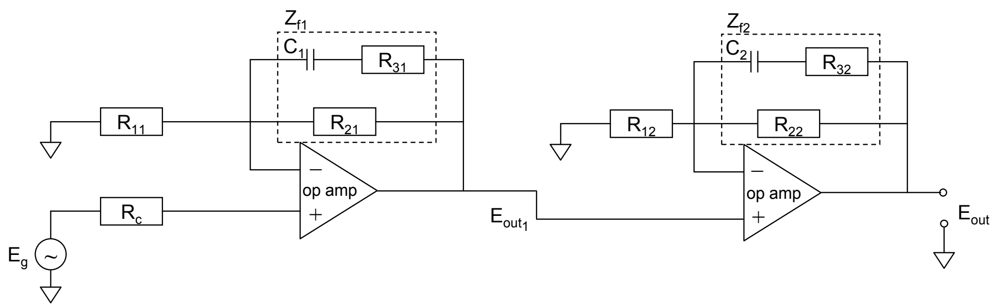

Figure B.2 *A two stage preamplifier circuit configuration. The geophone output signal E_g is fed in to the non inverting input of the first opamp. The output of the first stage E_{out_1} is then fed into a the second stage. The output of the second stage E_{out} is the final preamplifier output. R_{11}, R_{21}, R_{31}, R_{12}, R_{22}, R_{32}, represent resistors and C_1, C_2 capacitors. Their values determine the transfer function of the preamplifier. The variables $Z_{f1}(s)$ and $Z_{f2}(s)$ represent impedances defined by the dashed box enclosures. The triangles represent the signal common.*

The geophone output E_g is connected to the non-inverting input of the operational amplifier (opamp) of the first stage, which has the advantage over the inverting input concerning noise levels, as is discussed in Rodgers [18] and [19]. Since the transfer function of a single stage (B.11) has 3 DOF's (e.g.,, G_{pa1}, α_1, and τ_1) and a preamp stage has 4 DOF's, there is one DOF left, which gives a degree of freedom in choosing the physical components.

B.3.3 Preamplifier transfer function in physical component values

The total transfer function of the preamplifier as shown in Figure B.2, will be denoted by Z_{pa} and can be written as ([10]):

$$Z_{pa}(s) = Z_{pa1}(s)Z_{pa2}(s) = (1 + Z_{f1}(s)/R_{11})\,(1 + Z_{f2}(s)/R_{12}) \tag{B.12}$$

where $Z_{pa1}(s)$ is the transfer function of the first stage and $Z_{pa2}(s)$ of the second stage.

Transfer function of the first stage, Z_{pa1}

The transfer function of the first stage is now written as:

$$Z_{pa1}(s) = 1 + Z_{f1}(s)/R_{11} \tag{B.13}$$

and must be expressed in terms of the resistors values and the capacitor value. The impedance $Z_{f1}(s)$ is given by the parallel combination of R_{21} and the series connection of C_1 and R_{31}, or written out:

$$\begin{aligned} Z_{f1}(s) &= \left(\tfrac{1}{C_1 s} + R_{31}\right)||R_{21} = \tfrac{R_{31}C_1 s+1}{C_1 s}||R_{21} = \\ &= \tfrac{R_{21}R_{31}C_1 s+R_{21}}{(R_{21}+R_{31})C_1 s+1} = \tfrac{R_{21}||R_{31}C_1 s+\frac{R_{21}}{R_{21}+R_{31}}}{C_1 s+\frac{1}{R_{21}+R_{31}}} \end{aligned} \tag{B.14}$$

Interpreting $Z_{f1}(s)$: at low frequencies ($s \approx 0$) the capacitor is open (no connection) and $Z_{f1}(s)$ equals R_{21}, at high frequencies ($s \to \infty$) the capacitor is closed (short circuited) and $Z_{f1}(s)$ equals the parallel combination of R_{21} and R_{31}: $R_{21}||R_{31}$.
Notice that, when C_1 and R_{31} are set to zero the impedance $Z_{f1}(s)$ just equals the resistor value R_{21}.

$Z_{pa1}(s)$ can now be written as

$$Z_{pa1}(s) = 1 + Z_{f1}/R_{11} = \frac{(R_{11} + R_{21}||R_{31})C_1 s + \frac{R_{11}+R_{21}}{R_{21}+R_{31}}}{R_{11}C_1 s + \frac{R_{11}}{R_{21}+R_{31}}} \tag{B.15}$$

The low and high frequency gain of this $Z_{pa1}(s)$ are given by resp.:

$$Z_{pa1}(0) = \frac{R_{11} + R_{21}}{R_{11}}, \qquad Z_{pa1}(\infty) = \frac{R_{11} + R_{21}||R_{31}}{R_{11}} \tag{B.16}$$

and the two corner frequencies, in radians per second, are located at

$$\omega_1 = \frac{1}{(R_{21} + R_{31})C_1}, \qquad \omega_2 = \frac{1}{(R_{31} + R_{21}||R_{11})C_1} \tag{B.17}$$

We can now equal the transfer function of $Z_{pa1}(s)$ with the corresponding part of Equation B.11 which *can* result in the following equations (R_{11} is chosen as the degree of freedom):

$$\begin{aligned} R_{21} &= R_{11}(G_{pa1} - 1) \\ R_{31} &= R_{11}R_{21}\left((G_{pa1}/\alpha_p - 1)/(R_{21} - R_{11}(G_{pa1}/\alpha_p - 1))\right) \\ C_1 &= 1/(\omega_1(R_{21} + R_{31})) \end{aligned} \tag{B.18}$$

Transfer function of the second stage, Z_{pa2}

The derivation of the transfer function $Z_{pa2}(s)$ is completely similar to that of Z_{pa1} shown above, and is not repeated here. The transfer function of Z_{pa2} can be written as:

$$Z_{pa2}(s) = 1 + Z_{f2}/R_{12} = \frac{(R_{12} + R_{22}||R_{32})C_2 s + \frac{R_{12}+R_{22}}{R_{22}+R_{32}}}{R_{12}C_2 s + \frac{R_{12}}{R_{22}+R_{32}}} \tag{B.19}$$

B.3.4 Physical parameter values for the 1000-10 preamplifier

For the first stage the parameters are given by: $G_{pa1} = 100$, $\alpha_p = 10$ and $\omega_1 = 1/(2\pi\, 0.45)\ rad/sec$, as obtained earlier in this section. Setting R_{11} to 3.6 $k\Omega$ and using Equations B.18, we obtain: $R_{21} = 356400\ \Omega$, $R_{31} = 35640\ \Omega$ and $C_1 = 0.9\ \mu F$.
For the second stage the parameters are given by: $G_{pa2} = 10$ and α_p and ω_1. Plugging in $R_{12} = 43\ k\Omega$, returns: $R_{22} = 387\ k\Omega$, $R_{32} = 0\Omega$ and $C_2 = 0.91\ \mu F$.
A preamplifier with these component values was build and used in the isolation system. A photograph of the build preamp is shown in Figure B.3.

It is not a coincidence that the two capacitor values are about 0.9 μF. The output noise level of the preamplifier increases with increasing resistor values, as will be shown in the next Subsection. The bigger the capacitor value is chosen, the smaller the resistor values will be (this is clear when you plot the dependency described by Equations B.18, not shown here). Since the capacitor size increases rapidly with its capacitance, there is a practical limit to the usable capacitance value (the size of the circuit board should be as small as possible in order to avoid noise pick up). 0.9 μF was chosen in this case, and the values of R_{11} and R_{12} were chosen to meet this requirement.

B.4 A noise model for the preamplifier

B.4.1 Introduction preamplifier noise modelling

To develop a noise model for the preamplifier, all the noise models of the noise generating components will be modelled first. After that, a total noise model of the preamplifier will be derived.

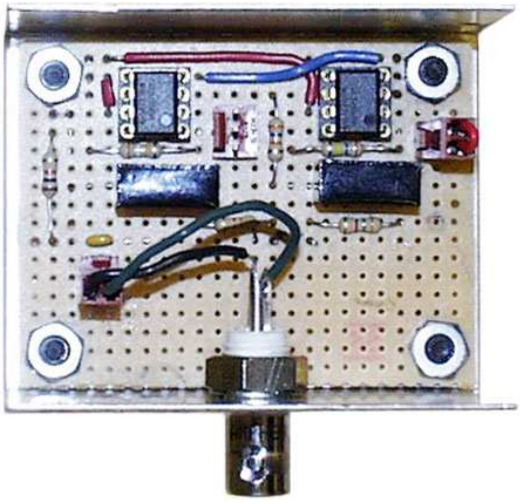

Figure B.3 *Photograph of the build preamplifier circuit.*

The noise generated by the preamplifier originates in its resistors and operational amplifiers. (The noise generated by capacitors is negligible, see Fish [7]). The thermal noise generated by the resistors was already modelled in section 3.3.2 on page 29. The noise generated by an operational amplifier is modelled in § B.4.2. In § B.4.3 a noise model for the preamplifier is derived in terms of the physical component values. Finally, in § B.4.4 the actual physical values found in § B.3 are filled in and the use of two different low noise opamps is compared.

B.4.2 Voltage and current noise of an operational amplifier

In this case study the use of two different operational amplifiers is analyzed; the op07 and the op27, both low-noise operational amplifiers. The noise produced by an operational amplifier can be modelled as a equivalent voltage noise source e_n in series with its inverting input, an equivalent current noise source i_{n-} in parallel with the inverting input and a current noise source i_{n+} in parallel with the non inverting input. These noise sources can be seen in Figure B.4.
The PSD's of the voltage noise source and current noise sources are given by (see e.g., Riedesel [17, p1749])

$$S_{e_n}(\omega) = e_o^2 \left(1 + \frac{2\pi f_v}{\omega}\right) \quad [V_{rms}^2/Hz] \tag{B.20}$$

$$S_{i_n \pm}(\omega) = i_o^2 \left(1 + \frac{2\pi f_c}{\omega}\right) \quad [A_{rms}^2/Hz] \tag{B.21}$$

where e_o^2 and i_o^2 are the asymptotic high frequency voltage and current noise PSD levels, respectively, and f_v and f_c are the voltage and current noise corner frequencies, respectively. The noise PSD S_{i_n} of the two current sources are assumed to be equal, $S_{i_n} = S_{i_n-} = S_{i_n+}$.

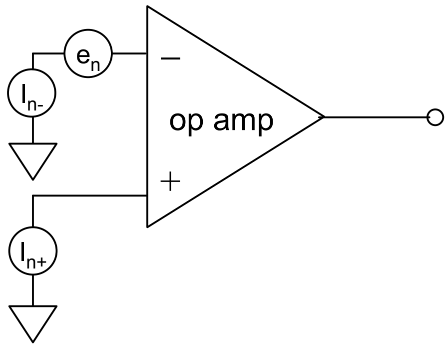

Figure B.4 *The equivalent noise sources of an opamp used to model the voltage noise, e_n, and current noise, i_{n-} and i_{n+}.*

The ASDs of these two noise sources of an op07 can be seen in Figure B.5, where the values of e_o, i_o, f_v and f_c are obtained from manufacturers product specification (Texas Instruments). The characteristic noise parameters of the two opamps are listed in Tables B.3 and B.4.

Asymptotic high frequency voltage level e_o	:	$10.0 \cdot 10^{-9}\ V_{rms}$
Asymptotic high frequency current level i_o	:	$0.14 \cdot 10^{-12}\ A_{rms}$
Voltage noise corner frequency f_v	:	$1.3\ Hz$
Current noise corner frequency f_c	:	$50\ Hz$

Table B.3 *Noise parameters of the op07*

Asymptotic high frequency voltage level e_o	:	$3 \cdot 10^{-9}\ V_{rms}$
Asymptotic high frequency current level i_o	:	$0.4 \cdot 10^{-12}\ A_{rms}$
Voltage noise corner frequency f_v	:	$2.7\ Hz$
Current noise corner frequency f_c	:	$140\ Hz$

Table B.4 *Noise parameters of the op27*

B.4.3 Noise modelling of the preamplifier

The noise model of the preamplifier developed here, is based on the models developed in Rodgers [18], [19], Riedesel (*et al.*) [17] and Horowitz and Hill [10], and corresponds to the configuration shown in Figure B.2 on page 103.

Noise model for the first preamplifier stage

In Figure B.6 the first stage can be seen again with all its noise sources included. (The geophone-coil noise is left out, because it is already accounted for in the geophone-coil noise

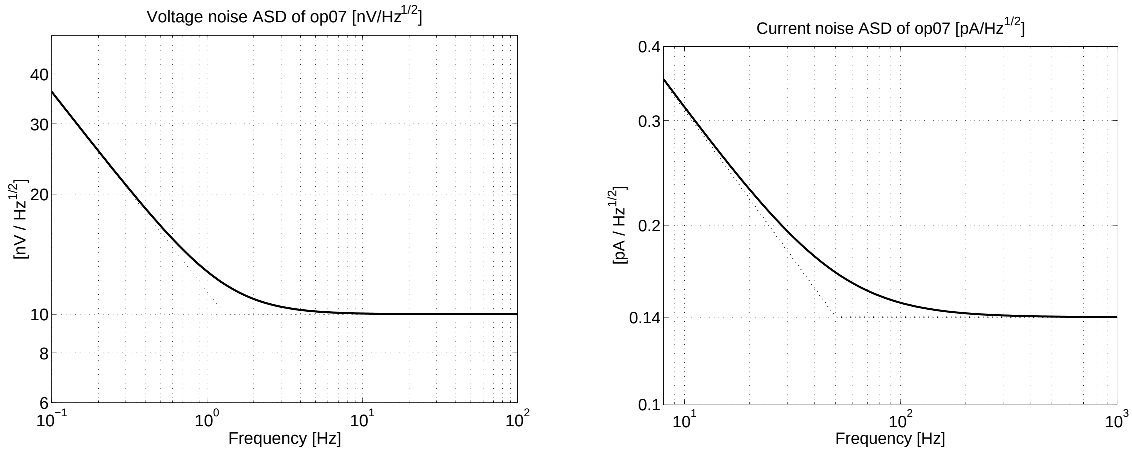

Figure B.5 left: *Voltage noise model (ASD) for the op07 with corner frequency at 1.3 Hz and an asymptotic high frequency white noise level of* $10\ nV_{rms}$. right: *Current noise model (ASD) of the op07, with corner frequency @ 50 Hz and an asymptotic high frequency white noise level of* $0.14\ pA_{rms}$.

model.)

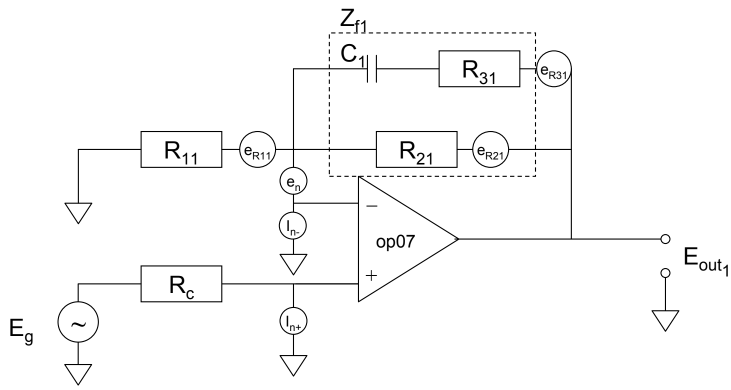

Figure B.6 *First stage of the preamplifier and all its noise sources*

The current noises, i_{n-} and i_{n+}, are shown as Norton generators from the inverting and non inverting inputs to ground. The voltage noise e_n is shown as a Thevenin generator in series with the summing junction at the intersection of R_{11} and Z_{f1}. The thermal noise voltages $e_{R_{11}}$, $e_{R_{21}}$, and $e_{R_{31}}$ are shown in series with the resistors (Rodgers [18, p1091]).

Voltage Noise, first stage

The noise PSD at the output of the first stage of the preamp due to the voltage noise of the opamp e_n is denoted by S_{o1,e_n}. From the voltage divider relationship between e_n and E_{out_1}, S_{o1,e_n} can be obtained as (see Rodgers [18, p1092]):

$$S_{o1,e_n}(\omega) = \left|1 + \frac{Z_{f1}(j\omega)}{R_{11}}\right|^2 S_{e_n}(\omega) \tag{B.22}$$

Current Noise, first stage

The noise PSD at the stage output due to the current noise of the opamp i_{n-} is denoted by $S_{o1,i_{n-}}$. Because the left side of R_{11} is at ground and the right side is at virtual ground, there is no potential difference across R_{11} due to i_{n-}. Therefore, all of i_{n-} flows through Z_{f1}, and none of it flows through R_{11}. Therefore (see Rodgers [18, 92,p1092]):

$$S_{o1,i_{n-}}(\omega) = |Z_{f1}(j\omega)|^2 S_{i_n}(\omega) \tag{B.23}$$

The noise at the stage output due to the current noise i_{n+} is denoted by $S_{o1,i_{n+}}$. i_{n+} flows directly through the coil resistance, R_c. (see Rodgers [18, p1094]) The part of i_{n+} which flows through the coil resistance R_c produces a force on the seismometer mass causing the mass to move and generate a back emf. Therefore the current noise does not see a resistance R_c but sees a source impedance Z_s. The relations for the source impedance are derived by Rodgers [18, p1096].

$$Z_s = \left(R_c + \frac{G_g^2}{m_g}\frac{s}{s^2 + 2\zeta\omega_o s + \omega_o^2}\right) \tag{B.24}$$

Accounting for the fact that the current noise sees the impedance Z_{f1} instead of only the resistance R_c, it can be seen that $S_{o1,i_{n+}}$ is given by

$$S_{o1,i_{n+}}(\omega) = |Z_s(j\omega)|^2 \left|1 + \frac{Z_{f1}(j\omega)}{R_{11}}\right|^2 S_{i_n}(\omega) \tag{B.25}$$

Thermal noise, first stage

The noise PSD at the output due to Johnson noise (see Fish [7]) generated by R_{11} is denoted by $S_{o1,R_{11}}$. The thermal noise generated by R_{11} is in series with any source voltage in the inverting configuration of the op amp, if one were connected at the left side of R_{11}. Because the gain of the inverting amplifier is given by $-Z_{f1}/R_{11}$, $S_{o1,R_{11}}$ can be written as (Rodgers [18, p1093]):

$$S_{o1,R_{11}}(\omega) = 4kTR_{11}\left|\frac{Z_{f1}(j\omega)}{R_{11}}\right|^2 \tag{B.26}$$

The noise PSD at the output due to Johnson noise generated by R_{21} and R_{31} are denoted by $S_{o1,R_{21}}$ and $S_{o1,R_{31}}$. Since the left hand side of Z_{f1} is at virtual ground, R_{21} and R_{31} both generate a noise component directly at the output, therefore

$$S_{o1,R_{21}} = 4kTR_{21} \tag{B.27}$$

$$S_{o1,R_{31}} = 4kTR_{31} \tag{B.28}$$

Finally, summing up all the noise PSD's at the output we obtain the total noise PSD at the output of the first stage of the preamplifier, denoted by $S_{pa,1}$:

$$S_{pa,1} = S_{o1,e_n} + S_{o1,i_{n-}} + S_{o1,i_{n+}} + S_{o1,R_{11}} + S_{o1,R_{21}} + S_{o1,R_{31}} \tag{B.29}$$

where the dependency on ω has been left out for convenience. Written out:

$$\begin{aligned} S_{pa,1}(\omega) \quad = \quad & \underbrace{\left|1 + \frac{Z_{f1}}{R_{11}}\right|^2 S_{e_n}}_{\text{Voltage noise}} + \underbrace{\left\{ |Z_{f1}|^2 + |Z_s|^2 \left|1 + \frac{Z_{f1}}{R_{11}}\right|^2 \right\} S_{i_n}}_{\text{Current noise}} + \\ & + \underbrace{4kT \left\{ R_{11} \left|\frac{Z_{f1}}{R_{11}}\right|^2 + (R_{21} + R_{31}) \right\}}_{\text{Johnson noise}} \end{aligned} \tag{B.30}$$

where the dependency on ω and $j\omega$ has been left out for convenience.

Noise model for the second preamplifier stage

The noise sources of the second stage are identical to the noise sources of the first stage, except for the current noise at the non inverting input of the opamp.

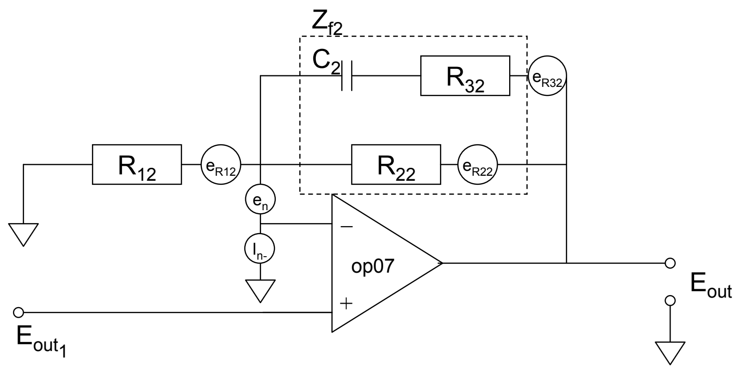

Figure B.7 *Second stage of the preamplifier and all its noise sources*

The total noise PSD at the output of stage 2 due to noise sources of stage 2 solely is denoted by $S_{pa,2}(s)$:

$$\begin{aligned} S_{pa,2}(\omega) \quad = \quad & \underbrace{\left|1 + \frac{Z_{f2}}{R_{12}}\right|^2 S_{e_n}}_{\text{Voltage noise}} + \underbrace{\left\{|Z_{f2}|^2\right\} S_{i_n}}_{\text{Current noise}} + \\ & + \underbrace{4kT \left\{ R_{12} \left|\frac{Z_{f2}}{R_{12}}\right|^2 + (R_{22} + R_{32}) \right\}}_{\text{Johnson noise}} \end{aligned} \tag{B.31}$$

where the dependency on ω and $j\omega$ has been left out for convenience.
Finally, the noise PSD at the preamp output can be written as

$$S_{pa}(\omega) = S_{pa,1}(\omega)\,|Z_{pa2}(j\omega)|^2 + S_{pa,2}(\omega) \qquad [V_{rms}^2/Hz] \tag{B.32}$$

B.4.4 A noise model for the 1000-10 preamplifier

Having obtained a general expression for the noise PSD of the preamplifier, it is now possible to plug in all the numeric values and investigate the resulting PSD's. The noise level of the preamplifier is defined by the found resistor and capacitor values at the end of Appendix B.3. The voltage and current noise levels are defined by the used operational amplifier. In this case study two opamps are considered, the op07 and the op27. Both cases are studied below. Numeric values of the op07 noise levels can be found in Tables B.3 and B.4.

using the op07

In Figure B.8 plots can be seen of the output ASD's corresponding to $S_{pa,1}(\omega)$ and $S_{pa,2}(\omega)$, when using the op07 in the circuit. In both plots, the different components comprising the ASD's can be seen, such as the total thermal noise, voltage noise and current noise. Looking at the current noise plot of the first stage, the effect of the geophone impedance can be seen as the little bump in the 5 Hz region.

On the left hand side of Figure B.10 the two ASD's can be seen again, together with the total output ASD of the preamplifier corresponding to $S_{pa}(\omega)$.

using the op27

The analysis is also made with another operational amplifier, the op27. This opamp has different noise parameters than the op07, listed in Table B.4. The transfer function of the preamplifier itself is exactly the same as the one build with the op07. Using the new values, the resulting ASD's are calculated as can be seen in
Figure B.9. On the right hand side of Figure B.10 the two ASD's can be seen again, together with the total ASD corresponding to $S_{pa}(\omega)$ using the op27.

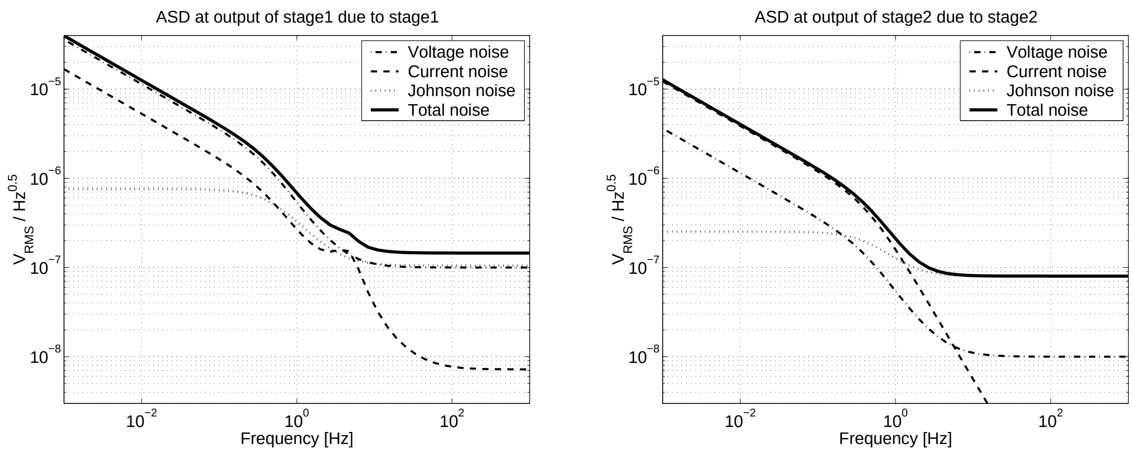

Figure B.8 left*: Resulting ASD corresponding to* $S_{pa,1}(\omega)$ *of the first stage output of the preamplifier using an op07 operational amplifier.* right*: Resulting ASD corresponding to* $S_{pa,1}(\omega)$ *of the second stage of the preamplifier using an op07 operational amplifier.*

B.4.5 Op07 and op27 performance comparison

To compare the performance of the two different opamps, one can compare the total output noise PSD's when using the different opamps. Both can be seen in Figure B.10. The total PSD using the op27 has a higher value than the op07 PSD at the lower frequencies, but is a little lower at the higher frequencies. To compare the performance one should analyze the noise propagation in closed loop, which is done in Section 3.5.4. The critical region for the preamplifier noise in the closed loop setting turns out to be the low frequency region. Since the noise of the op07 has a lower value in this region, it is chosen to use the op07.

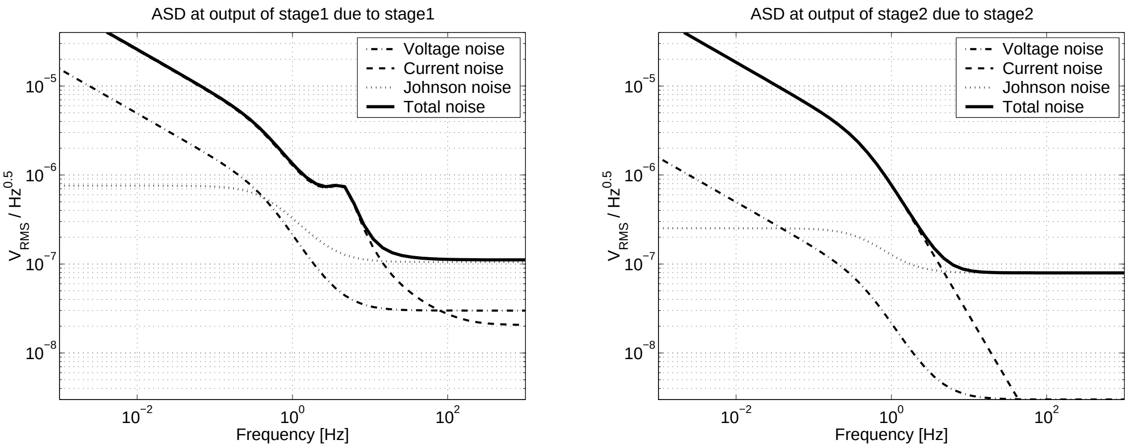

Figure B.9 left*: Resulting ASD corresponding to* $S_{pa,1}(\omega)$ *of the first stage of the preamplifier using an op27 operational amplifier.* right*: Resulting ASD corresponding to* $S_{pa,2}(\omega)$ *of the second stage of the preamplifier using an op27 operational amplifier.*

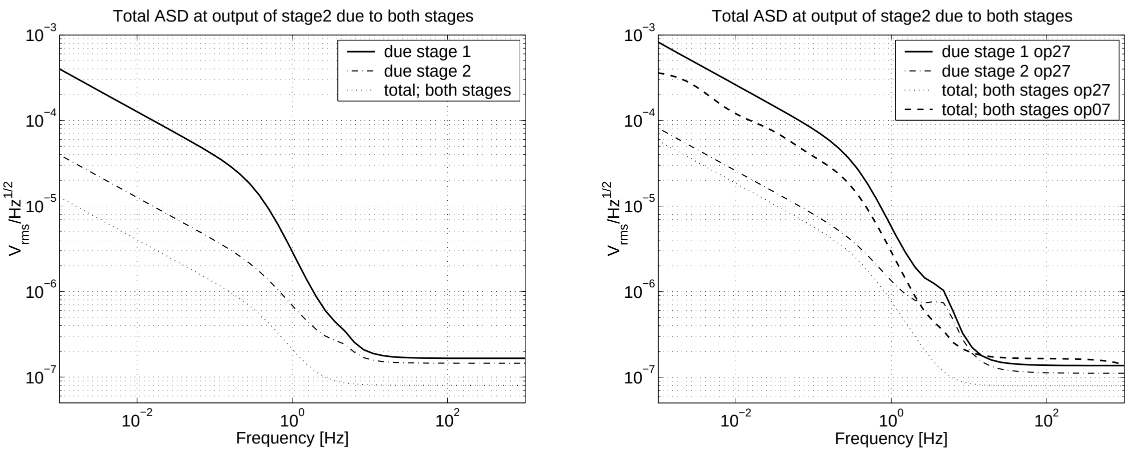

Figure B.10 left*: Total noise ASD corresponding to* $S_{pa}(\omega)$ *at output of the preamplifier using an op07. The separate contributions from the two stages to the output ASD can also be seen.* right*: Total noise ASD at preamplifier output using an op27. Again, the separate contributions of the two stages to the output ASD can also be seen. For performance comparison, the total output ASD using an op07 is plotted again. The total ASD using the op27 has a higher value than the op07 ASD at the lower frequencies, but is a little lower at the higher frequencies.*

Appendix C

Experimental setup MIT

In this appendix the experimental vibration isolation setup used at MIT is described. First a list of used hardware and software is given, then it is described how the hardware is connected.

C.1 List of used equipment

- Hewlett Packard 35665A Dynamic Signal Analyzer
- Crown DC300R stereo power amplifier
- Cerwin-Vega VEGA 84 subwoofer/speaker
- dSpace 1104 controller board, PCI-card in PC.
- Geo Space vertical geophone, GS-11D @ 4.5 Hz @ 4000Ω, http://www.geospacelp.com.
- Texas Instruments, operational amplifier op07c (in preamplifier circuit).

C.2 List of used software

- MATLAB® R12 and Simulink.
- ControlDesk 2.2: to control the dSpace board from a PC.
- sdftoml.exe: conversion program for HP analyzer `*.dat` files.

C.3 Hardware connection

In Figure C.1 a schematic of the hardware configuration of the vibration isolation setup can be seen using the preamplifier. The setup is shown in closed loop configuration while measuring the geophone output signal for analysis with the HP analyzer. The speaker-geophone combination corresponds to the schematic shown in Figure 3.2 on page 21. In Figure C.2 a photograph of the preamplifier-speaker-geophone setup can be seen. Most of the hardware is electrically connected using bnc-cable's (see figure), which has a inner-wire carrying the signal and an outer shielding which is connected to earth ground located in the dSpace board. The outer shielding of the bnc-cable's protects the delicate signals from electrical pick up noise. The power amplifier generates relatively large signals and can therefore be connected to the speaker voice coil using two simple electrical wires.

In Figure C.3 the hardware configuration of the swept sine experiment, which was done to identify the empirical poweramp-speaker-geophone model E_g/E_{in}, can be seen. The output of the analyzer, generating the sinusoidal source signals is connected with bnc-cable's to the power amplifier input and to the second analyzer input. The geophone output is fed into the first input channel of the analyzer. In the same manner the transfer function of the preamplifier was validated; the output of the analyzer was connected to the preamplifier input and its output was connected to the second input of the analyzer.

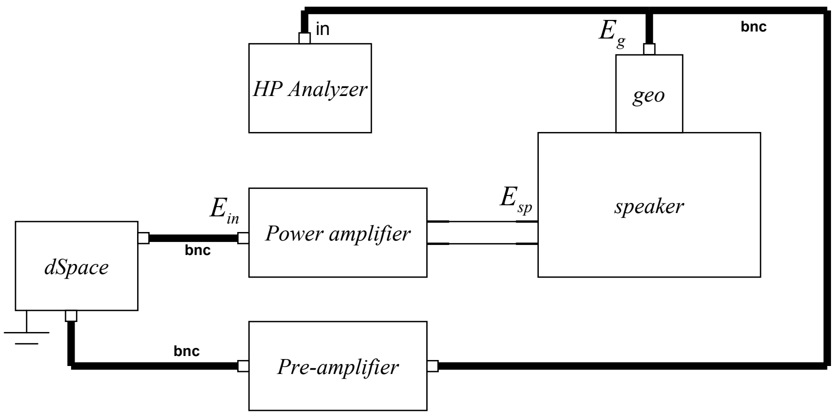

Figure C.1 *Closed loop hardware configuration MIT vibration isolation setup measuring the geophone output signal with the HP analyzer.*

C.4 Practical notes on using the HP35665A DSA

When one wants to measure a PSD with the analyzer a few things have to be taken into account. The analyzer shows the results on an the board display in the units set by the user. When the results are written to a $*$`.dat` file on a floppy disk, the data will be saved as an peak power spectrum with units [SI^2]. To convert the data to PSD units [SI$^2_{rms/Hz}$] the software `sdftoml.exe` can be used (comes on a floppy disk with the analyzer). With the following line the data is converted to the right units:

```
sdftoml sourcefile.dat /X /Y:PRD
```

The data is now written to a $*$`.mat` file which can be loaded in MATLAB®. For more conversion options see the software manual. `sdftoml.exe` can also be found on the CD ROM that comes with this thesis.

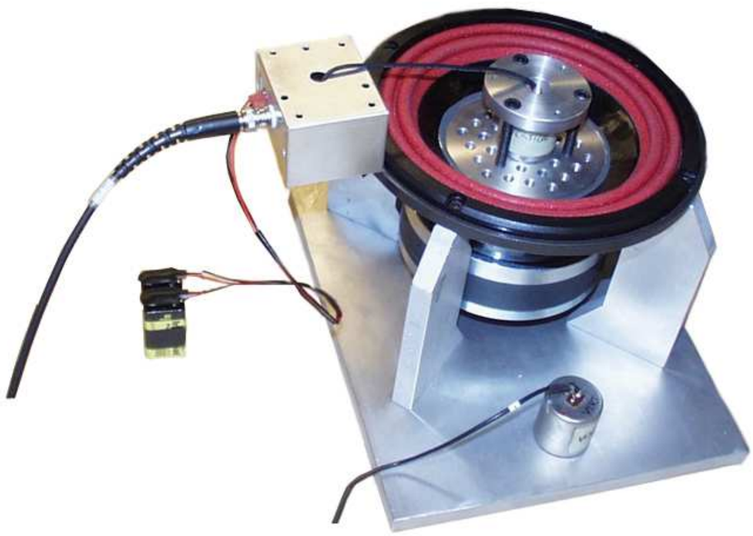

Figure C.2 *Hardware of the MIT vibration isolation setup. The speaker-geophone setup together with the preamplifier located at the rim of the speaker. The preamplifier is contained in an aluminum box, to shield it from electromagnetic disturbances. Two 9 Volt batteries can be seen that are used to power the preamplifier. On the base plate of the setup a similar geophone as is mounted on the cone plate of the speaker can be seen (this geophone is not used in the setup, but is used to measure the ground vibration level).*

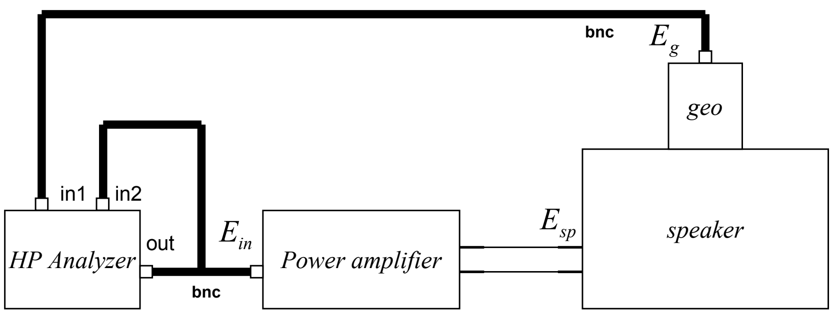

Figure C.3 *Hardware configuration MIT vibration isolation setup for swept sine identification experiment.*

Appendix D

CD-ROM

The files on the CD-ROM are divided over three folders: `Matlab`, `LaTeX` and `Files`.

D.1 MATLAB® m-files

The `/Matlab` folder contains two subfolders `AVIMIT` and `AVIPhilips`, in which all the MATLAB® files used in the case study at MIT and Philips can be found respectively. Both case studies have the same m-file structure. The main m-file is a `go.m` file. From this m-file all the other files are imported. The sequence of m-files and what happens in the m-files is quite self-explanatory by the comments. The `go.m` file is designed to run from top to bottom. The structure of the `go.m` files is briefly described below, the commented lines explain what happens in the imported m-file:

```
% pick up parameters, all parameters are defined here!
parameters

% define all system models
system_models

% define controller(s)
controllers

% define all noise models
noise_models

% define systems and filters in generalized plant format
genplant_systems

% define generalized plant with filters
genplant
```

```
% H2 controller synthesis
controller_H2

% close the loop and define all propagation transfer functions
closeloop

% simulate performance by propagating noise sources to output
calc_noise_prop

% plot propagations results
plot_prop_res
```

In the MIT case study a few different system configurations can be chosen. In the file `MIT_readme` is explained what to change in the m-files in order to simulate a different case. Only in the MIT case study an $\mathcal{H}_2$ controller can be synthesized.

D.1.1 tools

In the folder `Matlab/tools` a few tools can be found that are needed to run the `go.m` files and are self written. This folder must be added to the MATLAB® search path.

- `cumpsd.m`, calculates the PSD, PS, CPS and variance of the output of a system with a PSD at the input.
- `spectra.m`, calculates the PSD, PS and CPS of a sampled time signal.
- `check_genP.m`, algorithm to check if the standard assumptions on the weighted generalized plant are met for $\mathcal{H}_2$ controller synthesis.
- `frqrsp.m`, calculates frequency response of system.
- `angl.m`, calculates phase response of system.
- `makesys.m`, converts a state space system into system-matrix format in which the generalized plant is defined, a format used in the μ-toolbox.
- `makess.m`, converts a system in system-matrix format to state space format.
- `parr.m`, calculates the parallel combination of two values, e.g., resistors.

More information on how to use the m-files can be found in their help text.

D.2 LATEXfiles

In this folder all the LATEXfiles used to write this thesis can be found. The main file of this thesis is a WinEdt project file: `MasterThesis.prj`. The structure of the LATEXfiles follows from the comments in the main file `report.txt`, which can be found when opening the project file. In the folder `image_files` most of the source files used to generate the images in the thesis can be found, e.g., in the `/PPT` folder all the PowerPoint files are located. A commented line above each figure environment in the LATEXcode points out were the image was created.

D.3 Files

The folder Files/doc contains all digital literature used in this thesis, a large number of `*.pdf` files. The folder Files/Pics contains pictures of the setup build at MIT.

Bibliography

[1] Balmer L. Signals and Systems. sec. ed. Prentice Hall, Europe, 1998.

[2] Barzilai A., VanZandt T., Kenny T. Technique for measurements of the noise of a sensor in the presence of large background signals, Review of Scientific Instruments, Vol. 69, No. 7, pp 2767-72, july 1998.

[3] Boyd S., Barrat C. Linear Controller Design - Limits of Performance. Prentice Hall, 1991.

[4] Scherer C. Theory of Robust Control. Lecture notes, Delft University of Technology, Netherlands, 2001.

[5] Keith G., Doyle J.C. State-space formulae for all stabilizing controllers that satisfy an $\mathcal{H}_\infty$ norm bound and relations to risk sensitivity. System and Control Letters, Vol 11, pp 167-172, 1988.

[6] Doyle J.C., Glover K., Khargonekar P.P., Francis B.A. State-space solutions to standard $\mathcal{H}_2$ and $\mathcal{H}_\infty$ control problems. IEEE Transactions on Automated Control, Vol. 34, No 8, august 1989.

[7] Fish P.J. Electric Noise and Low Noise Design. McGraw Hill Inc. New York, 1994.

[8] Goossens H.M.W. By speach, Philips CFT, Eindhoven 2003.

[9] Harris C.M. Harris' Shock and Vibration Handbook. McGRaw-Hill Professional, 5^{th} ed., 2001.

[10] Horowitz P., Hill W. The Art of Electronics. Cambridge University Press, Cambridge, 1990.

[11] Ljung L. System Identification - Theory for the User. Prentice Hall, New Jersey, 1987.

[12] Monkhorst W. Feasibility Study of the Dynamic Error Budgeting Design Approach. Mech. Eng. Systems and Control Group, Delft Univ. of Technology, The Netherlands, 2002.

[13] Oppenheim A.V., Schafer R.W., Buck J.R. Discrete-Time Signal Processing. Prentice Hall, 2nd ed., 1999.

[14] Papoulis A. Probability, Random Variables and Stochastic Processes. McGraw-Hill, 1965.

[15] Peterson J. Observations and modeling of seismic background noise, United States Department of the Geological Survey, Open-File Report 93-322, Albuquerque, New Mexico, 1993, http://aslwww.cr.usgs.gov/Publications, last accesed 01-2004.

[16] Priestley M.B. Spectral analysis and time series. Academic Press, London, 1989.

[17] Riedesel M.A., Moore R.D., Orcutt J.A. Limits of Sensitivity of Inertial Seismometers with Velocity Transducers and Electronic Amplifiers. Bulletin of the Seismological Society of America. Vol. 80, No. 6, pp. 1725-1752, December 1990.

[18] Rodgers P.W. Frequency Limits For Seismometers as Determined from Signal-to-Noise Ratios. Part 1. The Electromagnetic Seismometer. Bulletin of the Seismological Society of America, Vol. 82, No. 2, pp. 1071-1098, April 1992.

[19] Rodgers P.W. Maximizing the Signal to Noise Ratio of the Electromagnetic Seismometer: the Optimum Coil Resistance, Amplifier Characteristics, and Circuit. Bulletin of the Seismological Society of America, Vol. 83, No. 2, pp. 561-582, April 1993.

[20] Roover D. de. Motion Control of a Wafer Stepper - A Design Approach for Speeding Up IC Production. PhD Thesis, Mech. Eng. Systems and Control Group, Delft Univ. of Technology, The Netherlands, 1997.

[21] Slocum, A.H., Precision Machine Design. Prentice-Hall, Inc., New Jersey, 1992.

[22] Subrahmanyan, P.K. A Model Approach to Precision Motion Control. PhD Thesis, Medch. Eng., Massachusetts Institute of Technology, Boston, USA, 1999.

[23] Texas Instruments Application Report. Noise Analysis in Operational Amplifier Circuits. SLVA043A, 1999. Internet document, last accessed Mch-2003.

[24] Trumper D.L., Sato T. A Vibration Isolation Platform. Mechatronics, No. 12, pp. 281-294, Elsevier Science Ltd. 2002.

[25] Usher M.J. Developments in Seismometry. Journal of Physics E: Scientific Instruments, Mechatronics, No. 6, pp. 501-507, Great Britain 1973.

[26] Vervoordeldonk M. By speach, Philips CFT, Eindhoven, 2003.

[27] Zhou K., Doyle J.C., Glover K. Robust and Optimal Control. Prentice Hall, Upper Saddle River, NJ, 1996.